# Voyager 1 Observations of Galactic Cosmic Ray Anisotropies in the Local Interstellar Medium

Thesis by

Jamie Sue Rankin

In Partial Fulfillment of the Requirements
for the Degree of
Doctor of Philosophy


CALIFORNIA INSTITUTE OF TECHNOLOGY
Pasadena, California

2019
(Defended August 23, 2018)

Jamie Sue Rankin
ORCID: 0000-0002-8111-1444

*The heavens declare*
*the glory of God.*

*The firmament shows*
*his handiwork.*

*Day to day*
*pours forth speech.*

*Night to night*
*imparts knowledge.*

*Thereof is no speech,*
*thereof no words,*
*thereof no sound not heard.*

*Throughout the earth*
*their verse goes out,*
*their language to world's end.*

*For the sun he made a tent in them;*
*he is like a bridegroom*
*who exits his canopy.*

*He rejoices like a champion*
*the course to run.*

*His point of exit: at heaven's end,*
*his circuit, against its extremities;*
*nothing is hidden from his heat.*

— Psalm 19:1-6

# Acknowledgements

On Friday, August 31, 2012 – just six days after Voyager 1 arrived in interstellar space – I arrived in Pasadena, California, to begin graduate school at Caltech. My new advisor, Edward C. Stone, invited me to attend the Voyager Science Steering Group meeting which started the following Monday.

I will never forget my first day on the job. As I entered the meeting room of the Voyager SSG, I walked into a room full of world-class scientists engaged in lively discussion about humankind's first in-situ measurements of interstellar space. Indeed, it was a historical moment, and there I was, a kid in her early 20's wearing sandals, shorts, and a comical t-shirt with a black-hole Pac-Man eating a bunch of planets. I scanned the room noting that I was a few decades younger than the mean of the age distribution and thought, "Wow, what will they think of me? I'd better quietly sneak into the back corner so no one notices."

But, I did not go unnoticed. Dr. Stone saw me and smiled as I came in. He warmly welcomed me and introduced me to the whole group. Suzanne Dodd even joked that they should include my picture on the front cover of the SSG report. The Voyager team was incredibly kind and welcoming, and I very quickly found myself at home in my new home.

The journey since has been one of incredible discovery. I personally believe that the timing has been too much to attribute to mere random chance and praise God for orchestrating the many humbling, amazing opportunities in which I have participated. Although the Voyagers were launched a decade before I was born, the Voyager data that I worked on for this thesis – humankind's

first in-situ measurements of interstellar space – was all acquired during my time here! Moreover, not only was I able to gain invaluable instrumentation and hardware experience working on the initial detector testing and instrument development of EPI-Hi, but I also recently attended Parker Solar Probe's launch. Every day as a graduate student here has been like living in a legacy of discovery.

I find it bittersweet now, six years later, to be finishing up this wondrous season at Caltech. I am very grateful and humbled by the privilege of working with some amazing people along the way. First of all, thank you Dr. Edward C. Stone for your patience, encouragement, faithful mentoring and teaching, and for never giving up on me, even when I stumbled upon many obstacles along the way. I know firsthand why so many people both respect you as a scientist and describe you as one of the kindest people they have ever met. It has been a privilege to work with a living legend such as yourself – thank you for making time for me and taking me under your wing.

Alan Cummings, thank you for your careful attention to detail, whether it be record-keeping at accelerator runs, accumulating bird-watching statistics, or keeping track of what's what on Voyager CRS. You've inspired me to be thorough, well organized, and to carefully document important details. Thank you for your hard work on the initial stages of investigating CRS's observations of Voyager's pitch angle anisotropies, and thank you for passing this project on to me. This thesis would not have been possible without your guidance and willingness to share with me the information you've discovered from your own work. Also, thank you for catching me up to speed on the many things which have happened in the last 40 years. To Ed and Alan both – I look forward to continued collaboration with you on Voyager in the future.

Thank you, other members of the Voyager team – including Len Burlaga,

Rob Decker, Don Gurnett, Bryant Heikkila, Tom Krimigis, Nand Lal, John Richardson, and Ed Roelof for answering my questions, giving me much useful input, and for making data available to me. I look forward to participating in future Voyager SSG's.

Rick Leske, thank you for your being an excellent friend and a good sounding board for ideas. I will miss our fun conversations in your office and I greatly appreciated your input as I was figuring out how to approach different aspects of the Voyager data analysis. I will miss your punny sense of humor and stabilizing realism as I move on to my postdoc, but I look forward to playing Blokus with you at the AGU.

Mark Wiedenbeck, thank you for patiently training and teaching me about instrumentation and for letting me take on many responsibilities that are rare for graduate students these days. It was a privilege to work with you on the EPI-Hi detector testing and development; I look forward to continued work with you and others as we analyze this incredible new data measured near the sun in the coming years of the Parker Solar Probe Mission!

Thank you, members of the Caltech Space Radiation Laboratory – including Caprece Anderson, Jill Burnham, Christina Cohen, Rick Cook, Marty Crabil, Andrew Davis, Michele Judd, Branislav Kecman, Allan Laborador, Dick Mewaldt, Debby Miles, and Heather Steele, for welcoming into the SRL family. Thank you, Nigel Angold, Barry Birdwell, and Danny Everett, for your hospitality and for "showing me the ropes" during the course of my travels. I will miss you all greatly, but I hope to see you a lot in the future.

Thank you, members of Graduate Christian Fellowship and other friends at Caltech for praying for me, encouraging me, and sharing in both the joys and trials in our voyages as graduate students. Thank you, Andrew Longman and Liz Holman for being my SoCal adventure buddies! Thank you also,

people of Prism church, for your spiritual guidance, moral support and your "GoPrayForMe" campaign that turned the tides of many obstacles that I've encountered. You are mighty prayer warriors! Thank you, Arnie and Bonnie Welch for providing a home away from home for me in Pasadena. Thank you Mike Roster, Leigh Torgerson, Nigel Angold, John and Debby Isenberg, Chuck and Carolyn Ryor, George and Christie Binder, Nick Holly, Steve and Jane Gropp, Bill and Delores Bing, Glenn Price, and others for being a part of my California family.

Thank you to my University of Utah professors and mentors for teaching me, fueling my passion for learning, believing in me, and encouraging me to "dare mighty things" – Pat Shea, Pierre Sokolsky, Gordon Thomson, Stephen Goldsmith, Janice Ugaki, Scott Hagen, Orest Symko, Valy Vardeny, and others. Onward!

Finally, thank you to my Utah family for cheering me on and supporting me in this daring endeavor of pursuing a PhD – Robert Rankin, SueZanne Rankin, Danielle Rankin, Kristy Thayne, Sam Thayne, Ian Thayne, Marilyn Rankin, Barbara and Dan Dickerson, and others in my extended family. I know you have missed me dearly (I have missed you too!), but thank you for your many sacrifices that have enabled me to go and spread my wings. I love you all very much!

This work was supported by NASA Grant NNN12AA01C.

# Abstract

Since crossing the heliopause on August 25, 2012, Voyager 1 has observed reductions in galactic cosmic ray counting rates caused by a time-varying depletion of particles with pitch angles near 90°, while intensities of particles with other pitch angles remain unchanged. Between late 2012 and mid-2017, three large-scale, durable events occurred, lasting roughly 100 to 630 days. Omnidirectional and directional data from the Cosmic Ray Subsystem's high energy telescopes are used to report observations of the cosmic ray intensity variations. Omnidirectional ($\gtrsim$ 20 MeV) proton-dominated measurements show up to a ∼3.8% intensity reduction. Bi-directional ($\gtrsim$ 70 MeV) and unidirectional (∼18 to ∼70 MeV) proton-dominated measurements are analyzed using data taken from various spacecraft orientations, including during magnetometer roll calibrations and 70°-offset maneuvers. The anisotropy is characterized as a "notch" in an otherwise uniform pitch-angle distribution of varying depth and width centered about 90° in pitch angle space. The notch averages ∼22° wide and ∼15% deep – signifying a depletion region that is broad and shallow. However, electron observations reveal that there is only a weak, at most, evidence of pitch angle anisotropy in cosmic-ray electrons with energies of ∼3 to ∼105 MeV, indicating that the generation of the notch or its evolution differs between electrons and protons, or varies with rigidity. There are indications that the anisotropy is formed by a combination of magnetic trapping and adiabatic cooling in associated shocks or compression regions.

# Published Content and Contributions

[1] J. S. Rankin, E. C. Stone, A. C. Cummings, N. Lal, and B. Heikkela,"Galactic Cosmic-Ray Anisotropies in the Local Interstellar Medium from Voyager 1 Observations" (manuscript in preparation).

*Contributions: I am the primary author, wrote all of the text, performed all of the data analysis and created most of the figures.*

# Contents

# Glossary of Acronyms and Terms

| **Term** | **Definition** |
|---|---|
| AS | A-Stopping; unidirectional CRS rate consisting of particles stopping in the A-end of HET 1 or 2 |
| BS | B-Stopping; unidirectional CRS rate consisting of particles stopping in the B-end of HET 1 or 2 |
| BSe | B-Stopping electrons |
| BSp | B-Stopping protons |
| Clock Angle | The angle of the boresight in the N-T plane with the $\hat{N}$-axis as the origin and the angle increasing towards $\hat{T}$ |
| CRS | Cosmic Ray Subsystem |
| GCRs | Galactic Cosmic Rays |
| Guards | HET 1, HET 2, and TET anti-coincidence counters that produce $\gtrsim$ 20 MeV, proton-dominated omnidirectional rates on CRS |
| HET | High Energy Telescope |
| ISM | Interstellar Medium |
| LECP | Low Energy Charged Particle instrument |
| LISM | Local Interstellar Medium |
| MAG | Magnetometer |
| Offset Epoch | The first day of a sequence of 70-° offset maneuvers, sin the form: Year-DOY |
| PENH | Penetrating High-Gain Mode; $\gtrsim$ 70 MeV, proton-dominated bi-directional rates on CRS |
| Pitch Angle | The angle of a particle's trajectory or telescope's boresight with respect to the magnetic field |
| PWS | Plasma Wave Subsystem |
| Roll Epoch | the set of 10 turns which took place on a particular day in the form: Year-DOY |
| R, T, N | Spacecraft-centered coordinate system where $\hat{R}$ is the sun-to-spacecraft vector, $\hat{T}$ is the cross product of the sun's rotation vector with $\hat{R}$, and $\hat{N}$ completes the triad of the right-handed system |
| TET | The Electron Telescope |
| VLISM | Very Local Interstellar Medium |

# List of Figures

# List of Tables

# Chapter 1
# Introduction

## 1.1 The Heliosphere and its Dynamic Environment

As the million-degree upper atmosphere of the sun (the solar corona) expands outward into space, its accelerated plasma is driven forward with sufficient pressure to overcome the sun's inward gravitational pull, forming a supersonic solar wind [6–8].

The sun rotates on an axis that is tilted 7.25° with respect to earth's orbit (the ecliptic plane) and makes a complete rotation every ∼27 days (equatorial), while maintaining the solar wind's radially outward flow. Its magnetic fields are frozen into the solar wind plasma, and the sun's rotation, combined with the solar wind's outward expansion twists the interplanetary magnetic field into the shape of an Archimedean spiral (Parker spiral) in the solar equatorial plane [6, 7, 9].

The sun's activity is marked by an ∼11-year solar cycle, traditionally characterized by the numbers of sunspots; its magnetic field undergoes polarity reversal every ∼11 years. Polar coronal holes form on the sun's surface during solar minimum, producing fast solar wind streams. When these fast streams encounter slower solar winds, they compress the plasma, producing co-rotating interaction regions (CIRs) that are bounded by forward and reverse shocks [10].

During solar maximum, the monthly mean sunspot number increases, as does the level of solar activity [11]. Localized magnetic energy is released in violent eruptions, expelling the large amounts of radiation and plasma in solar

flares and coronal mass ejections (CMEs)[10]. These events are also known to accelerate solar energetic particles (SEPs) from ∼few keV energies to greater than a GeV (see, e.g. [12]).

As the solar wind hydrodynamically expands, it forms a bubble that encompasses all of the planets, known as the heliosphere. Along the way, it slows from supersonic speeds (∼400 km/s) to subsonic (∼100 km/s) at the termination shock[1.1]. Beyond the termination shock is the heliosheath, a turbulent region where the subsonic solar wind is deflected as it approaches the heliosphere's boundary. This complex environment is characterized by low plasma densities (∼0.002 $cm^{-3}$) [21, 22], weak magnetic fields (∼0.1 nT) [23], and large-amplitude fluctuations in field strengths within several hours or days [24]. The heliosphere achieves a pressure balance with the surrounding local interstellar medium at its outermost boundary called the heliopause [25], [26].

Voyager 1 was launched in September 1977 and following encounters with Jupiter and Saturn, started on a trajectory ∼35° north of the ecliptic, roughly towards the heliopause nose – the direction of the solar system's velocity through the interstellar medium. Voyager 2 was launched in August 1977, and is currently on a trajectory that is ∼30° south of the ecliptic towards the flank. Figure 1.1 shows a history of galactic cosmic ray counting rates observed by Voyager 1's Cosmic Ray Subsystem from 1977 (inner heliosphere) through 2018 (interstellar space). Solar modulation is prominent before the termination shock crossing (TSX); cosmic ray intensities vary inversely with solar activity (note the ∼11-year periodicity). Beyond the termination shock, solar modulation is much weaker, but the radial gradient of increasing cosmic ray intensities with

[1.1] Voyager 1 crossed the termination shock at a radial distance of 94 AU [13–16]. Voyager 2 crossed the termination shock in 2007 at 84 AU, leading to the discovery that the termination shock is blunt and asymmetric [17–21].

increasing radial distance from the sun is still evident. After the heliopause crossing (HPX), intensities become mostly uniform and isotropic.

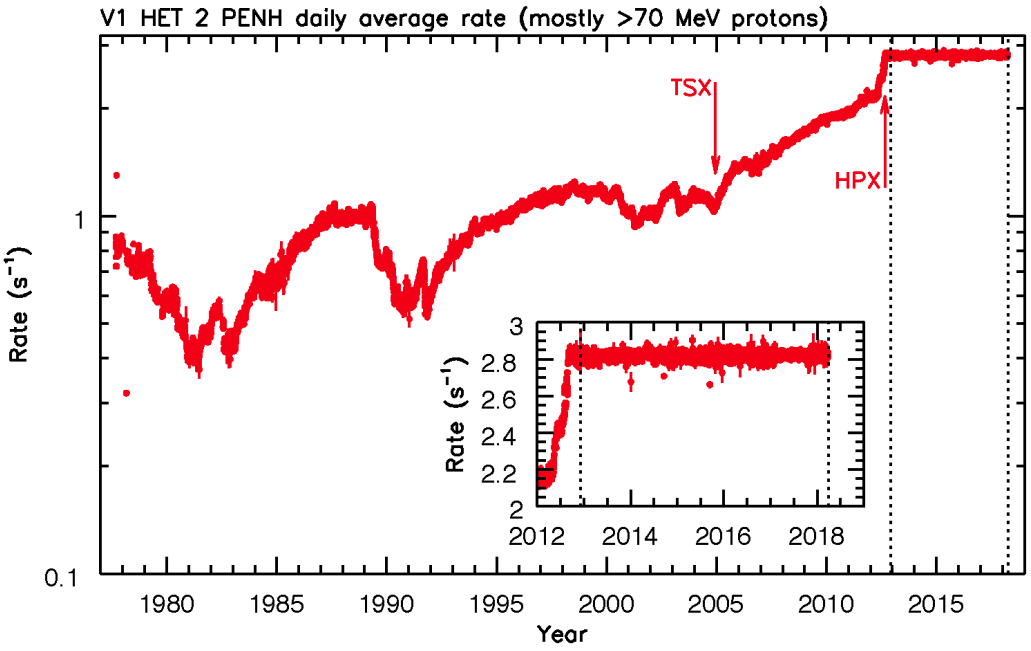


**Figure 1.1**. Rate of galactic cosmic rays from 1977 (inner heliosphere) through 2018 (interstellar space) measured by the HET 2 telescope on the Voyager 1 Cosmic Ray Subsystem. TSX denotes the termination shock crossing and HPX denotes the heliopause crossing. The inset shows that cosmic ray intensities in the very local interstellar medium are mostly uniform and isotropic. This figure is an updated version of Figure 1 of [1] provided by Alan Cummings (private communication).

Voyager 1 has exited the heliosphere and continues its journey into the very local interstellar medium, while Voyager 2 remains inside the heliosheath, approaching its own interstellar encounter.

## 1.2 Cosmic Rays in the Quiescent Local Interstellar Medium

While the solar system is filled with dynamic interactions of particles, plasmas, and fields governed by the activity of the sun, the local interstellar medium

(LISM) is a quiescent place. It is composed of a low-$\beta$ plasma with densities of $\sim$0.1 cm$^{-3}$ [27] and magnetic fields of $\sim$0.3 nT [28]. Its constituent energetic particles are galactic cosmic rays with energies of several MeV and higher.

Galactic cosmic rays (GCRs) are fully ionized atomic nuclei that are accelerated by various galactic sources, including supernova [29]. Individual particles travel along field lines in helical orbits with a gryoradius, $r_g$ and angle, $\alpha$ with respect to the local field (pitch angle). They most efficiently scatter off of magnetic irregularities (turbulence) of scales comparable to their gyroradii [30].

Because they originate from sources that are kiloparsecs away, GCRs undergo large amounts of scattering, causing their intensity distribution to be isotropic by the time they reach the LISM. Nonetheless, due to the region's very low levels of turbulence, GCR scattering mean free paths are very large, even compared to the size of the heliosphere ($\sim$25,000 AU vs. $\sim$120 AU).[1.2]

## 1.3 The Very Local Interstellar Medium: Influenced by Solar Transients

The very local interstellar medium (VLISM) lies in the wake of the interstellar wind's interactions with the heliosphere. As the 26 km/s flow of interstellar plasma is deflected by this magnetosphere-like obstacle, the interstellar wind drapes the interstellar magnetic field around the heliosphere [23] and produces gradients of plasma density just beyond the heliopause [32, 33].

Meanwhile, in the inner solar system, CMEs, CIRs and other solar wind transients from the inner solar system may coalesce to form merged interaction regions (MIR) and global merged interaction regions (GMIRs)(see, e.g. Chapter 8 of [34]). These large-scale structures are capable of passing beyond

[1.2]The reported mean free path is for a 1 GeV proton, calculated using a parallel diffusion coefficient of $10^{28}$ cm$^2$ s$^{-1}$ [30]. For comparison, the scattering mean free path of the same-energy particle near the earth is $\sim$0.5 AU [31].

the termination shock, propagating through the heliosheath, and generating compressive waves at the heliopause boundary that propagate outward and produce weak shocks in the VLISM.

Such events have been observed in the heliosheath by Voyager 2 [35], and their effects have been modeled extensively via time-dependent simulations, many of which are informed by solar wind observations[1.3] [36–40]. One of these models even successfully predicted a recently observed shock outside the heliopause [41]. Indeed, the VLISM is not only a complex region formed by the steady-state collision of interstellar plasmas with the heliosphere, but it is also influenced by solar transients, as Voyager 1 has now discovered.

After a 35-year journey through the solar system, Voyager 1 finally crossed the heliopause boundary[1.4], and reached interstellar space on August 25, 2012. The transition was marked by sharp increases in low-energy galactic cosmic rays (GCRs) and corresponding sudden decreases in anomalous cosmic rays, as observed by the Cosmic Ray Subsystem (CRS) and Low Energy Charged Particle (LECP) instruments [42–44]. In the wake of Voyager's interstellar arrival, LECP observed an unexpected anisotropy in the GCRs, characterized by a clear reduction in $>$ 211-MeV proton intensities for particles entering their bi-directional telescope when viewing perpendicular to the magnetic field. Several durable, time-dependent events have continued to occur during Voyager 1's interstellar journey.

In addition to the GCR anisotropies, several shock-related disturbances have been observed in the VLISM by Voyager 1's four working instruments. [23, 45] have reported evidence for several weak, laminar, quasi-perpendicular, subcritical, shocks observed by the Magnetometer (MAG). [4, 32] detail a series

[1.3] The OMNI database provides near-Earth spacecraft-interspersed SW data and is used by many of these models: https://omniweb.gsfc.nasa.gov.

[1.4] At a radial distance of 122 AU from the sun

of locally-generated electron plasma emissions detected by the Plasma Wave (PWS) instrument.

There is evidence that the transient shock events and GCR anisotropies may be related. For example, [3, 46] found through numerical simulations that a gradual shock, followed by a slow weakening of the magnetic field may account for the pitch angle and time profiles of both transient GCR increases and anisotropic decreases, interpreting the latter to arise from adiabatic cooling behind the shock.

The current work focuses on CRS measurements of the GCR anisotropy, presenting additional information about these unusual events through measurements of proton and electron intensities. In the following chapters, observations with multiple telescopes and varying spacecraft orientations are reported, and two models are employed to characterize the temporal and spatial behavior of the unexpected pitch angle phenomena. Results are incorporated into three types of simulated response functions, yielding predictions for comparison with observations. Shock-related magnetic trapping and adiabatic cooling are discussed as possible physical mechanisms for producing the anisotropy.

# Chapter 2
# Voyager 1's Cosmic Ray Subsystem

## 2.1 Basic Operating Principles

The Cosmic Ray Subsystems (CRS) on both the Voyager 1 and Voyager 2 spacecraft consist of 4 single-ended low-energy telescopes (LETs A, B, C, and D), 2 double-ended high-energy telescopes (HETs 1 and 2), and a single-ended electron telescope, together capable of measuring ∼1 to ∼500 MeV/nuc ions[2.1] from hydrogen through nickel ($1 \leq Z \leq 28$) and electrons from ∼3 to ∼110 MeV (see [1, 48] for more details).

Since the present work involves interstellar observations of galactic cosmic rays, the focus will be on measurements taken by Voyager 1. However, it is noted that the basic operating principles of CRS particle telescopes (pictured in Figure 2.1) have much in common with those found on recent spacecraft such as HET on STEREO [49] and EPI-Hi on Parker Solar Probe [50].

### 2.1.1 Particle Identification via the dE/dx-E Method

Consider an incident particle of charge $Z$, mass $M$, and kinetic energy $E$ that deposits most of its energy through a thin front detector of thickness $L$ – losing energy $\Delta E$ – and stops below it in a second detector, losing its remaining energy, $E' = E - \Delta E$. The rate of energy loss is proportional to $Z^2$ and can therefore be used to identify the particle's species (for the non-relativistic case, $\Delta E \propto LZ^2/v^2$). Knowing both $\Delta E$ and $E'$, one can solve for $Z$ via

[2.1] This range applies for stopping particles. The range for penetrating particles extends to roughly a few GeV (see [47]).

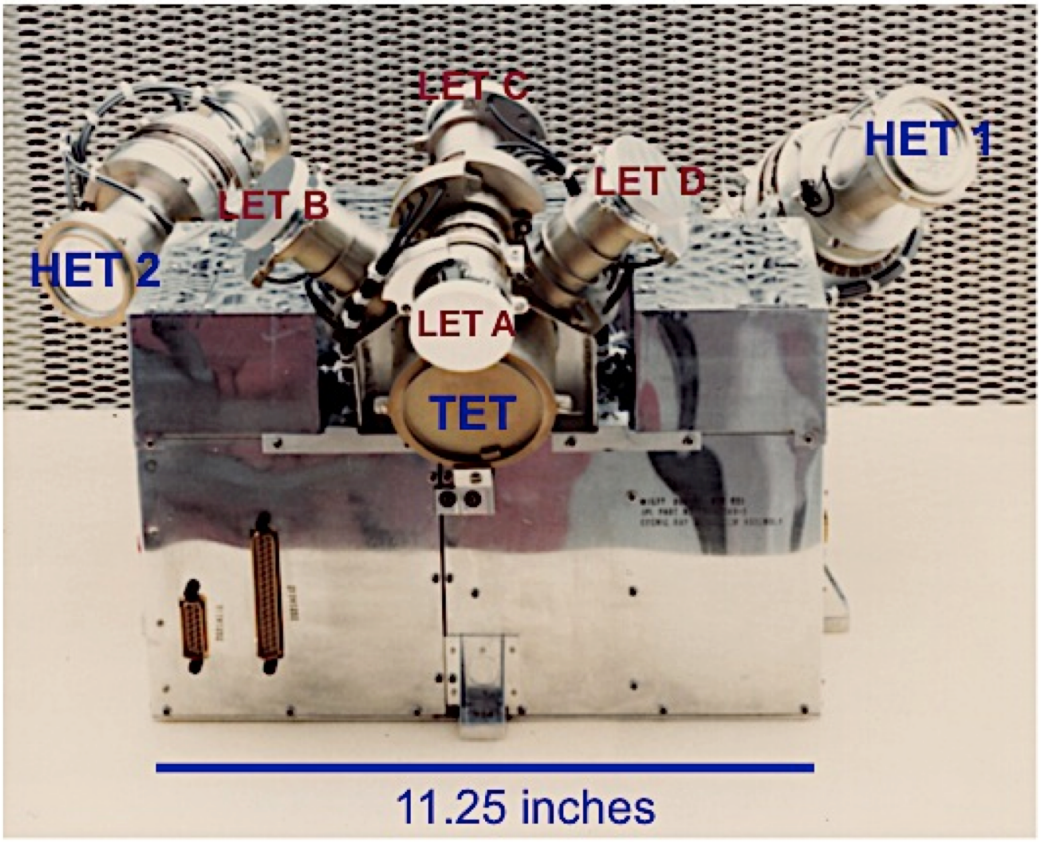


**Figure 2.1**. Image of Voyager's Cosmic Ray Subsystem (CRS)(courtesy of Voyager CRS instrument team).

a range-energy relation $R(E, Z, M)$. For high energies, the relation can be reasonably approximated by the power law:

$$R(E, Z, M) = \frac{\kappa M}{Z^2}\left(\frac{E}{M}\right)^{\alpha} \tag{2.1.1}$$

with $\alpha \approx 1.77$. The range of the particle entering the first detector is:

$$R = \frac{\kappa M}{Z^2}\left[\frac{(\Delta E + E')}{M}\right]^{\alpha}, \tag{2.1.2}$$

and a remaining range after entering the first detector and stopping in the second is:

$$R - L = \frac{\kappa M}{Z^2}\left(\frac{E'}{M}\right)^{\alpha}. \tag{2.1.3}$$

The approximation $M = 2Z$ can be used to solve for the charge using Equations 2.1.2 & 2.1.3 (small, known corrections are applied for nuclei where $M \neq 2Z$):

$$Z \propto \left[(E' + \Delta E)^{\alpha} - (E')^{\alpha}\right]^{\frac{1}{\alpha+1}} \tag{2.1.4}$$

A particle that passes through 3 or more detectors enables two independent charge estimates, which are useful for eliminating background events [51, 52].

### 2.1.2 CRS's Electronic Data System

As an ionized particle traverses the detector stack, it expends energy along the way by creating electron-hole pairs. In silicon, the energy required to generate a single electron-hold pair is $\epsilon = 3.62$ eV at 300 K, which is mainly dependent upon material properties and temperature as opposed to the particle's species and energy. The total ionization energy loss of the particle in the detector – $\Delta E$ in Equations 2.1.2 and 2.1.4 – is proportional to the total number of electron-hole pairs created within the active area of the detector.

In CRS, the charges are collected at each detector's semiconductor surface. The resulting small current pulse is fed to the onboard charge-sensitive preamplifiers and shaping amplifiers. The height of the output pulse – proportional to $\Delta E$ – is converted to a digitized signal for transmission by the pulse height analyzer (PHA). Signals from detector amplifiers are sent through an analog discriminator with a fixed threshold. Coincidence and anti-coincidence circuits for each telescope determine whether or not a specific logic requirement is met and determine the events for which pulse height analysis is carried out [48, 53].

## 2.2 High-Energy and Electron Telescopes

CRS's double-ended high-energy telescopes (HETs 1 & 2) and single-ended electron telescope (TET) have geometry factors and energy ranges appropriate

for observing GCR intensities and spectra in the LISM. Each telescope is

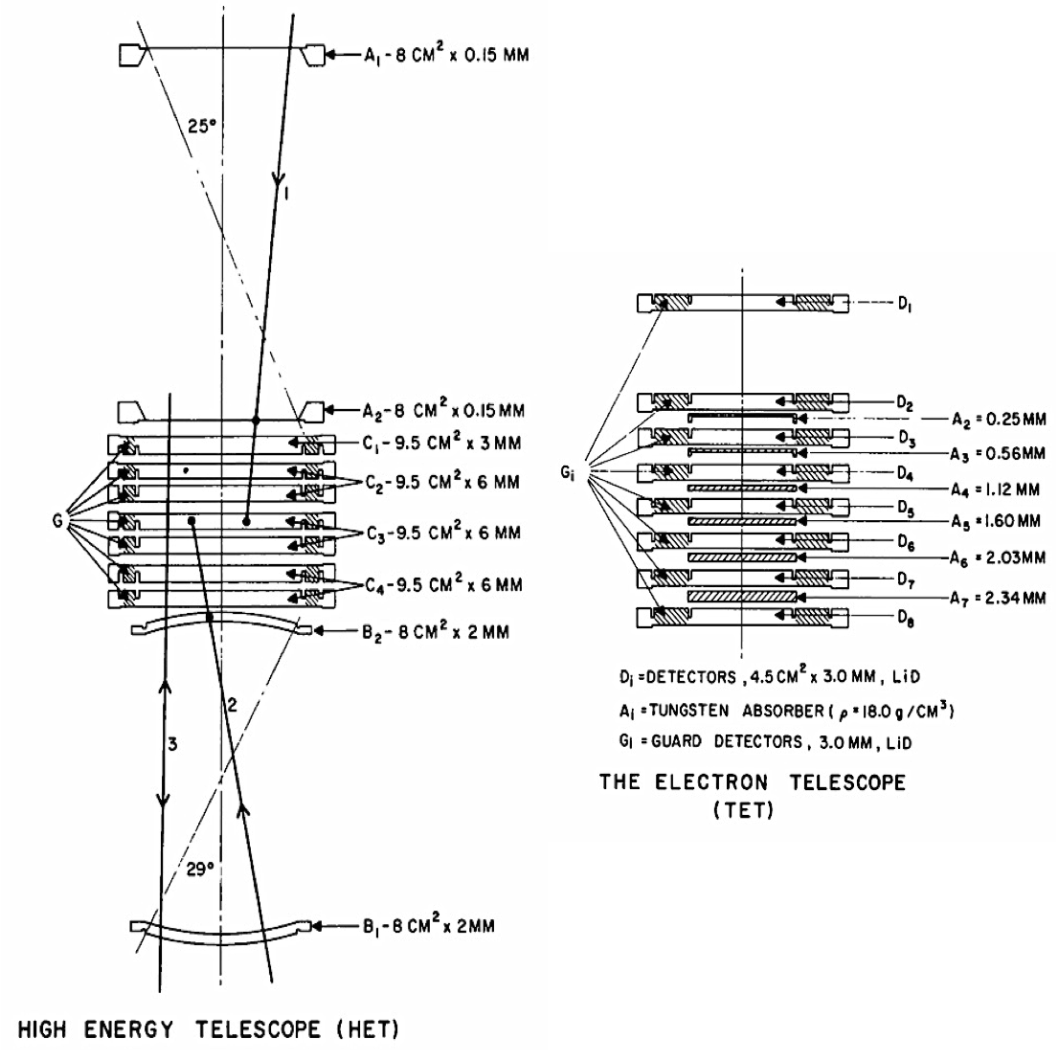


**Figure 2.2**. Schematic of the high-energy telescope (HET) and the electron telescope (TET) on Voyager's Cosmic Ray Subsystem (CRS). CRS also contains 4 low energy telescopes (LET), but since GCR's are primarily detected by HET and TET in the LISM, the LETs are not relevant to this work. Modified from Figure 6 of [48].

composed of circular energetic particle detectors arranged in a cylindrical stack, as shown in Figure 2.2. The two HETs each contain a central stack of 7 silicon solid-state detectors (C1 through C4) with annular guard rings (G) and end detectors consisting of 2 thin detectors on the A-end (A1 & A2) and 2 curved detectors on the B-end (B1 & B2). TET is a single-ended telescope composed

of 8 silicon detectors (D1 through D8) with annular guard rings ($G_i$) and interleaved with 6 tungsten absorbers (A2 through A7) [48].

### 2.2.1 Coincidence Logic and Operating Modes

In order to provide directional measurements for a variety of species over assorted energy ranges, CRS telescopes operate in multiple coincidence modes. The unidirectional modes indicate that a particle has stopped in a given telescope, while for bi-directional modes, particles penetrate through the entire stack of detectors from either end of the telescope. The modes of particular

| Mode | Telescope | Directionality | Dominant Species | Energy Range | Median Energy[3] | Coincidence Condition |
|---|---|---|---|---|---|---|
| **Guards** | HETs 1 & 2, TET | omnidirectional | protons | $\gtrsim$ 20 MeV | ∼460 MeV | G |
| **PENH** | HETs 1 & 2 | bi-directional | protons[1] | $\gtrsim$ 70 MeV | ∼540 MeV | B1·B2·C1 |
| **TAN** | TET | unidirectional | electrons[2] | ∼5 to ∼105 MeV | ∼13 MeV | D1·D2·D3·$\overline{\text{D8}}$·$\overline{\text{G}}$ |
| **BSp** | HETs 1 & 2 | unidirectional | protons | ∼18 to ∼70 MeV | ∼43 MeV | B1·B2·SB[4]·$\overline{\text{C1}}$·$\overline{\text{G}}$ |
| **BSe** | HETs 1 & 2 | unidirectional | electrons | ∼3 to ∼14 MeV | ∼6 MeV | B1·B2·C4·$\overline{\text{SB}}$·$\overline{\text{C1}}$·$\overline{\text{G}}$ |

**Table 2.1**. A summary of various CRS telescope modes.
(1) In addition to protons, PENH is ∼25% electrons (median energy ∼60 MeV) and ∼5% heavier nuclei ($\gtrsim$ 70 MeV/nuc) [1].
(2) TET's TAN rate has an estimated ∼4% proton background obtained by calculating the intensity-weighted averages ($J$) of the background percentages (Bkg %) of detectors D13 through D16 in Table 10 of [1] and also D17 (not listed in the table – acquired from Alan Cummings via private communication). See [1] for further details about the constituents of various CRS rates.
(3) Median energies calculated using spectra from: 1) the GALPROP DR propagation model for HET PENH, BSp, and Guard rates, 2) the Potgeiter model for TET's TAN rate, and 3) $J = E^{-1.3}$ for HET's BSe rate, all described in [1].
(4): SB is a slant threshold in the ΔE -E' plane which discriminates between ions and electrons of appropriate range (see [48]).

relevance for this study include a bi-directional proton-dominated mode (PENH) and a unidirectional mode that discriminates between electrons (BSe) and protons (BSp) on HETs 1 & 2, and a TET unidirectional electron mode (TAN)(summarized in Table 2.1). Additionally, the annular guard rings on each telescope operate as omnidirectional anti-coincidence counters.

## 2.3 Interstellar Spectrum

By applying the dE/dx-E technique to Voyager 1's interstellar measurements (Subsection 2.1.1), Cummings et al. (2016) presented the first low-energy spectra of galactic cosmic rays (GCR's) in the local interstellar medium (LISM), for nuclei with $1 \leq Z \leq 28$ down to 3 MeV and electrons down to 3.7 MeV from late 2012 through mid 2015 [1]. Electrons and protons are the dominant species in the LISM; their spectra are displayed in Figure 2.3. The electrons have a steeply falling spectrum, and their intensity exceeds that of protons up to a cross-over energy of $\sim$50 MeV. The proton intensity peaks between 10 and 50 MeV, and its overall shape remains flat and broad up to a few hundred MeV.

Related to the current work, PENH and Guard rate modes reflect intensities that are integrated over a very broad portion of the spectrum (see Table 2.1). As such, they have much better statistics than the modes with narrow energy ranges. However, their broader energy ranges make it difficult to determine whether or not the anisotropy has an energy dependence. Nonetheless, PENH and Guard rates are advantageous for characterizing the anisotropy's temporal evolution, as detailed in the following chapters. Moreover, since the LISM spectrum is mostly proton and electron dominated, B-stopping protons and electrons, as well as TET electrons are used to evaluate for species-dependent behavior.

## 2.4 Telescope Boresight Pointing Directions

Characterizing a pitch angle anisotropy requires reliable knowledge of CRS telescope boresight pointing directions. A brief description of terminology used in later chapters is included below; details about the procedure used to

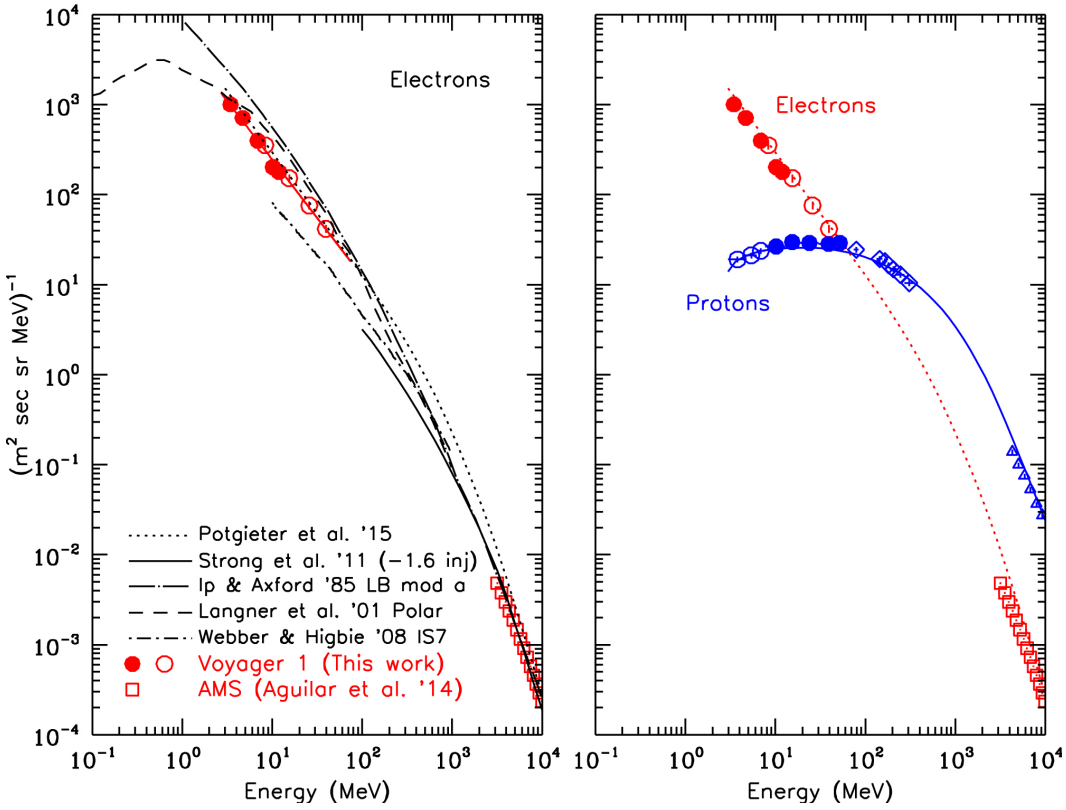


**Figure 2.3**. Electron and proton energy spectra from CRS on Voyager 1 from 2012, DOY 342 to 2015, DOY 181. The electron data was derived using TET and HET BSe observations. The proton data was derived from HET PENH and BSp measurements (recall Table 2.1). The dotted curve through the proton spectrum was calculated from a GALPROP model of protons in the LISM. This figure is from Figure 8 of [1].

determine CRS boresight orientations in conjunction with the spacecraft's daily position vector are recorded in Appendix A.

### 2.4.1 Spacecraft Cone and Clock Angles

The spacecraft coordinate system for both Voyagers is defined relative to the sun sensor's boresight (cone angle) and the star tracker's optical axis (clock

angle).[2.2] The sun sensors are located at 0° cone and star trackers[2.3] are at 0° clock. These locations, along with the cone and clock coordinates of the spacecraft's $\hat{S}_x$, $\hat{S}_y$ and $-\hat{S}_z$ axes are listed in Table A.1. CRS telescopes are also defined in terms of fixed cone and clock angle positions; these are used to convert from the telescope to the spacecraft coordinate system (see Appendix A, Table A.2 for listing of relevant cone and clock angle directions).

### 2.4.2 The R, T, N Coordinate System

R, T, N is a spacecraft-centered coordinate system where $\hat{\mathrm{R}}$ is the sun-to-spacecraft vector, $\hat{\mathrm{T}}$ is the cross product of the sun's rotation vector with $\hat{\mathrm{R}}$, and $\hat{\mathrm{N}}$ completes the triad of the right-handed system. Since data used by Voyager's instrument teams are often reported in R, T, N, it is the main coordinate system used throughout the current work.

Details of the procedure used to convert from CRS telescope cone and clock angle positions to boresight orientations in R, T, N are included in Appendix A (courtesy of Alan Cummings; personal communication). Applying the inverse transformations from R, T, N to other coordinates can be useful when relating Voyager's measurements to other missions such as New Horizons [54] or IBEX [55].

[2.2] The spacecraft cone and clock angles are not to be confused with the celestial cone and clock angles which are defined relative to the Sun and Voyager's reference star. The reference star has changed at least once on each spacecraft, but the original reference was Canopus.

[2.3] The sun sensor's boresight axis is aligned with the High Gain Antenna (HGA) and the star tracker is referred to as the "Canopus tracker" in early documentation.

# Chapter 3
# Observing the Anisotropy

## 3.1 CRS Omnidirectional and Directional Observations

Figure 3.1 shows LECP and CRS count rates in the LISM from 2012.5 through 2017. LECP's > 211 MeV protons reveal the anisotropy's signatures in the form of long-duration, time-varying intensity changes, present in sectors 1 & 5 but not in other sectors (Figure 3.1a). LECP has an advantage for viewing the pitch angle anisotropy because its stepper-motor platform enables its bi-directional telescope to regularly change orientation (Figure 3.2).

CRS's telescopes are body-fixed on the 3-axis stabilized spacecraft (Figure 2.1). As such, it mainly detects the anisotropy through its omnidirectional anti-coincidence guard counters (Figure 3.1b). Because they measure particles with all pitch angles, these detectors continuously monitor the temporal intensity changes without providing pitch angle information. The omnidirectional rates have the highest statistics of all of the rates available on CRS (several hundred cts/sec) and show a time-varying intensity response similar to that of LECP.

Detecting the anisotropy using CRS's directional observations presents a greater challenge. HET 1, HET 2, and TET fields of view do not typically observe particles with $\sim 90^\circ$ pitch angles, so their nominal rates are not sensitive to the anisotropy (see for example, HET 1's bi-directional PENH rate shown in Figure 3.1c). However, data taken while telescope fields of view rotate during occasional spacecraft maneuvers provide an opportunity to examine the pitch angle variation of the intensity at specific times.

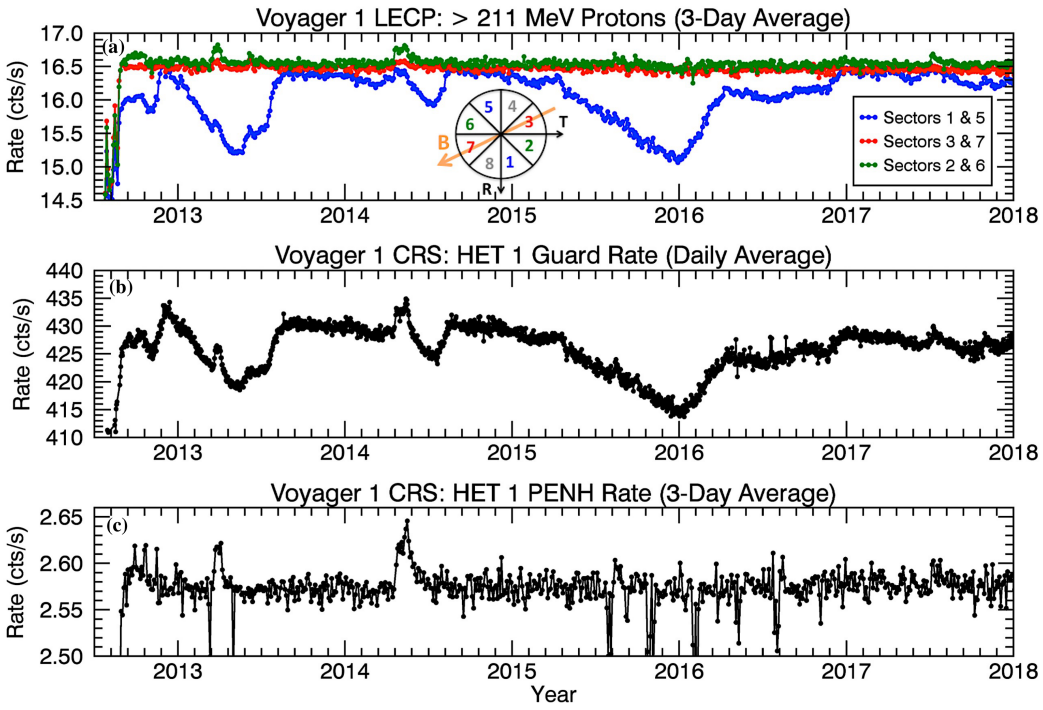


**Figure 3.1**. LECP and CRS counting rates in the LISM from 2012.5 through 2018. (a) LECP's > 211 MeV protons reveal the GCR pitch angle anisotropy. The magnetic field direction lies in sectors 3 & 7, while sectors 1 & 5 are approximately perpendicular to the field direction, as illustrated by the circular diagram (background-corrected data is courtesy of Rob Decker and the LECP team; for LECP's non-corrected, publicly-available data, see: http://sd-www.jhuapl.edu/VOYAGER/index.html). (b) CRS's omnidirectional rate ($\gtrsim$ 20 MeV; proton-dominated) from anti-coincidence guard counters on the HET 1 telescope show similar time dependence to LECP's sectors 1 & 5. (c) CRS's bi-directional PENH rate on HET 1 ($\gtrsim$ 70 MeV; proton-dominated) is fairly steady in the LISM, in agreement with LECP's bi-directional rates in sectors 2 & 6 and 3 & 7. Two types of deviation arise from: (1) shock-related increases (e.g. 2014.35), and (2) decreases observed during 70°-offset spacecraft maneuvers (e.g. 2015.59).

## 3.2 Magnetometer Roll Maneuvers and Observations

Magnetometer roll maneuvers are performed ∼6 times per year for calibration purposes of Voyager 1's magnetometer (MAG). They originally consisted of 10 successive 360° turns about the spacecraft's Earth-pointing axis (approximately $\hat{\mathrm{R}}$ in the R, T, N coordinate system), but as of 2017 are now performed with a

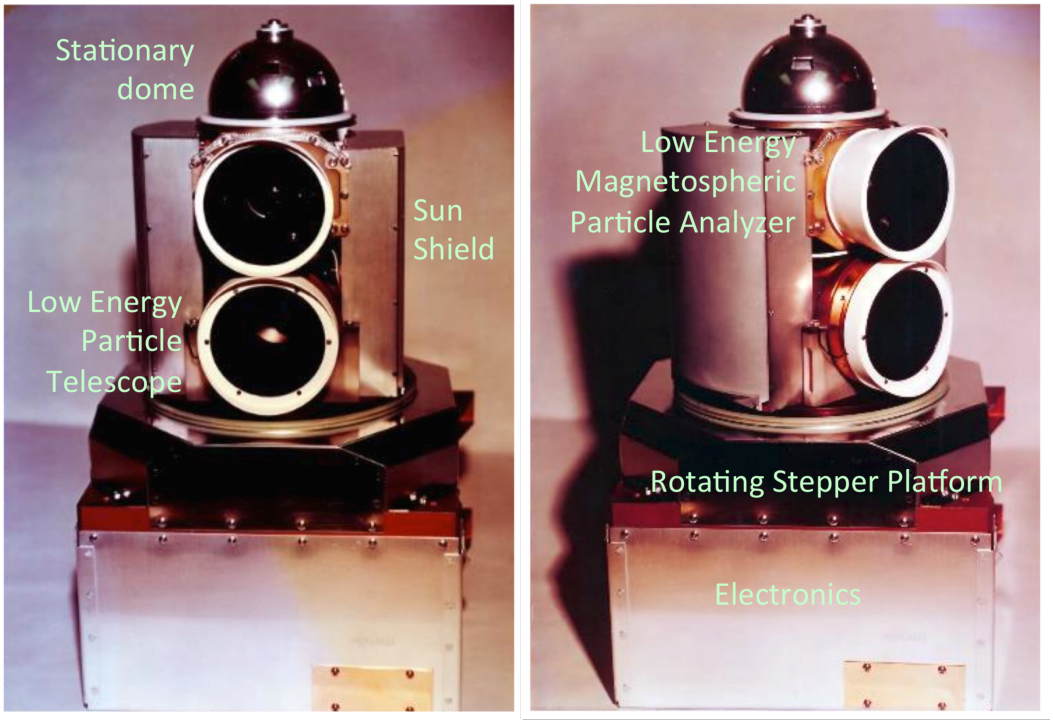


**Figure 3.2**. Images of Voyager's Low Energy Charged Particle Instrument (LECP)(from LECP's website: http://space.umd.edu/group_photos/LECP_pictures.html).

reduced number of turns because of power limitations. During the 10-roll time period (∼5.6 hours), CRS telescope fields of view smoothly and continuously rotate 360° every 2,000 s (0.18°/sec), which translates to an 8.6° angular averaging interval per point in the highest-resolution data (48-s). "Clock angle" refers to the angle of the boresight in the N-T plane with the $\hat{\text{N}}$-axis as the origin and the angle increasing towards $\hat{\text{T}}$. "Roll epoch" refers to the set of 10 turns which took place on a particular day (e.g. the 2015-310 epoch occurred on day 310 of 2015). Knowing the roll rate, the magnetic field direction, and the clock angle orientation of a telescope's boresight enables the average pitch angle of particles entering the telescope to be determined during each 48-s interval throughout a roll maneuver.

HET 1 and HET 2 bi-directional PENH measurements during roll maneuvers

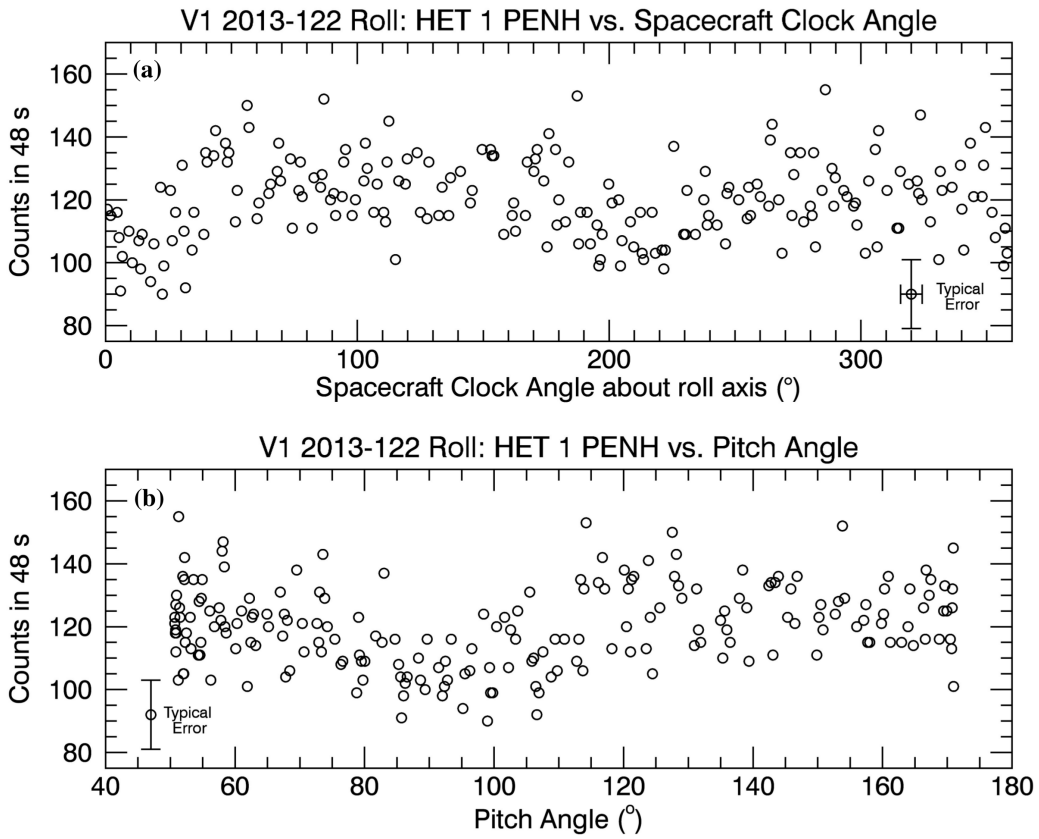


**Figure 3.3**. HET 1's bi-directional PENH rate ($\gtrsim$ 70 MeV; proton-dominated) vs. clock angle (a) and pitch angle (b) during the 2013-122 roll epoch. The magnetic field for this epoch was (0.176, -0.422, 0.188) nT in R, T, N (from the MAG's publicly-available data: https://omniweb.gsfc.nasa.gov/coho/form/voyager1.html). Anisotropy-related minima occur near $\sim$11° and $\sim$217° in clock angle space, which transform to 90° in pitch angle space. The spacecraft's continuous rolling motion over 48-s interval produces an 8.6° angular averaging per point. The horizontal line on the typical error reflects this 8.6° angular average in clock space, while the vertical line reflects the statistical uncertainty in the number of counts.

confirm that the reduction observed by LECP's sectors 1 & 5 (Figure 3.1a) and CRS's omnidirectional rates (Figure 3.1b) results from a pitch angle anisotropy. Figure 3.3 and Figure 3.4 depict the highest-time-resolution PENH counts (48-s data intervals) for HET 1 & 2 during the 2013-122 roll epoch. As evident by the two minima observed in each telescope, HET 1 and HET 2 fields of view pass through the anisotropy region twice during their 360° rotations in clock-angle space (Figures 3.3a & 3.4a). For HET 1, the minima occur

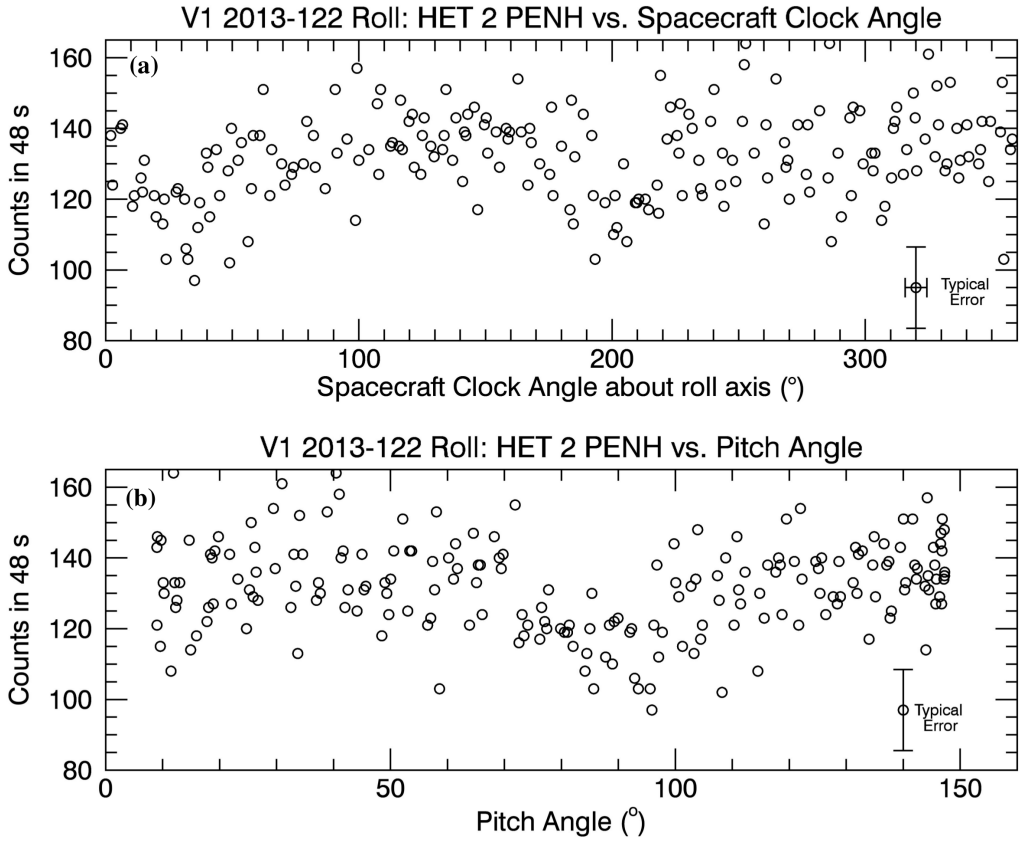


**Figure 3.4**. HET 2's PENH rate vs. clock angle (a) and pitch angle (b) for the same roll epoch as Figure 3.3. Although HET 2's differing orientation shifts the minima to ∼29° and ∼200° in clock angle space, these locations also transform to 90° in pitch angle space.

near ∼11° and ∼217° clock angle (Figure 3.3a), translating to 90° in pitch angle space (Figure 3.3b). HET 2's minima near ∼29° and ∼200° clock angle (Figure 3.4a) and are also centered on 90° pitch angle (Figure 3.4b).

Overall, CRS data taken during roll maneuvers provide the clearest measure of the anisotropy's spatial distribution. Figure 3.5 displays a superposition of HET 1 (Figure 3.5a) and HET 2 (Figure 3.5b) rates during 7 rolls where the anisotropy is most prominent (listed in Appendix C). Although the effects of its time-variable magnitude are also present, not only does the anisotropy occur within a region perpendicular to the magnetic field – in agreement with

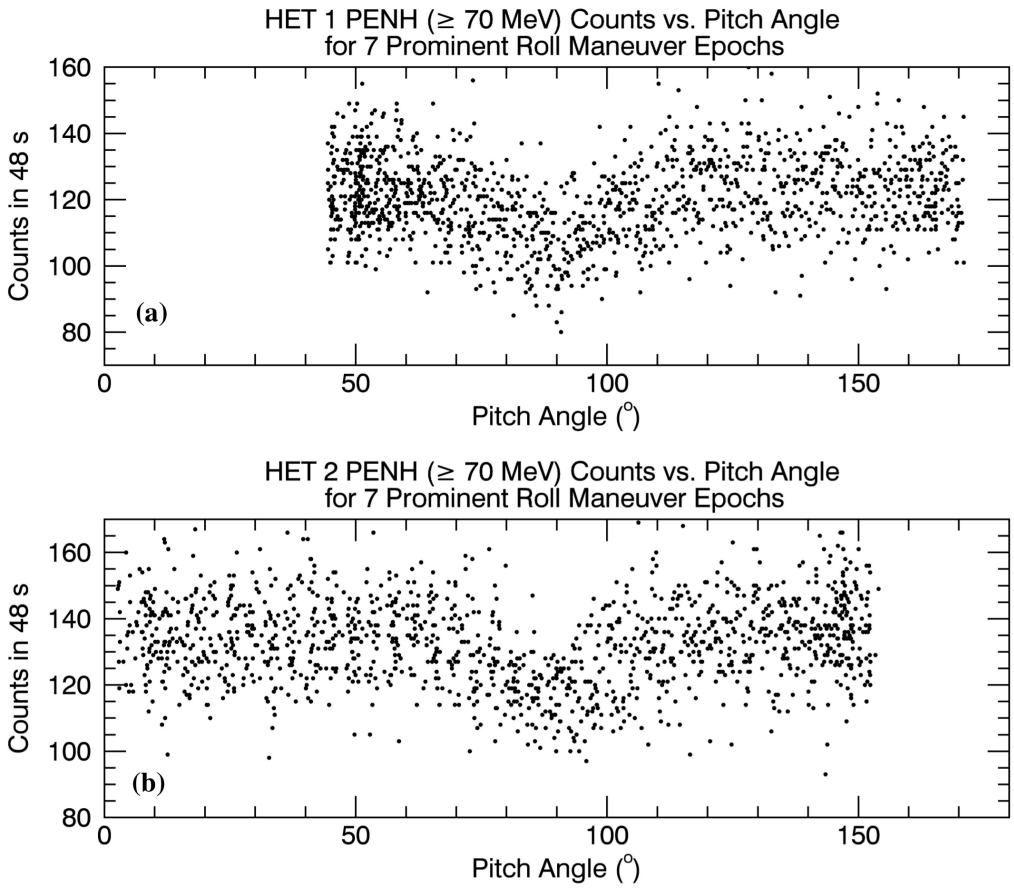


**Figure 3.5**. Superposition of 7 prominent HET 1 (a) and HET 2 (b) roll maneuver epochs of varying anisotropy magnitudes arranged in pitch angle space (see Appendix C for a listing of selected epochs).

LECP's observations – but it is also distributed about 90° pitch angle.

## 3.3 70°-offset Maneuvers and Observations

70°-offset maneuvers were introduced on Voyager 1 in March 2011 to provide a way for LECP to measure heliosheath plasma flow velocity in the direction not seen in its usual configuration [56] and were discontinued in 2017. Like magnetometer roll maneuvers, they require the spacecraft to roll about the $\hat{\mathrm{R}}$-axis. However, rather than rolling continuously, the spacecraft rotates to a clock angle offset of 70° and parks for up to 5 hours before returning to

its usual orientation. These maneuvers typically occur on consecutive days over a multiple-day period, usually in the temporal vicinity of a roll maneuver. Figure 3.6 shows average HET 1 PENH rates during the 2015-296 "offset epoch", where DOY 296 is the first day of the sequence of 7 maneuvers that took place on days 296 to 312 of 2015; this is the epoch in nearest proximity to the 2015-310 roll maneuver.

| Telescope | Average Nominal Boresight Pitch Angle | Average 70° -Offset Boresight Pitch Angle | Field of View (Full Angle) |
|---|---|---|---|
| **HET 1** | $136° \pm 3°$ (A-end) | $77° \pm 3°$ (A-end) | 40° (PENH) |
| | $44° \pm 3°$ (B-end) | $103° \pm 3°$ (B-end) | 58° (B-stopping) |
| **HET 2** | $31° \pm 4°$ (A-end) | $69° \pm 3°$ (A-end) | 40° (PENH) |
| | $149° \pm 4°$ (B-end) | $111° \pm 3°$ (B-end) | 58° (B-stopping) |
| **TET** | $135° \pm 5°$ | $88° \pm 3°$ | 60° (TAN) |

**Table 3.1**. A summary of CRS telescope boresight directions in pitch angle space. Note that particles entering a given telescope travel in directions opposite to the telescope's average boresight direction and field of view. Averages were determined using telescope and magnetic field directions from ∼2012.65 to 2017.0. The average magnetic field during this period was (0.143, -0.401, 0.179) nT in R, T, N. Uncertainties reflect variations in the magnetic field direction and changes in telescope orientation due to the small difference between Voyager's actual earth-to-spacecraft vector and the sun-to-spacecraft vector used in the R, T, N coordinate system (see Appendix B, Section B.1).

During 70°-offsets, both HET 1 and TET fields of view overlap with 90° pitch angle, thus allowing for bi-directional and unidirectional measurements from fixed orientations to complement roll maneuver and omnidirectional observations of the pitch angle anisotropy. Counts from multiple days are combined to reflect a single value for each offset epoch and are normalized to temporally adjacent non-offset values in order to determine a relative intensity change arising from the pitch-angle anisotropy ($\delta_{70°}$). Modes relevant to 70°-offsets include HET 1's bi-directional proton-dominated PENH rate, unidirectional B-stopping proton rate (BSp), and unidirectional B-stopping electron rate (BSe), as well as TET's unidirectional electron-dominated TAN rate (Table 2.1). The anisotropy's temporal evolution can be examined to see if its properties vary

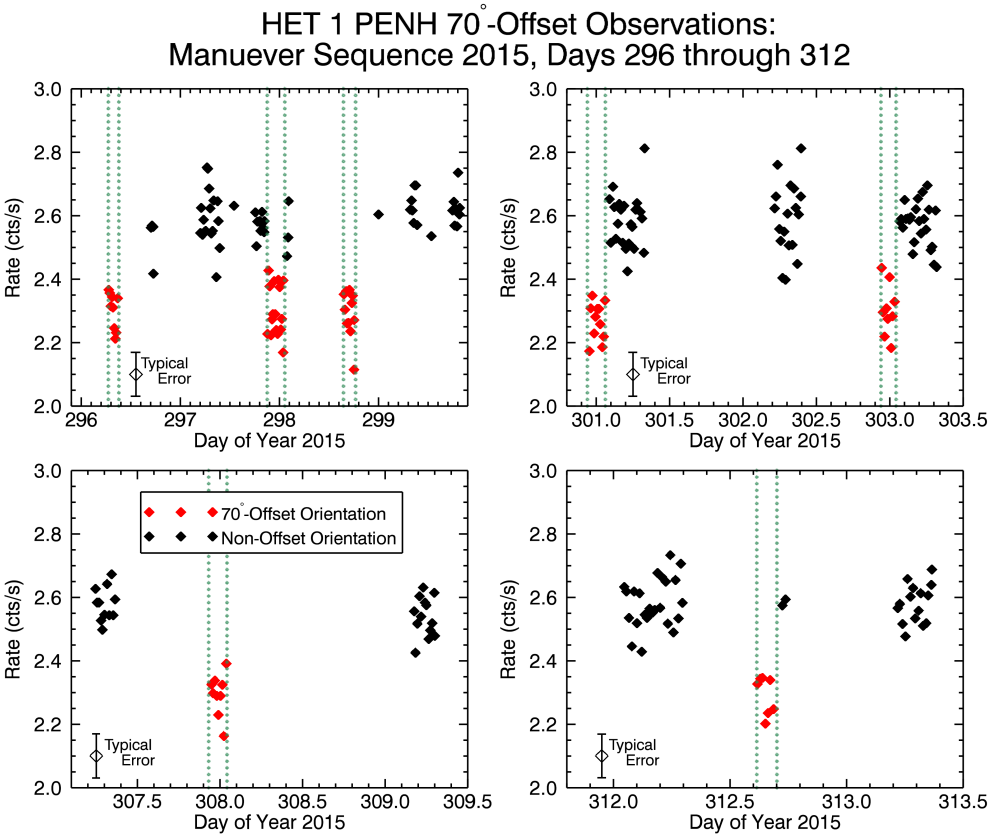


**Figure 3.6**. HET 1 PENH ($\gtrsim$ 70 MeV; proton-dominated) 70°-offset observations for a full sequence of maneuvers that took place in 2015, on days 296 to 312. Note that offset maneuvers take place within a subset of time over a period of multiple days, in contrast with roll maneuvers which take place on a single day. The roll maneuver proximate to this 2015-296 offset epoch occurred on day 310 of 2015. The results of the 70°-offset observations will be addressed much later (in Chapter 5), but Appendix F, Table F.1 contains a detailed list of the days during which the offset maneuvers occurred for all epochs from late 2012 through the end of 2016. In the current plot, points are averaged over ∼480-s intervals for visualization purposes. The large data gaps are an indication of Voyager 1's daily gaps in communication with Earth. The dotted lines denote the times when the spacecraft was fixed in the offset position. The red points indicate observations taken while the spacecraft was parked at the 70°-clock-angle offset from its usual position. The black points represent values obtained while the spacecraft was in its nominal orientation. Since HET 1's field of view includes 90° pitch angle during 70°-offsets (Table 3.1), it sees a reduction of counts indicative of the anisotropy.

between protons and electrons due to their differing masses, charges, velocities, and rigidities.

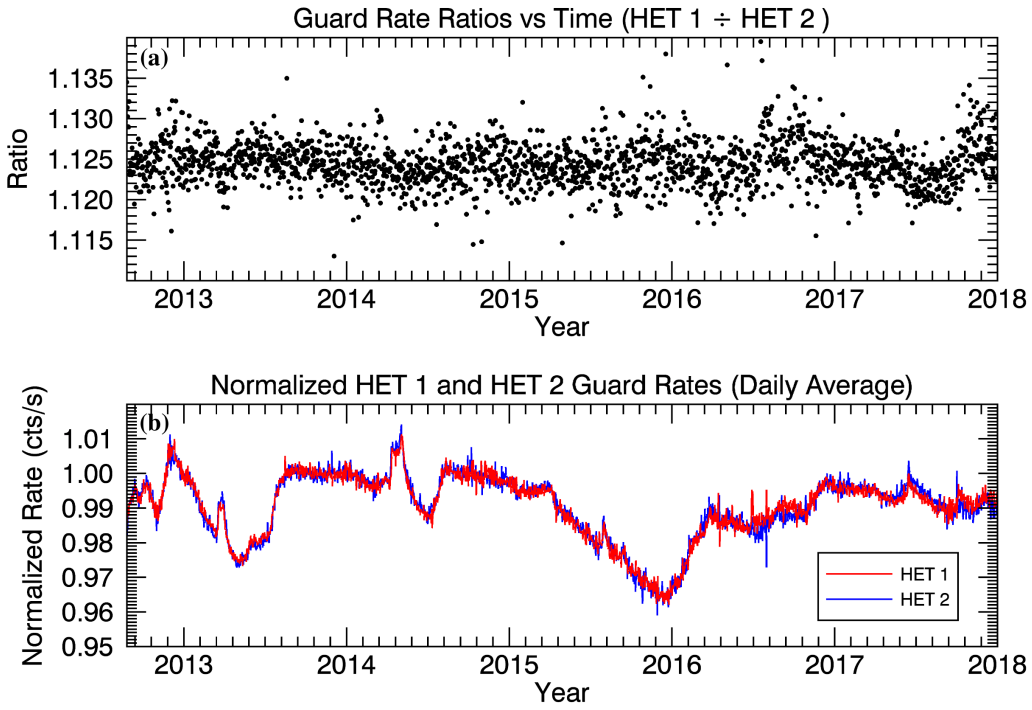


**Figure 3.7**. A comparison of HET 1 and HET 2 omnidirectional (guard) rates.
(a) HET 1 and HET 2 integral omnidirectional (guard) rates reflect a constant offset of roughly 11%, but follow each other closely in their temporal variation to within 0.6%.
(b) Superposition of HET 1 and HET 2 omnidirectional (guard) rates, each normalized by their respective isotropic values (430.0 cts/s for HET 1 and 382.4 cts/s for HET 2; see text).

## 3.4 Omnidirectional Observations

An omnidirectional intensity reduction ($\delta_{\text{omni}}$) is determined by comparing observations of each epoch's daily average to the average rate during 2013.6 to 2014.1 – a time period when the pitch angle anisotropy is not present (note the steady rates in Figures 3.1a & 3.1b). The average isotropic rates used for normalization are $430.01 \pm 0.06$ cts/s for HET 1 and $382.38 \pm 0.06$ cts/s for HET 2.

Although the integral counting rates between HET 1 and HET 2 guards differ by $\sim$11% as a result of differing electronic threshold levels, the ratio

between the two remains constant to within 0.6% (see Figure 3.7).

Referring back to Figure 3.1b, the three main episodes of GCR intensity changes caused by the pitch-angle anisotropy last on the order of 265, 100, and 630 days and exhibit at most ∼2.6%, ∼1.3%, and ∼3.8% intensity reductions, respectively. A fundamental assumption about CRS's omnidirectional observations is that these long-duration intensity changes arise primarily from the pitch-angle anisotropy, as opposed to additional effects such as solar modulation, a radial gradient, or diffusive or convective flows. This assumption is well-supported by the following examination of data taken when the spacecraft was in its nominal orientation and during roll maneuvers.

## 3.5 Additional Forms of Anisotropy

The possibility of a radial cosmic ray intensity gradient in the local interstellar medium was initially explored by [1], who examined the intensity of CRS protons in 4 energy bands as a function of Voyager 1's distance from the sun. They concluded from linear fits that the radial gradient is consistent with zero over an energy range of 3 to 346 MeV. This trend continues through present (mid-2018), even at ∼20 AU beyond Voyager 1's heliopause crossing. An updated version of their Figure 2 is shown in Figure 3.8, courtesy of the Voyager CRS team.

Complementing these spectral observations, Figure 3.9 shows the results of linear least squares fits to HET 1 (a) and HET 2 (b) bi-directional PENH rates from 2012.8 to 2018.0 – excluding events recorded during spacecraft maneuvers and shock transients.[3.1] Although the telescopes differ in their

[3.1] See column 1 of Table D.1 (Appendix D) and column 2 of Table F.1 (Appendix F) for a listing of the roll maneuver and 70°-offset days, all of which are excluded from these fits. Three shock transient events occurring from 1) 2013-73 (2013.200) to 2013-109 (2013.299), 2) 2014-100 (2014.275) to 2014-155 (2014.425), and 3) 2015-210 (2015.575) to 2015-255 (2015.699) were also excluded.

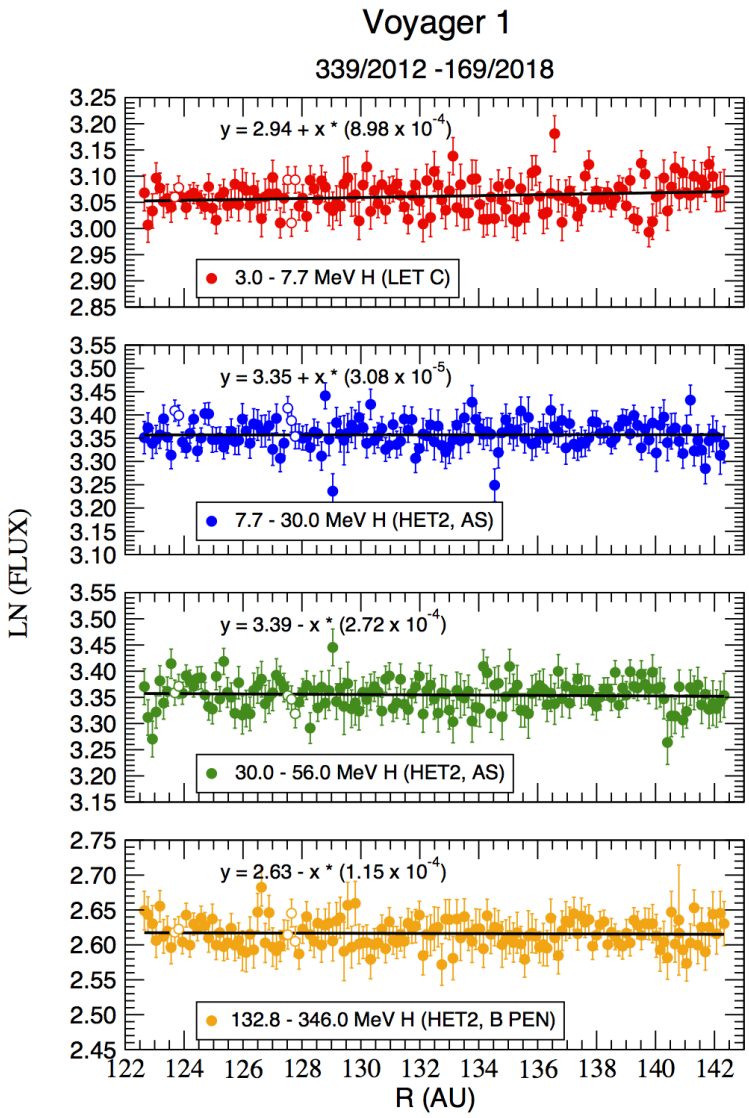


**Figure 3.8**. CRS proton intensity in 4 energy bands vs. Voyager 1's heliocentric radial distance (AU) over the 2012-339 to 2018-169 time period with shock-related transients (open symbols) excluded. Intensities are in units of $(\mathrm{m}^2\ \mathrm{s\ sr\ MeV})^{-1}$. Linear fits show a radial gradient consistent with zero. The average for the 4 modes is $0.02 \pm 0.02$ %/AU. This is an updated version of Figure 2 from [1] generated by the Voyager CRS team.

viewing orientation (Table 3.1), the slope is small for HET 1 and HET 2 ($0.0010 \pm 0.0003$ cts/s/year). Normalizing by the mean rates ($2.57 \pm 0.04$ cts/s for HET 1; $2.82 \pm 0.04$ cts/s for HET 2) and converting from time to distance (Voyager 1's speed is 17 km/s = 3.58 AU/year), this translates to an intensity change of $0.01 \pm 0.003$ %/AU, revealing a negligible radial gradient consistent

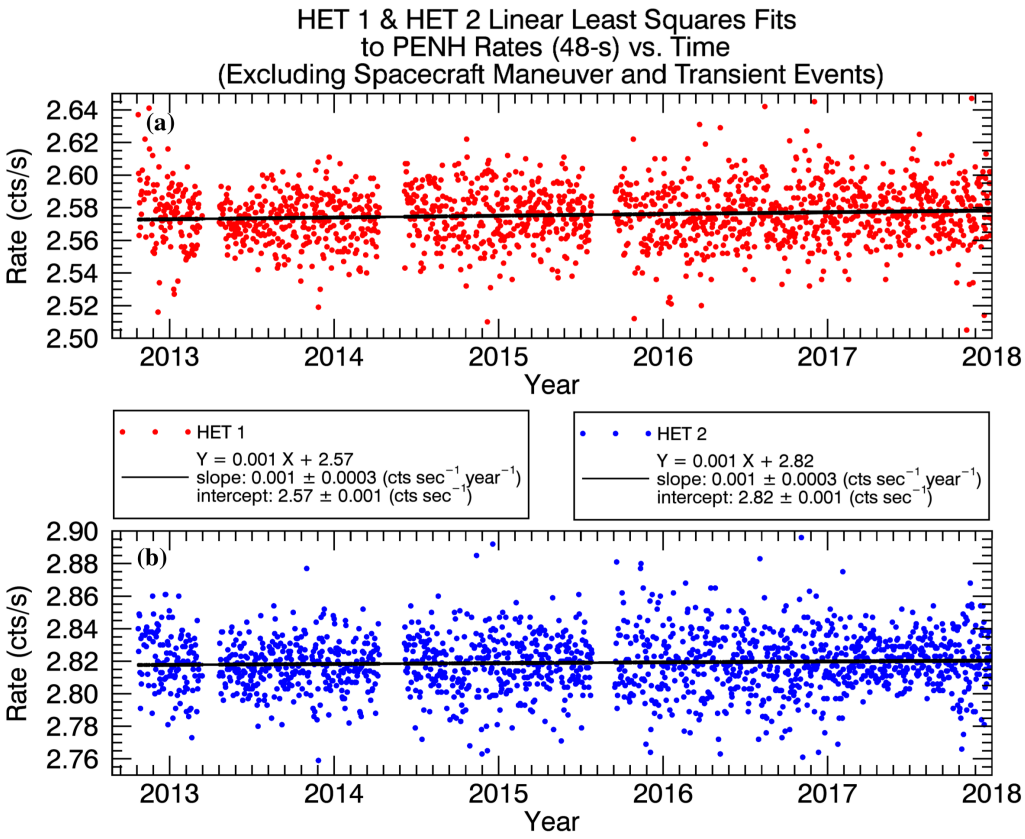


**Figure 3.9**. Linear least squares fits to HET 1 and HET 2 bi-directional PENH rates ($\gtrsim$ 70 MeV; mostly protons) while the spacecraft is in its usual configuration (maneuver events and shock transients excluded). The negligible slopes are consistent with no significant radial gradient.

with Figure 3.8.

Roll maneuvers provide a unique opportunity to assess whether or not additional forms of anisotropy may be present. LECP's pitch angle anisotropy observations fall within a single 45°-sector centered at 90° pitch angle, which sets an upper limit to the affected region's extent. These effects are removed by excluding the data when telescope boresight pitch angles are oriented at $67.5° < \alpha < 115.5°$. Using the pitch-angle anisotropy-excluded data, a search is made for possible first-order anisotropies – such as diffusive or convective flows – by solving for the Compton-Getting anisotropy parameters ($\delta$ and $\theta_0$)

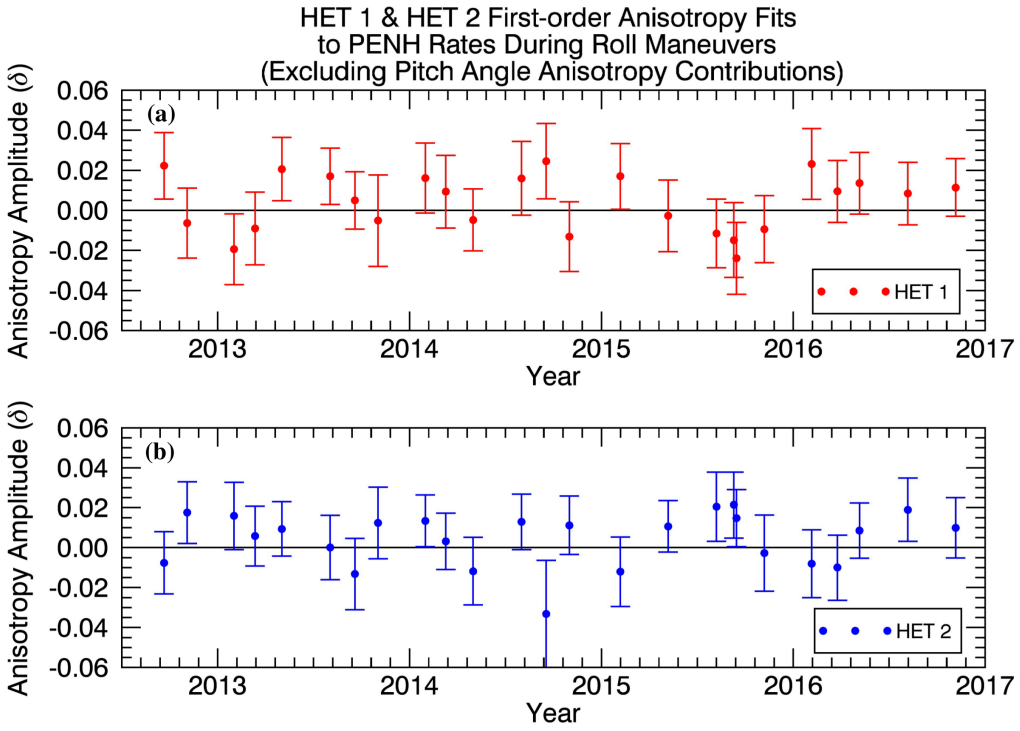


**Figure 3.10**. First-order anisotropy amplitudes, $\delta$, from Compton-Getting fits to bi-directional 48-s PENH rates ($\gtrsim$ 70 MeV; mostly protons) during HET 1 (a) & HET 2 (b) roll maneuvers (excluding pitch angle anisotropy effects) for 25 epochs from late 2012 through the end of 2016 (fit parameters are listed in Appendix C, Tables C.1 & C.2).

from fits to $I = I_0(1 + \delta\cos(\theta - \theta_0))$. Here, $I$ is the count rate, $I_0$ is the mean rate excluding the pitch-angle anisotropy, $\delta$ is the anisotropy amplitude, $\theta$ is the telescope boresight clock angle, and $\theta_0$ is the boresight clock angle at which maximum intensity occurs. A similar procedure was applied to Voyager 2's roll maneuver data in 2017 by [5], who discovered a flow anisotropy of anomalous cosmic rays in the inner heliosheath. Parameters from fits to each of the 25 roll epochs from late 2012 through the end of 2016 are listed in Appendix C, Tables C.1 & C.2. The resulting first-order anisotropy amplitudes ($\delta$) are shown in Figure 3.10. Weighted averages of all epochs reveal amplitudes of $\delta = 0.005 \pm 0.003$ for HET 1 and $\delta = 0.006 \pm 0.003$ for HET 2, indicating that the first-order anisotropies are small, at most.

These results, along with LECP's sectored rates (2 & 6, 3 & 7) provide strong evidence that the small, long-term deviations in intensity observed by Voyager 1 primarily arise from particles with near 90° pitch angles that are missing in an otherwise uniform, steady intensity distribution. Not only does this support CRS's directional observations, but it also implies that the omnidirectional rates can serve as a reliable measure of intensity changes caused by the evolution of the anisotropy over time.

# Chapter 4
# Characterizing the Anisotropy

## 4.1 Theory: Relating Detector Count Rates to Cosmic Ray Intensities

In general, the coincidence rate of any particle telescope is dependent on both the intensity of the radiation environment as well as the telescope's geometrical properties such as individual detector areas and relative spacing of elements within the stack.

For an ideal telescope – one having 100% detection efficiency and negligibly thin detectors so as to minimize energy loss – the count rate of particles passing through the telescope, $C$, is related to intensity, $I$, by a constant of proportionality known as the geometry factor, $G$, via the relation: $C = GI_0$, where $I = I_0$ for an isotropic intensity and $G$ depends upon the telescope response function, $A(\omega)$:

$$G = \int_\Omega \mathrm{d}\omega A(\omega) = \int_\omega \mathrm{d}\omega \int_S \mathrm{d}\vec{\sigma} \cdot \hat{r}. \tag{4.1.1}$$

$\omega$ represents the element of solid angle. In terms of polar ($\theta$) and azimuth ($\phi$), $\omega = \mathrm{d}\phi\ \mathrm{dcos}\,\theta$. $\Omega$ is the domain of $\omega$ and can be limited by other telescope sensors. $S$ is the last sensor's total area, $\vec{\sigma}$ is the element of the last telescope sensor to be penetrated, $\vec{r}$ is a unit vector in direction $\vec{\omega}$, and $\hat{r} \cdot \mathrm{d}\vec{\sigma}$ is an effective element of area looking into $\vec{\omega}$.

The above equation can be solved for a few simplified cases. For instance, the geometry factor of a single-element telescope with area $A = \int_\Omega \mathrm{d}\vec{\sigma}$ is:

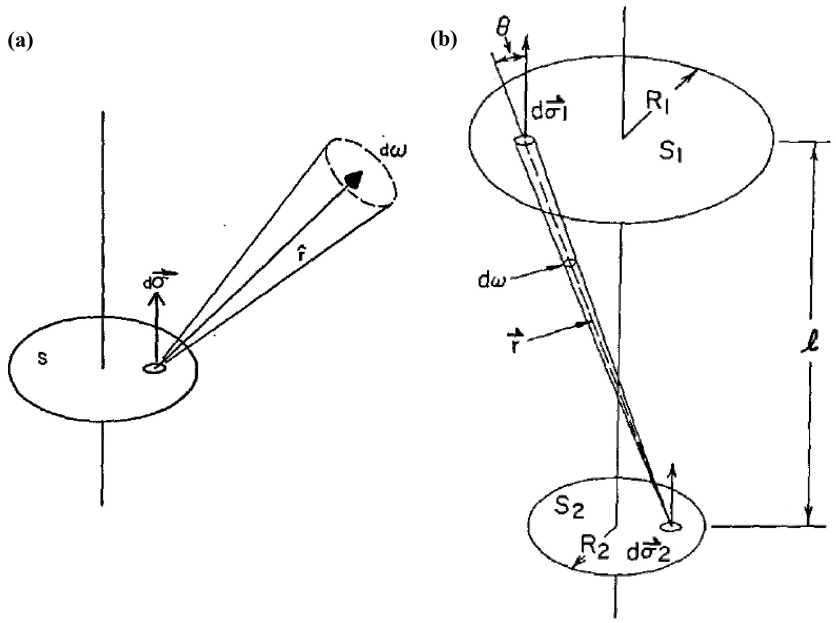


**Figure 4.1**. Depiction of single-element (a) and double-element (b) particle telescopes used to illustrate geometry factors described in Equations 4.1.2 & 4.1.3.
(a) Single-element telescope consisting of a circular, planar detector viewing one hemisphere, with radius $R$, total area $S$, and surface area element $\mathrm{d}\vec{\sigma}$. From Figure 1 of [2].
(b) Two-element telescope arranged in a cylindrical configuration. The two circular detectors are spaced at a distance $l$ and have radii $R_1$ and $R_2$, total areas $S_1$ and $S_2$, and surface area elements $\mathrm{d}\vec{\sigma}_1$ and $\mathrm{d}\vec{\sigma}_2$, respectively. From Figure 2 of [2].

$$G = \int_\Omega \int_S \cos\theta \; \mathrm{d}\vec{\sigma} \; \mathrm{d}\omega = 2\pi A \int_0^1 \cos\theta \; \mathrm{d}\cos\theta = \pi A \tag{4.1.2}$$

(illustrated in Figure 4.1a). Here, $\Omega$ is not limited by any other sensors. This example is for particles seen from one direction; if the telescope receives particles from both sides, Equation 4.1.2's result doubles.

The geometry factor for a two-element telescope with circular symmetry is also straightforward to determine analytically [2]:

$$G = \frac{\pi^2}{2} \; [R_1^2 + R_2^2 + l^2 + \{(R_1^2 + R_2^2 + l_2^2)^2 - 4R_1^2 R_2^2\}^{\frac{1}{2}}]. \tag{4.1.3}$$

In Figure 4.1b's illustration, detector 2 is the last to be penetrated, so $S = S_2$ and $\mathrm{d}\vec{\omega} = \mathrm{d}\vec{\omega}_2$ in Equation 4.1.1. Moreover, its domain $\Omega$ is limited by detector 1. As such,

$$G = \int_{\Omega} \int_{S_2} (\mathrm{d}\vec{\sigma} \cdot \hat{r}) \, \mathrm{d}\omega \tag{4.1.4}$$

and

$$\mathrm{d}\omega = \frac{\hat{r} \cdot \mathrm{d}\vec{\sigma_1}}{r^2}, \tag{4.1.5}$$

leading to:

$$G = \int_{S_1} \int_{S_2} \frac{(\mathrm{d}\vec{\sigma_1} \cdot \hat{r})(\mathrm{d}\vec{\sigma_2} \cdot \hat{r})}{r^2}. \tag{4.1.6}$$

Since $\frac{\hat{r} \cdot \mathrm{d}\vec{\omega}}{r} \leq \frac{\mathrm{d}\sigma}{l}$ and $\int_S \mathrm{d}\sigma$ is just the detector area $A$, it follows from Equation 4.1.5 that $G \leq \frac{(A_1 A_2)}{l^2}$ [2].

Although these basic principles apply to count rates on Voyager 1, simulating CRS response functions is not as straightforward as using the analytical approach of Equation 4.1.1. This is because telescope orientations change during spacecraft maneuvers and characterizing an anisotropy is of primary interest. Therefore, rather than integrating an explicit formula, a more general and efficient Monte Carlo method is used to simulate HET 1 & 2 response functions during roll maneuvers and 70°-offsets, and through this, several models accounting for the anisotropy are explored.

## 4.2 Monte Carlo Simulation of Telescope Response Functions

Directional response functions of CRS telescopes obtained from Monte Carlo simulations for each roll maneuver and 70°-offset epoch, together with an analytical representation of the omnidirectional response function provide the foundational basis for modeling the anisotropy.

For directional measurements, the condition for particles to pass entirely through a given telescope renders itself nicely to a two-element telescope model, like that of Equation 4.1.3. Referring back to Chapter 2, the two high-energy

telescopes, HET 1 and HET 2, are double-ended. Thus, particles may enter the A-end of the telescope, entering through C1 and exiting through B1, or particles may enter the B-end of the telescope, entering through B1 and exiting through C1 (see Figure 2.2).

Details of the Monte Carlo procedure used to numerically simulate particles passing through HET 1 and HET 2 are included in Appendix B. One can control angular resolutions and count rates to produce results with high enough statistics that the uncertainties in the numerical simulation are negligible compared to the data. Moreover, after accumulating millions of particles, simple sanity checks are employed to verify known parameters such as telescope viewing angle and geometry factor, as well as the observed distribution of particles in pitch angle and clock angle space.

## 4.3 Characterizing the Anisotropy via "Notch" Models

One way to model the anisotropy is to assume some percentage of particles drop out within a region of some width centered at 90° pitch angle, hence creating a "notch" in the otherwise uniform pitch angle distribution, and thereby an overall reduction in the omnidirectional and directional GCR intensities. In principle, the shape of the boundaries of the missing particle region – the notch's geometry – may manifest in a variety of forms. For example, it may have abruptly falling edges or a more gradual slope as a function of pitch angle. Additionally, the missing particle region might be completely empty or partially filled. Each of these cases can be represented by two parameters: 1) the notch's width and 2) its depth, which could result from scattering.

Indeed, ascertaining a precise shape may provide useful insights about the anistropy's underlying physical mechanisms, but in practice, extracting detailed information about the notch's geometry is a challenge. This is be-

cause CRS's omnidirectional and directional rates are a mixture of temporal (48-s) and spatial averaging. Also, the sporadic nature of the spacecraft maneuvers (∼6 times/year) adds to the statistical limitations of the directional data. Nonetheless, two models are considered for setting limits on the notch's characteristics: 1) an empty notch (model #1: variable width, 100% depth) and 2) a partially-filled notch (model #2: variable width and depth).

## 4.4 Model #1: Empty Notch

### 4.4.1 Omnidirectional Notch Response Function

The simplest anisotropy model assumes a case of negligible scattering and represents the notch as a complete dropout of particles within a range of pitch angles characterized by variable width and 100% depth (see Figure 4.2). These assumptions enable efficient fitting of simulated directional response functions to data using a single "effective width" parameter.

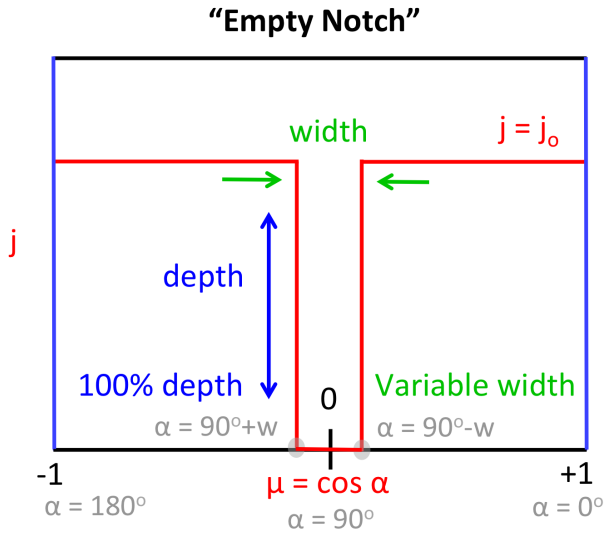


**Figure 4.2**. Diagram of notch model #1.

The implementation of the notch concept is most readily demonstrated through its application to omnidirectional intensities. The general expression

is:

$$\mathrm{J} = 2\pi \int_{-1}^{1} j(\mu)\ d\mu \tag{4.4.1}$$

where $j$ denotes directional particle intensity and $\mu$ is related to pitch angle, $\alpha$, by: $\mu = \cos\alpha$. For an isotropic distribution, $j = j_0$ and is constant, so J $= 4\pi j_0$. For a distribution with a notch, the missing particle intensity ($\mathrm{J}_n$) is given by the integral over the notch's effective width $w$ centered at $\alpha = 90°$:

$$\mathrm{J}_n = 2\pi \int_{\cos(90°+w/2)}^{\cos(90°-w/2)} j(\mu)\ d\mu = 4\pi j_n \cos(90° - w/2). \tag{4.4.2}$$

Assuming negligible scattering within the notch implies that the directional intensity of the missing particles is isotropic: $j_n = j_0$. Thus, a normalized "omnidirectional notch response function" is obtained:

$$\delta_{\mathrm{omni}} = \frac{\mathrm{J}_n}{\mathrm{J}} = \cos(90° - w/2) = \cos\alpha. \tag{4.4.3}$$

### 4.4.2 Directional Notch Response Functions

To implement the directional version of this empty notch model, the Monte Carlo simulation described in Subsection 4.2 is used to calculate the pitch angle distribution of particles passing through HET 1 or HET 2 during a simulated magnetometer roll maneuver (such as that shown in Figure 4.3), taking into account the observed magnetic field direction for a particular epoch. The notch is created by excluding particles having pitch angles within an effective width centered on 90°. Normalizing the simulated values outside of the notch to observed rates and accounting for the spacecraft's 8.6° rotation during the 48 s accumulation interval, a smooth, width-dependent roll maneuver notch response function is generated (e.g. Figure 4.5). Then, a $\chi^2$ value can be determined by comparing to the 48-s data. The process is repeated for different widths to identify the width that produces the minimum $\chi^2$ (see Figure D.1 in Appendix D for a sample $\chi^2$-fit parabola). After determining the best fit to the

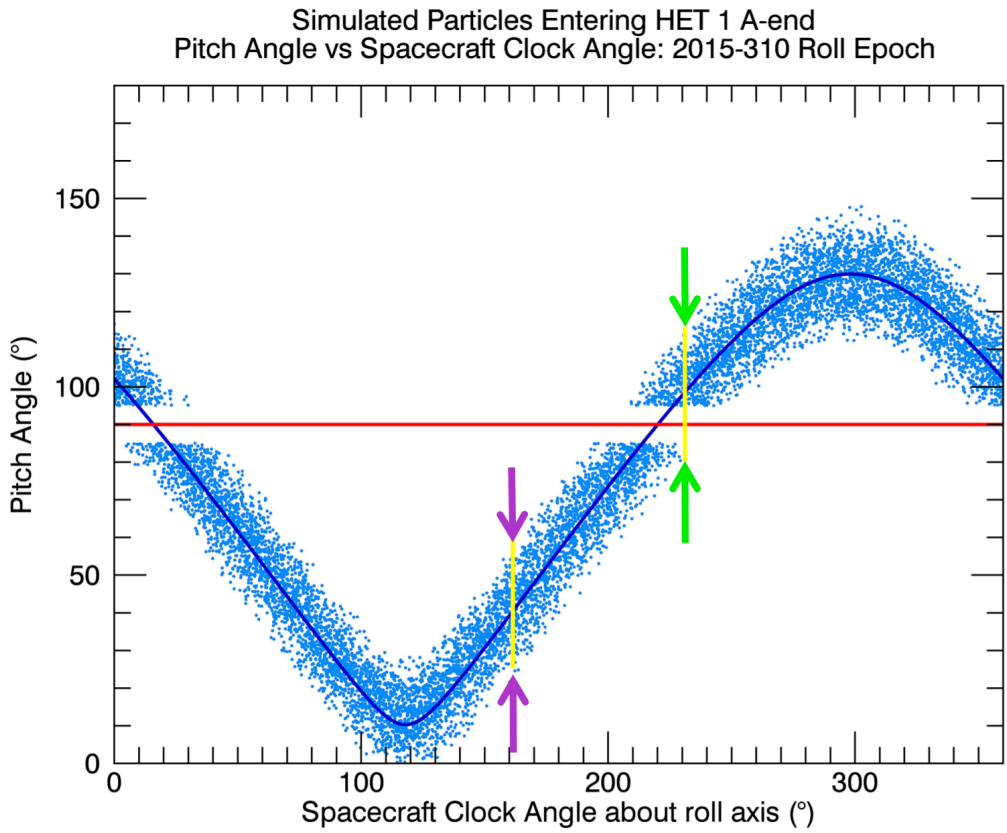


**Figure 4.3**. Pitch angle vs. spacecraft clock angle (measured from $\hat{\mathrm{N}}$ towards $\hat{\mathrm{T}}$) view of the 2015-310 roll maneuver Monte Carlo simulation for particles entering HET 1's A-end, shown with a 10°-wide notch. The magnetic field for this epoch was (0.156, -0.381, 0.202) nT in R, T, N (from the MAG's publicly-available data: https://omniweb.gsfc.nasa.gov/coho/form/voyager1.html). Simulated particles (blue dots) fall within a ∼40°-wide band, as defined by the telescope's opening angle. HET 1's nominal boresight is centered at 160.9° clock angle and 40.5° pitch angle; its normal field of view (indicated by the purple arrows) does not overlap with 90° pitch angle (red horizontal line). However, when the HET 1 boresight passes through ∼17° and ∼219° clock angle during the 2015-310 roll maneuver, the notch is directly centered in its field of view; therefore a measurable count rate reduction is observed (see Figure 4.5a). HET 1's 70°-offset boresight is at 230.9° clock angle and 98.5° pitch angle, so its field of view also overlaps with the anisotropy during the offsets (green arrows).

roll-maneuver data, the resulting notch is incorporated in omnidirectional and 70°-offset response functions to predict expected intensity reductions ($\delta_{\mathrm{omni}}$, $\delta_{70^\circ}$) for each epoch.

Figure 4.5a shows simulated roll maneuver response functions fits to ob-

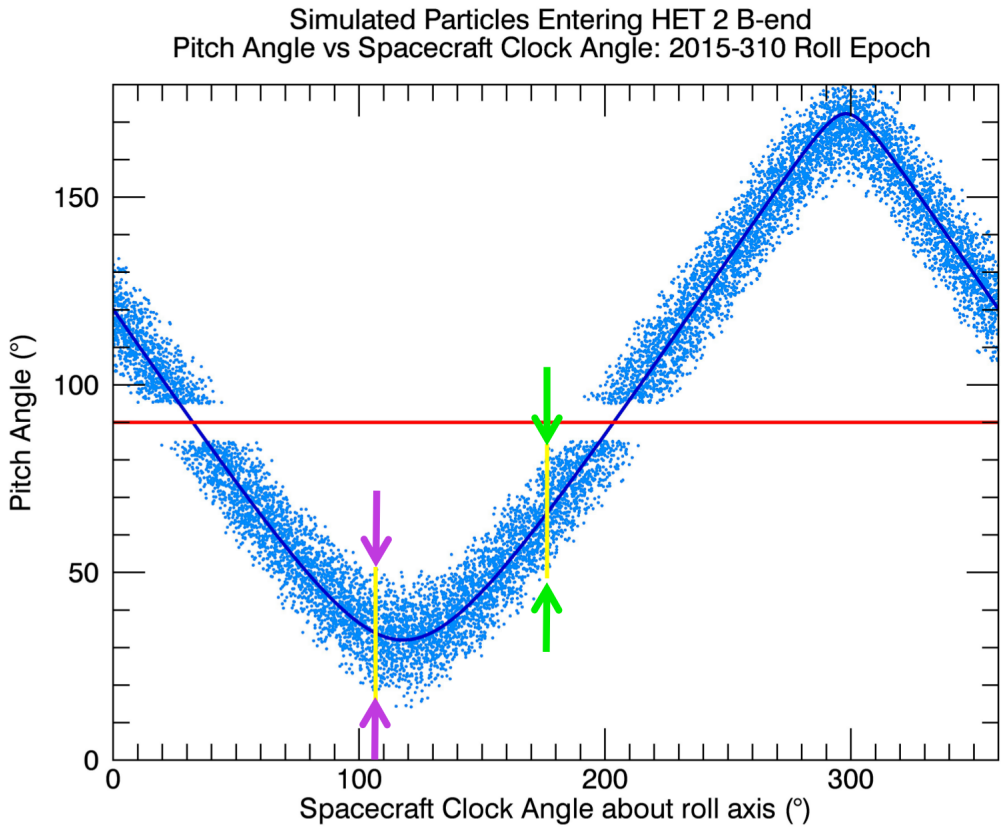


**Figure 4.4**. Similar to Figure 4.3, but for particles entering HET 2's B-end. HET 2's normal field of view (purple arrows) does not overlap with 90° pitch angle (red horizontal line) since its normal boresight is centered at 107.1° clock angle and 33.7° pitch angle. HET 2's 70°-offset boresight for this 2015-310 epoch is at 177.1° clock angle and 66.4° pitch angle, placing HET 2's field of view (green arrows) at the edge of the anisotropy; it may see an intensity decrease if the notch is wide enough.

served bi-directional HET 1 PENH counts for the 2015-310 roll maneuver, and Figure 4.5b shows fits to the same data in pitch angle space. Both pitch angle and clock-angle-space fits yield the same effective widths for all epochs. For 2015-310, the best fit was generated by a notch with an effective width of $4.0° \pm 0.4°$. Since CRS telescopes view the anisotropy as a function of clock angle during the roll maneuvers, it is the clock-angle-space fits that are reported in the following chapters.

Figure 4.6a shows HET 1's observed count rate during 70°-offsets on days

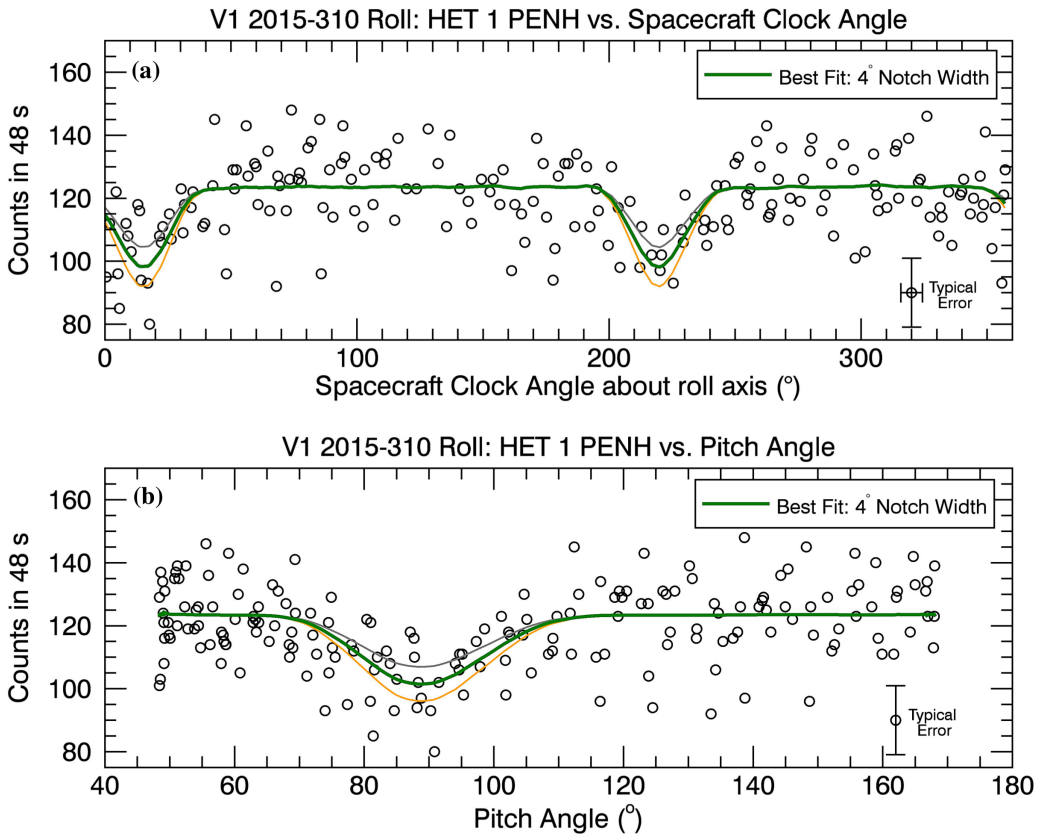


**Figure 4.5**. HET 1's bi-directional PENH rate ($\gtrsim$ 70 MeV; proton-dominated) vs. clock angle (a) and pitch angle (b) during the 2015-310 roll maneuver. The magnetic field for this epoch was (0.156, -0.381, 0.202) nT in R, T, N (from MAG's publicly-available data: https://omniweb.gsfc.nasa.gov/coho/form/voyager1.html). The thick green solid line superimposed over the data represents the best-fitting notch roll response function produced by a Monte Carlo simulation with a width of $4.0° \pm 0.4°$. Independent fits applied in clock angle space and pitch angle space yielded the same best fit geometry. The thinner top (grey) and bottom (gold) lines represent 3° and 5°-wide notches respectively, plotted for visual reference. The horizontal line on the typical error reflects an 8.6° angular averaging within the 48-s data interval produced by the spacecraft as it rolls in clock space, while the vertical line reflects the statistical uncertainty in the number of counts. Count reductions appear broadened in both pitch angle and clock angle space, reflecting the $\sim$40° opening angle of the telescope.

2015-297 through 2015-299, a subset of the full sequence of offset maneuvers which took place nearest to the 2015-310 roll epoch (recall Figure 3.6). As mentioned in Section 3.3, an observed 70°-offset rate reduction is calculated by combining the 48-s data from the full sequence of offsets and normalizing to the

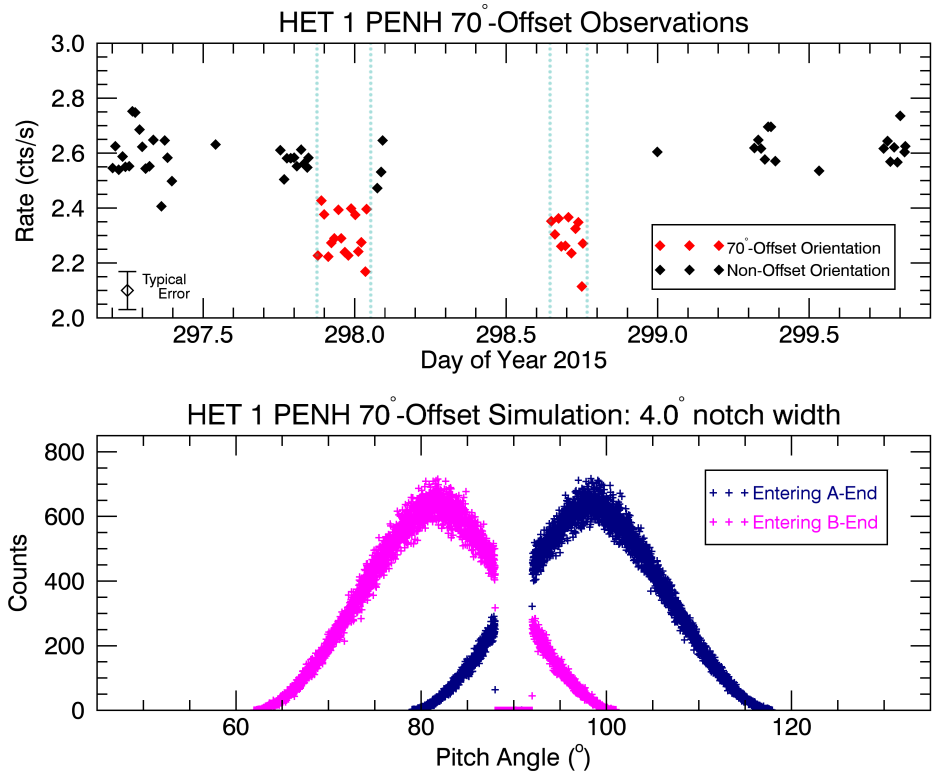


**Figure 4.6**. HET 1's 70°-offset observed intensities (a) and simulation (b) near the time of the 2015-310 roll maneuver.
(a) is an average (typically 480-s intervals) of a subset of data from the offset epoch which began on 2015-296. The full set of maneuvers consisted of 7 offsets that took place between days 296 and 312 (see Figure 3.6), and the observed rate reduction was $11.0\% \pm 0.3\%$ for this series of maneuvers.
(b) shows the 4.0°-wide notch cut applied to the simulation of HET 1's bi-directional 70°-offset response function for particles entering the telescope's A-end (right; navy blue) and B-end (left; pink). The predicted reduction was $12.2\% \pm 1.2\%$.

averages of temporally adjacent non-offset rates. A corresponding 70°-offset rate reduction is predicted from the roll maneuver fit results by summing the counts in HET 1's simulated bi-directional response function (Figure 4.6b) with and without the notch cut. The observed 70°-offset reduction for this particular epoch was $11.0\% \pm 0.3\%$ and the predicted value was $12.2\% \pm 1.2\%$. Figure 4.7 shows the same concept applied to HET 2.

Recalling Section 3.4, an observed omnidirectional count reduction is determined by comparing each epoch's daily average to the average rate ($430.01 \pm 0.06$ cts/s for HET 1) during 2013.6 to 2014.1 – a time period when the pitch

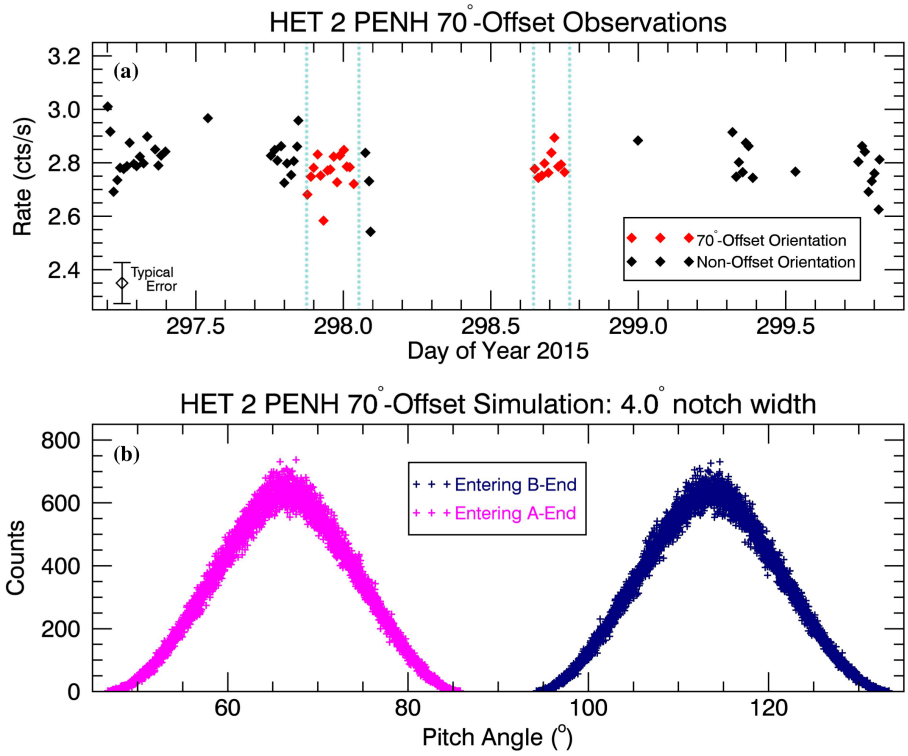


**Figure 4.7**. Similar to 4.6, but for HET 2.
(a) HET 2's observed rate reduction was $1.7\% \pm 0.4\%$ for this series of maneuvers. (b) Due to the orientation of HET 2's boresight, no reduction is predicted when a 4.0°-wide notch cut is applied to its bi-directional 70°-offset response function. Note that HET 1 and HET 2 are oppositely oriented, so particles entering the HET 2's B-end are on the right (navy blue) and while particles entering HET 2's A-end are on the left (pink).

angle anisotropy is absent (note the steady rates at those times in Figures 3.1a & 3.1b). A predicted reduction in the omnidirectional rate is calculated using Equation 4.4.3 (Subsection 4.4.1). Returning to the 2015-310 roll epoch, and incorporating its $4.0° \pm 0.4°$ effective notch width, a reduction of $3.5\% \pm 0.3\%$ is predicted, which is consistent with the observed value of $3.3\% \pm 0.1\%$ (comparable to the rates near ∼2015.8 and ∼2013.85 in Figure 3.1b).

## 4.5 Model #2: Partially-Filled Notch

### 4.5.1 Omnidirectional Notch Response Function

Model #2 and following models utilize a two-parameter representation of the notch by introducing a depth term to allow for the possibility of scattering. In the omnidirectional notch response function, this is achieved by modifying $j_n$ in Equation 4.4.2 to allow for a reduced directional intensity representation of the missing particle distribution ($j_n < j_0$), leading to:

$$\delta_{\text{omni}} = \frac{\mathrm{J}_n}{\mathrm{J}_0} = \frac{j_n}{j_0}\cos(90^\circ - w/2) = d \times \mu. \tag{4.5.1}$$

Hence, the notch is now partially filled and is characterized by an "effective area" of depth, $d = j_n/j_0$, and width $\mu = \cos\alpha$ ranging from $\alpha = 90^\circ + w/2$ to $\alpha = 90^\circ - w/2$, as shown in Figure 4.8.

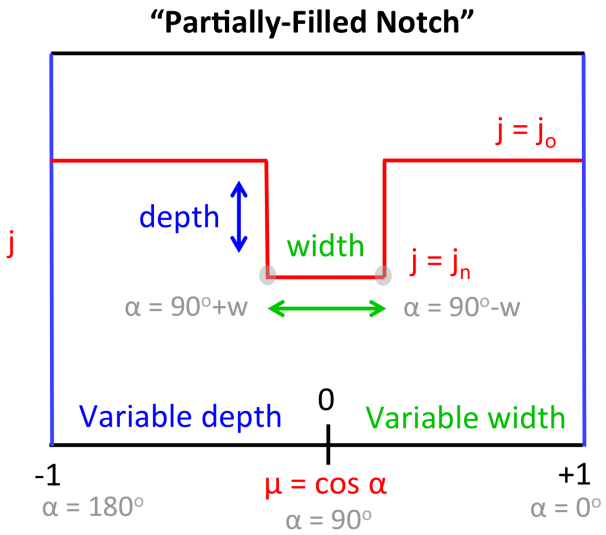


**Figure 4.8**. Diagram of notch model #2.

For a given epoch where the anisotropy is prominent ($\delta_{\text{omni}} > 0$), the range of possible widths is no larger than LECP's full telescope opening angle: $0^\circ \leq w \leq 45^\circ$. Therefore, the range of possible depths is given by:

$$d = \frac{\delta_{\text{omni}}}{\cos(90^\circ - w/2)}. \tag{4.5.2}$$

### 4.5.2 Directional Notch Response Functions

Since the anisotropy is now represented as a single function with two unknowns – width and depth (analogous to Equation 4.5.2) – alternate strategies are employed to implement and evaluate the effectiveness of model #2's simulations. Unlike model #1, which uses independent roll maneuver fits to predict omnidirectional and 70°-offset intensity reductions for each telescope, model #2 requires at least two response functions to constrain the notch's geometry and achieve predictions for comparison amongst $\delta_{\text{omni}}$, $\delta_{70^\circ}$, and roll maneuver observations.

One approach is to compare the same type of response function between the two different telescopes, relying on the assumption that both telescopes report the same notch geometry. Although HET 1 and HET 2's commonalities greatly simplify evaluations, establishing possible limits for the notch's widths and depths requires the response function curves to not be entirely identical. As such, using the directionally sensitive 70°-offset data is the most promising way to achieve any possible constraint.

A second approach is to compare two different response functions for the same telescope, with the advantage that each telescope can be treated independently. The assumption here is that omnidirectional and directional rates are responding to the same notch geometry. Like the first approach, the response function curves should differ enough to set at least some limits on the notch's widths and depths, a feat most likely accomplished by comparing omnidirectional and 70°-offset simulations.

Due to the time-varying nature of the anisotropy and a weak intensity reduction observed by HET 2 during its 70°-offsets, the analysis for model #2 focuses on the 6 offset epochs where the anisotropy is most prominent, listed in Table 4.1. The telescope orientations, omnidirectional intensity reductions

| Offset Epoch | 2013-67 | 2013-120 | 2015-208 | 2015-250 | 2015-296 | 2016-31 |
|---|---|---|---|---|---|---|
| Maneuver Days | 67, 68, 69, 70, 71 | 120, 121 122 | 208, 209, 210, 215, 216 | 250, 251 252 | 296, 297, 298, 300, 301, 302, 303, 307, 308, 312 | 31, 32, 34, 38, 39, 40 |
| HET 1 Offset Boresight (A-end) | r = -0.494<br>t = -0.675<br>n = -0.548 | -0.495<br>-0.673<br>-0.550 | -0.503<br>-0.669<br>-0.547 | -0.506<br>-0.669<br>-0.545 | -0.505<br>-0.671<br>-0.543 | -0.496<br>-0.678<br>-0.543 |
| HET 1 Boresight Pitch Angle | $\alpha = 78.5°$ | 79.3° | 77.2° | 76.7° | 81.3° | 78.3° |
| HET 2 Offset Offset (B-end) | r = -0.209<br>t = -0.056<br>n = 0.976 | -0.212<br>-0.056<br>0.976 | -0.210<br>-0.051<br>0.976 | -0.207<br>-0.051<br>0.977 | -0.204<br>-0.050<br>0.978 | -0.206<br>-0.050<br>0.977 |
| HET 2 Boresight Pitch Angle | $\alpha = 69.2°$ | 70.0° | 66.1° | 67.1° | 66.2° | 67.2° |
| 70°-Offset Reduction ($\delta_{70°}$) | HET 1 = 4.3% ± 0.4%<br>HET 2 = 1.3% ± 0.4% | 6.1% ± 0.4%<br>1.6% ± 0.4% | 7.1% ± 0.4%<br>1.0% ± 0.4% | 7.2% ± 0.6%<br>1.5% ± 0.6% | 11.0% ± 0.3%<br>1.7% ± 0.4% | 11.4% ± 0.4%<br>1.0% ± 0.4% |
| Omnidirectional Reduction ($\delta_{omni}$) | HET 1 = 1.6% ± 0.05%<br>HET 2 = 1.8% ± 0.05% | 2.4% ± 0.05%<br>2.7% ± 0.05% | 1.9% ± 0.05%<br>2.1% ± 0.05% | 2.2% ± 0.07%<br>2.4% ± 0.07% | 2.9% ± 0.04%<br>3.1% ± 0.05% | 3.1% ± 0.06%<br>3.3% ± 0.06% |
| B-field | r = 0.175<br>t = -0.444<br>n = 0.200<br>\|B\| =0.517 | 0.178<br>-0.421<br>0.188<br>0.495 | 0.118<br>-0.402<br>0.197<br>0.463 | 0.117<br>-0.392<br>0.183<br>0.448 | 0.152<br>-0.379<br>0.200<br>0.455 | 0.132<br>-0.370<br>0.180<br>0.433 |

**Table 4.1**. Summary of HET 1 and HET 2 observational values used for 70°-offset and omnidirectional simulations.

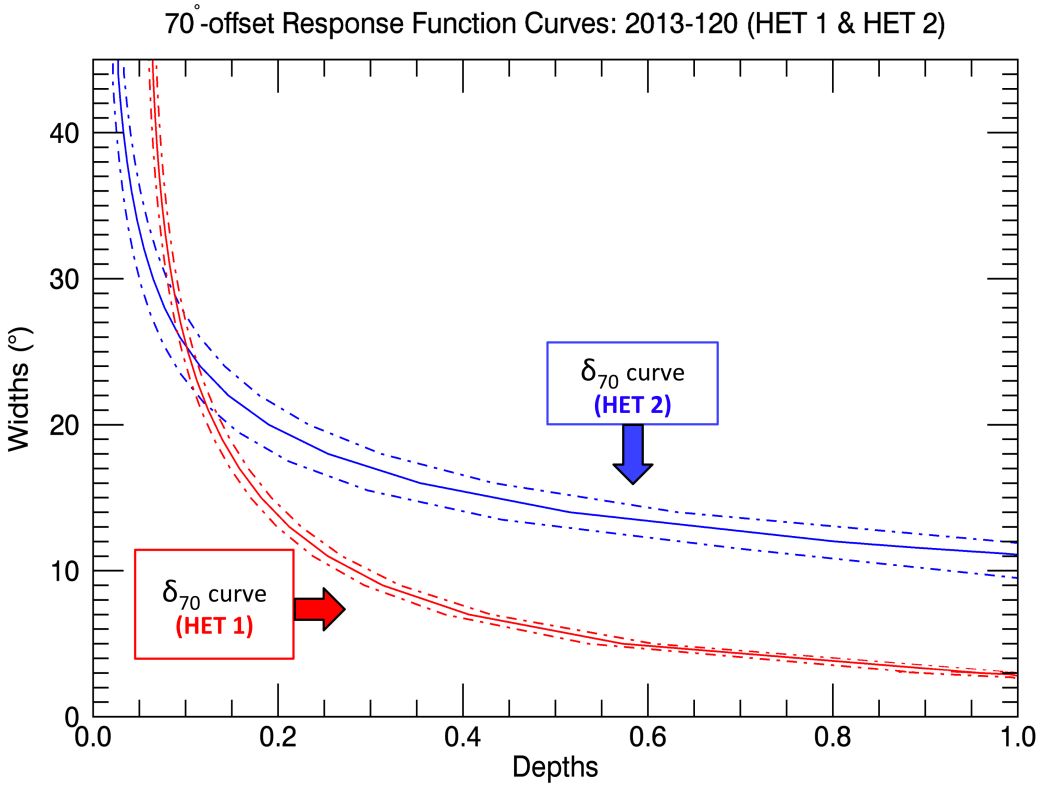


**Figure 4.9**. Simulated HET 1 (red) and HET 2 (blue) 70°-offset widths vs. depths for the 2013-120 offset epoch, allowing for a partially-filled notch. HET 1's A-end boresight pitch angle is centered at 79.3°, while HET 2's B-end is at 70.0° during this maneuver. The dotted curves represent the uncertainties in each telescope's observed relative intensity reductions, $\delta_{70°}$ (see Table 4.1).

($\delta_{\text{omni}}$), 70°-offset reductions ($\delta_{70^\circ}$), and magnetic field observations all reflect the average taken over the offset maneuver sequence time periods.

For some width ($0^\circ \leq w_\alpha \leq 45^\circ$), one can use the Monte Carlo simulation of the telescope's 70°-offset response function (Section 4.2) to determine a depth that produces results consistent with the observed relative intensity reduction, $\delta_{70^\circ}$ (analogous to solving Equation 4.5.2 using the observed $\delta_{\text{omni}}$). An isocontour curve is generated by stepping through a variety of widths and depths. Roll maneuver fits are still obtained through $\chi^2$ minimization, but are slightly modified to allow for both variable width and depth.

Figure 4.9 shows the superposition of HET 1 (red) and HET 2 (blue) 70°-offset response function curves for the 2013-120 epoch. The intersection occurs at 25.8° width and 10.0% depth, with widths ranging from 22.8° to 28.1° and depths from 10.8% to 9.7%. Incorporating these results into Equation 4.5.1 yields a predicted $\delta_{\text{omni}}$ of $2.2 \pm 0.1\%$ compared to the observed 2.4% for HET 1 and 2.7% for HET 2.

Figure 4.10 and Figure 4.11 show superimposed omnidirectional and 70°-offset curves for the same offset epoch. While HET 1's observations allow for a broad range of widths and depths – 2.8° to >45° and 100% to < 6.5% (Figure 4.10) – HET 2's observations narrow the range of possible values to widths of 19.2° to 25.8° and respective depths of 16.4% down to 11.8% along the curve (Figure 4.11). The 2013-120 nominal values are 22.5° wide and 13.7% deep.

Best fits to roll maneuver data give independent measurements of the geometries; for example, the 120-122 roll maneuver epoch is characterized by a nominal width of 25.8° (ranging from 23.2° to 33.4°) and depth of 18.5% (ranging from 21.5% to 15.5%) for HET 1. For HET 2, the nominal width and depth is 24.6° and 18.0% (ranging from 20.3° to 29.2° and 21.0% to 15.0%,

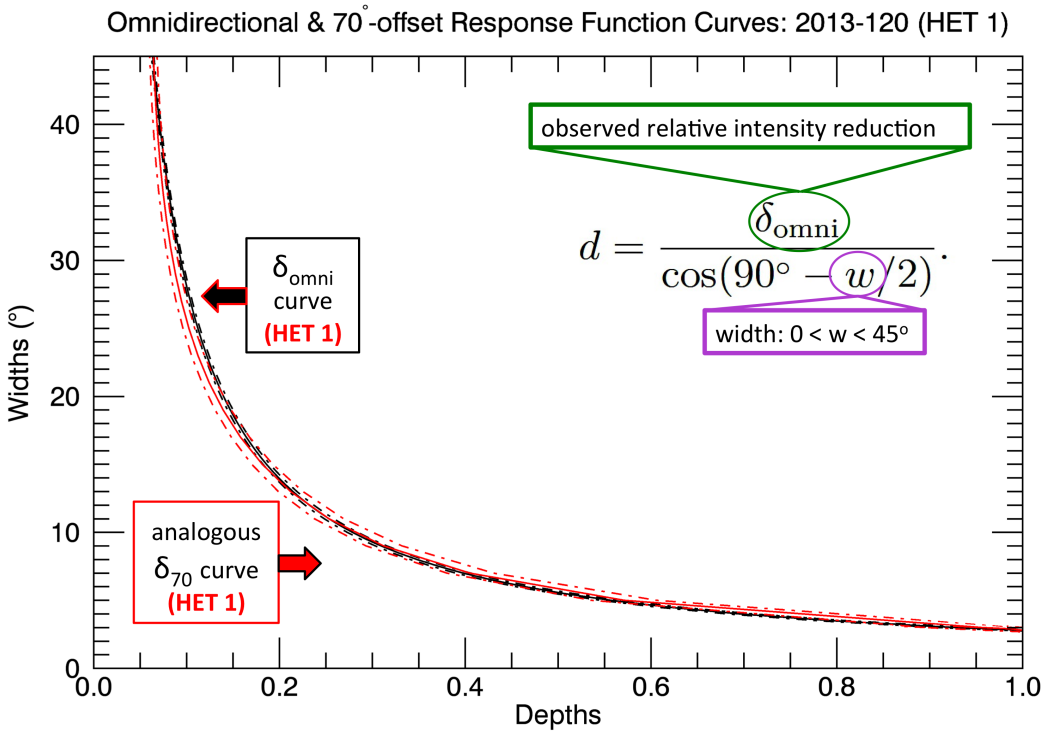


**Figure 4.10**. Simulated omnidirectional (black, dotted) and 70°-offset (solid, red) widths vs. depths for HET 1 during the 2013-120 offset epoch.

respectively).

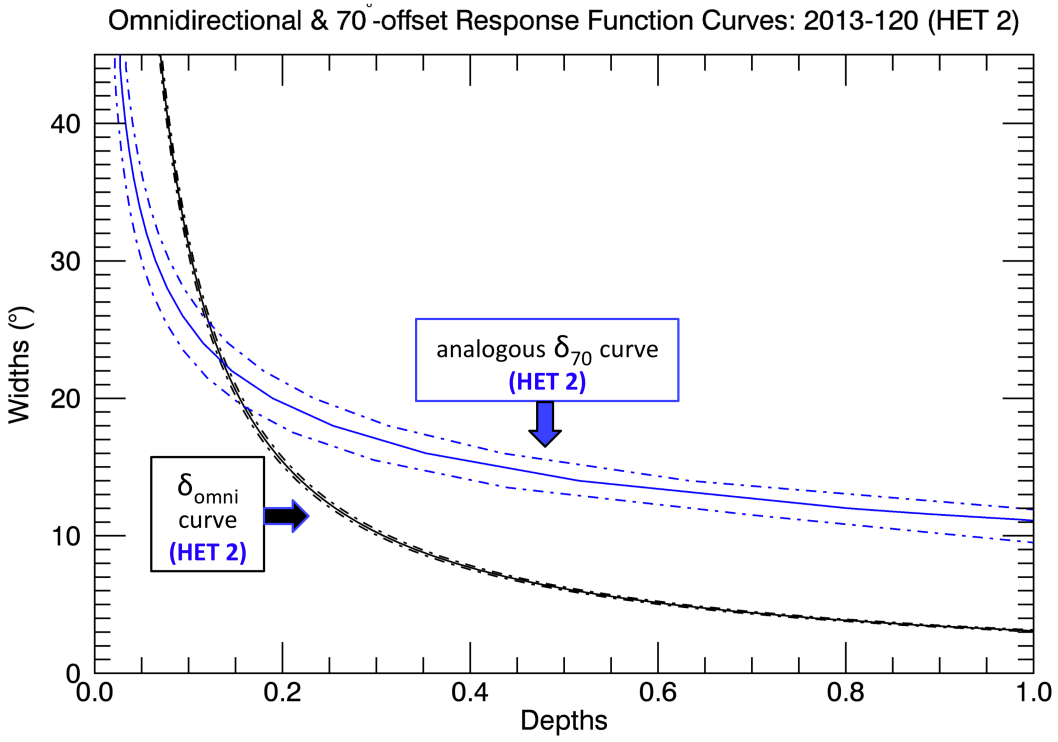


**Figure 4.11**. HET 2 version of Figure 4.10.

# Chapter 5
# Results

## 5.1 Model #1: Predictions and Comparison with Observations

Results from best fits of notch model #1 (empty notch with varying width and 100% depth) to HET 1's bi-directional PENH roll rate for 25 epochs are shown in Figure 5.1 and listed in Appendix D, Table D.1; these epochs occur from late 2012 (shortly after the heliopause crossing) through the end of 2016, when the number of rolls per maneuver was reduced. The effective widths range from 0° to ∼4° (Figure 5.1b). Overall, HET 1 bi-directional 70°-offset predictions (Figure 5.1c) and omnidirectional predictions (Figure 5.1d) agree well with respective observations.

Similar results derived from the best fits to HET 2's roll-maneuvers are shown in Figure 5.2 and listed in Appendix D (Table D.2). HET 2's widths also vary from 0° to ∼4° (Figure 5.2b) and predictions from its omnidirectional notch response function agree with observations (Figure 5.2d). However, the 70°-offset results are not consistent (Figure 5.2c); simulations predict that HET 2 should not observe a decrease, but small, statistically-significant intensity changes are observed. This disagreement illustrates a shortcoming of the empty notch model.

Figure 5.3 shows the average of HET 1 & HET 2 effective widths, weighted by uncertainties. An important implication from this model is that the temporal nature of these durable anisotropy episodes is due to smoothly varying changes

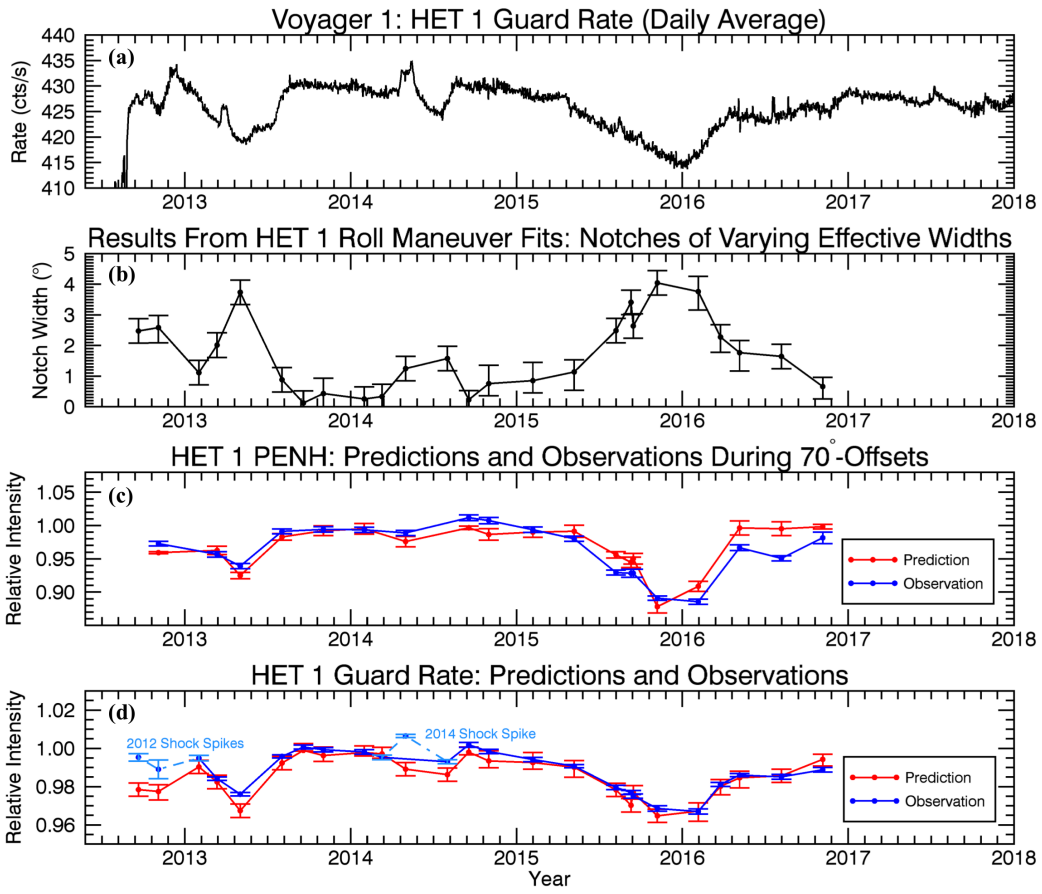


**Figure 5.1**. (a) HET 1's omnidirectional guard rate ($\gtrsim$ 20 MeV; proton-dominated) shows the time-varying GCR intensity reductions caused by the pitch-angle anisotropy.
(b) Effective notch widths from fits to HET 1's bi-directional PENH rate ($\gtrsim$ 70 MeV; proton-dominated) during the 25 roll maneuvers from late 2012 through 2016. Monte Carlo simulations incorporating these widths were used to determine the predicted intensities shown in panels (c) and (d).
(c) 70°-offset predictions and observations near the 25 roll epochs for HET 1's bi-directional PENH rate ($\gtrsim$ 70 MeV; proton-dominated). Observed intensities are normalized to temporally-adjacent non-offset rates, while predicted intensities are normalized to simulated response function values without a notch.
(d) Omnidirectional predictions and observations during the 25 roll epochs for HET 1's guard rate ($\gtrsim$ 20 MeV; proton-dominated). Observed intensities are normalized to the average values during the 2013.6 to 2014.1 time period when count rates are relatively uniform and isotropic, while predicted intensities are normalized to simulated response function values without a notch.

to the notch's width. GCR intensity decreases are attributed to the notch slowly widening from 0° until it reaches some maximum effective width over the

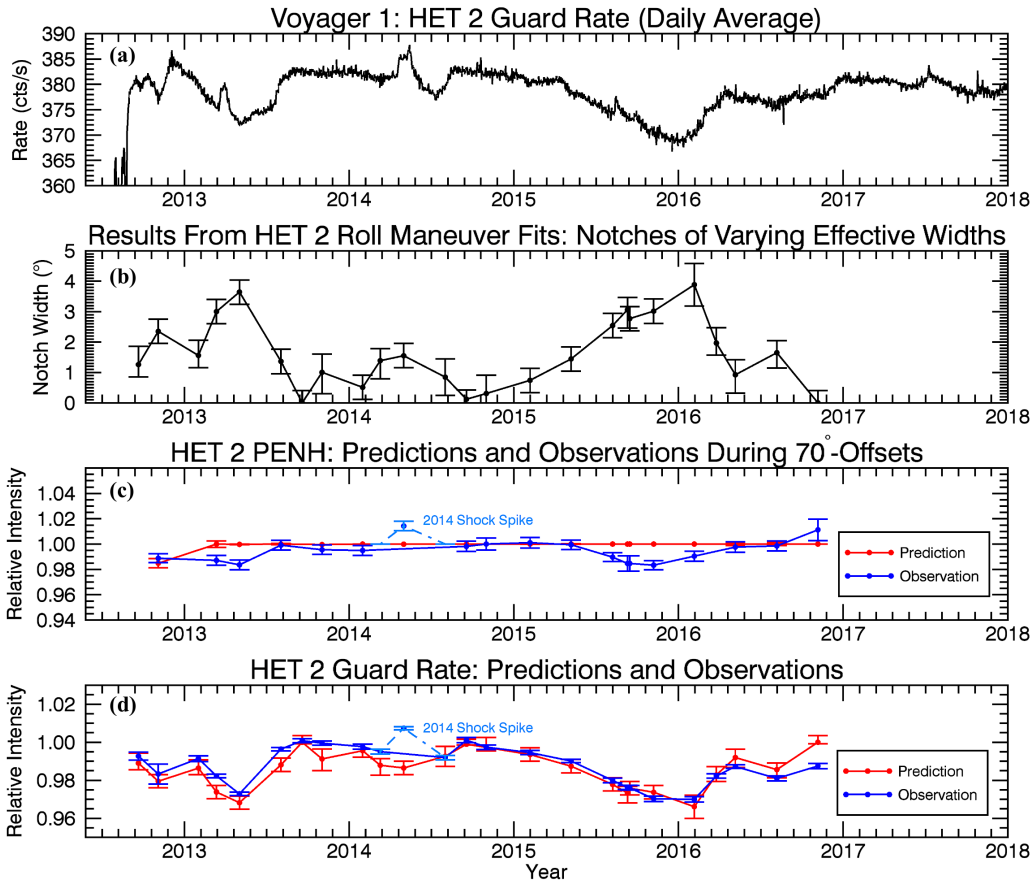


**Figure 5.2**. Same as Figure 5.1, but for HET 2. (a) HET 2's omnidirectional guard rate ($\gtrsim$ 20 MeV; proton-dominated).
(b) Effective notch widths from fits to HET 2's bi-directional PENH rate ($\gtrsim$ 70 MeV; proton-dominated) during the 25 roll maneuvers from late 2012 through 2016.
(c) 70°-offset predictions and observations near the 25 roll epochs for HET 2's bi-directional PENH rate ($\gtrsim$ 70 MeV; proton-dominated).
(d) Omnidirectional predictions and observations during the 25 roll epochs for HET 2's guard rate ($\gtrsim$ 20 MeV; proton-dominated).

course of ∼60 to ∼260 days. Subsequently, intensity recoveries are attributed to the notch smoothly narrowing over ∼40 to ∼370 days, until it disappears, returning the particle distribution to isotropy.

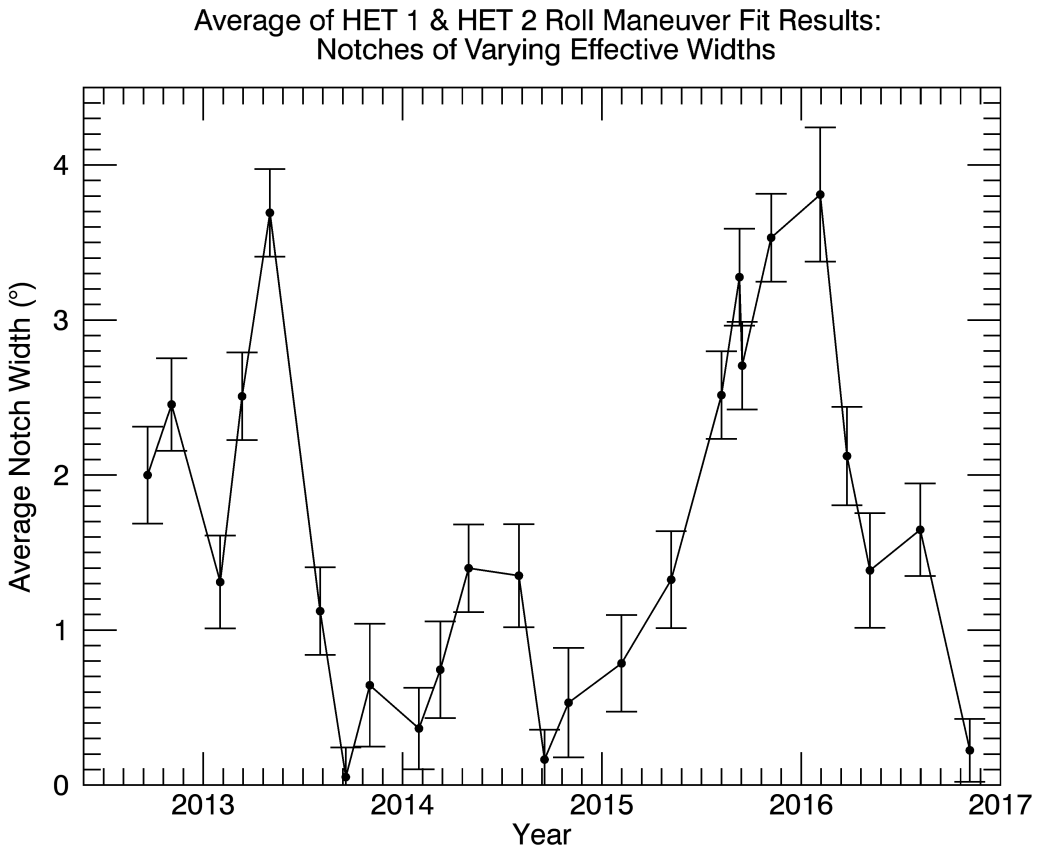


**Figure 5.3**. A comparison of average effective widths (weighted by uncertainties) obtained from best fits of the notch model applied independently to HET 1 & HET 2 bi-directional PENH rates ($\gtrsim$ 70 MeV; proton-dominated) during roll maneuvers. Results are listed in Appendix D, Table D.2 (last column).

## 5.2 Advantages & Limitations of Model #1

There are several attractive features of the empty notch model. First, it is straightforward to implement; a single width parameter fitted to roll maneuver data yields predictions for omnidirectional and 70°-offset rates that reasonably agree with HET 1's observations. Second, the resulting geometry is validated by two telescopes; independent fits to HET 1 and HET 2 roll maneuvers report similar notch widths. Third, it is not limited to spacecraft maneuvers; one can determine how the notch evolves by directly using the omnidirectional response function (Equation 4.4.3). For example, HET 1's omnidirectional rate

for the largest anisotropy episode reached a maximum intensity reduction of $3.8\% \pm 0.2\%$ on day 11 of 2016, corresponding to an effective notch width of $4.3° \pm 0.2°$ – the maximum width of the most prominent anisotropy to date. Since the 70°-offsets were discontinued in 2017 and roll maneuvers are now limited, omnidirectional measurements will be important for characterizing future anisotropy episodes, along with LECP's continued observations.

Nonetheless, the inconsistency between HET 2's 70° offset predictions and observations illustrates that there may be factors to consider that are beyond the scope of the model. Resolving the discrepancy requires a shift in boresight pitch angle of typically ∼8°, which theoretically might be achieved if there are errors in either the telescope's assumed pointing direction or the measured magnetic field direction. However, the adjustment required is too large to be attributed to uncertainty in telescope orientation and is also beyond the range of MAG's uncertainties. An added complication is that changing the magnetic field direction also affects the results for HET 1.

In principle, consistency between measurements and calculations for the HET 2 70°-offset decrease can be achieved by simply allowing for a wider notch. However, maintaining the 100% depth assumption leads to significant inconsistencies for HET 1. Using the 2015-296 offset epoch (2015-310 roll epoch) as an example, HET 2's observations ($1.7\% \pm 0.4\%$) can be reproduced by an effective notch width of $19.1° \pm 0.8°$. Yet, this same width applied to HET 1 predicts a $56.2\% \pm 2.2\%$ relative intensity reduction compared its $11.0\% \pm 0.3\%$ observation. Model #2's broader, partially-filled notch resolves these issues by introducing a variable depth parameter (see, e.g. Table E.1 in Appendix E).

## 5.3 Model #2 Results

### 5.3.1 70°-offset Approach: Predictions and Comparison with Observations

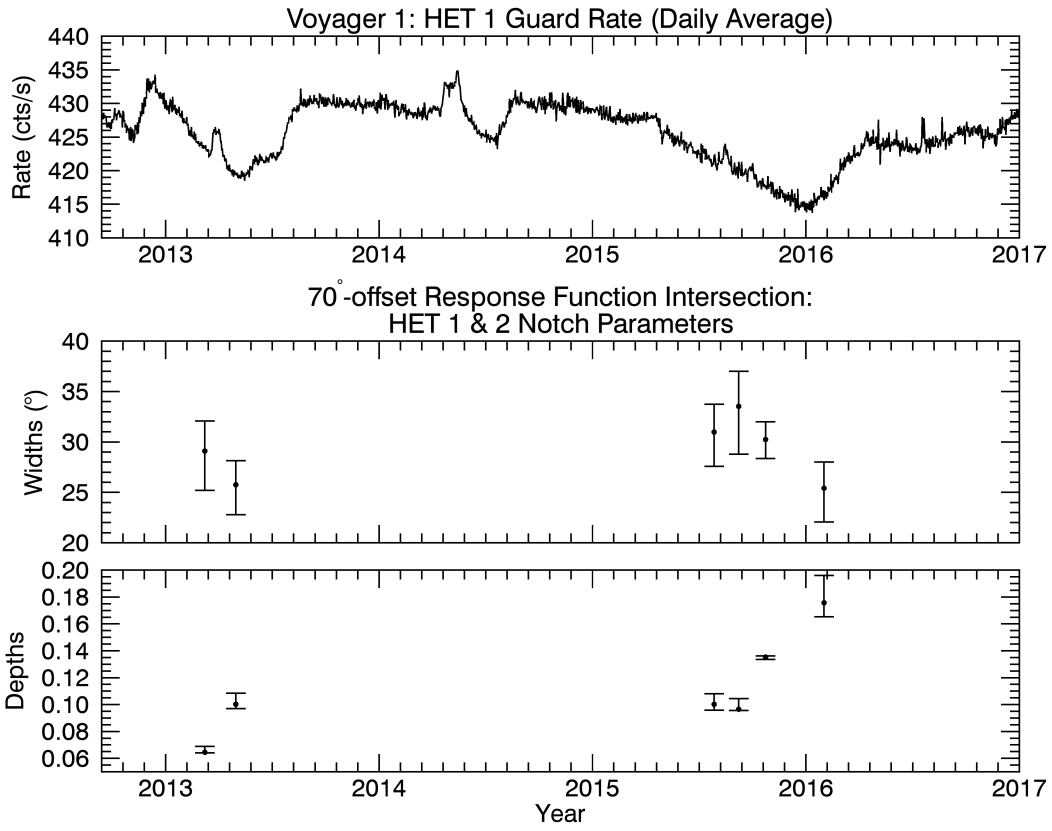


**Figure 5.4**. Anisotropy characteristics determined by finding the intersection of HET 1 and HET 2's 70°-offset notch response curves for the 6 epochs listed in Appendix E, Table E.2.

Figure 5.4 shows widths and depths obtained by solving for the intersection between HET 1 and HET 2's 70°-offset notch response function curves; the results are also listed in Appendix E, Table E.2. The response function curves for each epoch were generated using the values in Table 4.1, and intersection points were determined for the 6 most prominent 70°-offset epochs (due to statistical limitations), via the process described in Chapter 4, Subsection 4.5.2.

The average width is ∼29° and is narrowest near the minimum of the 2015 anisotropy episode (∼25° during the 2016-31 epoch), while the average depths are largest near the minima of the 2013 and 2015 anisotropy episodes: 1) ∼7% in 2013-67 and 2) ∼18% (2016-31).

Figure 5.5 shows the predicted omnidirectional intensity reductions from applying the resulting notch parameters to Equation 4.5.1. Compared to HET 1 and HET 2 observations (red, blue), the predictions (black) agree for the 2013-67 epoch, are a few sigma low for the 2013-120 epoch, and several sigma high from 2015 onward, implying an unphysical scenario – that omnidirectional observations are produced by a different-sized notch than that required for the 70° offsets.

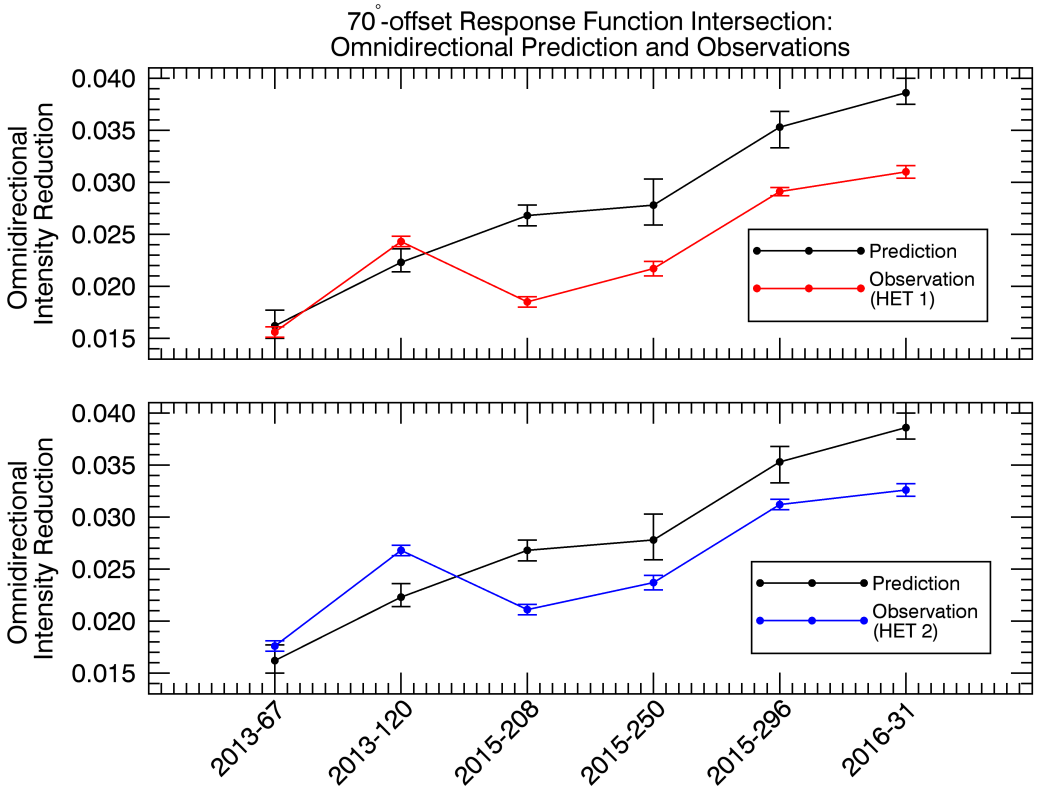


**Figure 5.5**. Predicted and observed omnidirectional intensity reductions achieved by applying HET 1 & HET 2's 70°-offset fit parameters (shown in Figure 5.4) to Equation 4.5.1.

These conflicting sets of measurements invoke consideration of two possible causes. First, the omnidirectional observations could theoretically encompass an additional flux that is outside of HET 1 and HET 2's 70°-offset fields of view. Such an enhancement would make the observed relative intensity change appear smaller than that caused by the pitch angle anisotropy alone. However, observations show that the intensity outside of the notch region remains uniform and constant over all epochs (recall Section 3.5), with the exception of a few shock transients that last ∼30 days at most. Notably, these transients cause decreases in the reported omnidirectional intensities for some of the epochs shown in Model #1 (Figures 5.1d and 5.2d), but they can be clearly identified as "spikes" in both the omnidirectional and directional data, and the epochs concerned are not included in Model #2's analysis. Also, a single shock transient cannot account for the multiple-epoch trend that endures for ∼200 days (from 2015-208 onward).

A second possibility is motivated by a key difference between omnidirectional and directional observations: the sensitivity (or lack thereof) to the telescope's boresight pitch angle, $\alpha$. The 70°-offset data is particularly sensitive to the anisotropy's location due to its dependence on the combination of both telescope and magnetic field direction. A small adjustment to the magnetic field direction that is consistent with MAG's uncertainties can resolve the omnidirectional and 70°-offset disparity, as demonstrated in the following sections.

### 5.3.2 Illustrative Magnetic Field Adjustments

To illustrate each telescope's differing sensitivities, HET 1's width vs. depth curves for boresight pitch angles ranging from $\alpha = 70°$ to 85° are presented for the 2013-120 offset epoch in Figure 5.6. Similar curves are also shown for HET 2, in this case for boresight pitch angles ranging from $\alpha = 60°$ to 75° (Figure 5.7). Notably, all of HET 2's simulated 70°-offset curves (solid

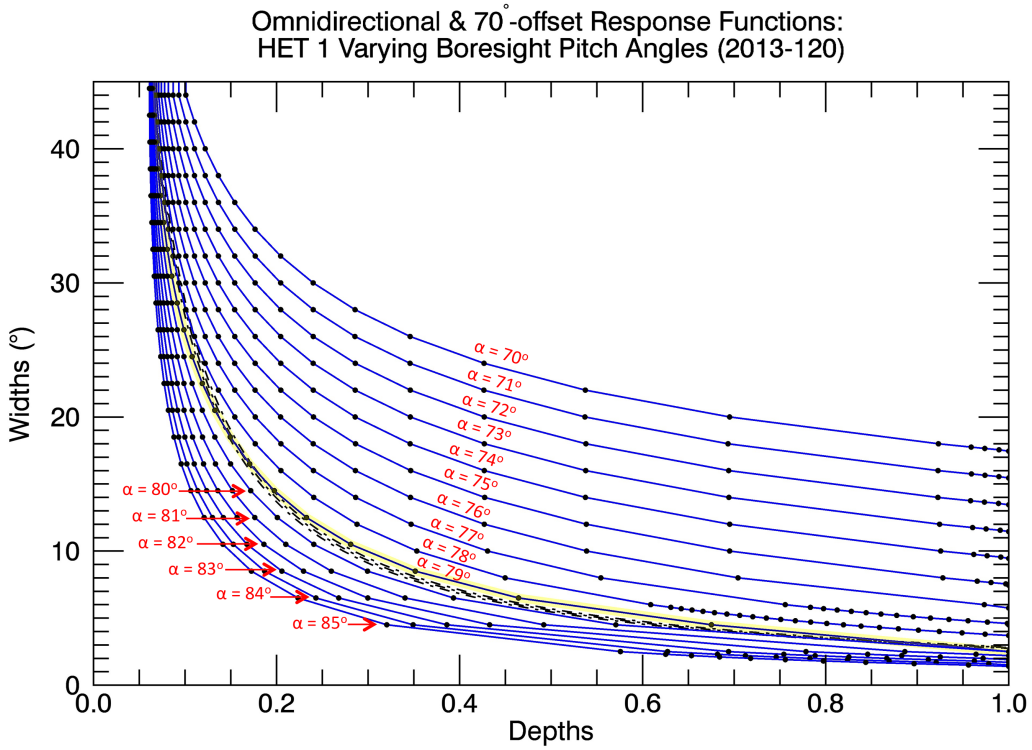


**Figure 5.6**. Width and depth curves for simulated HET 1 (PENH; $\gtrsim$ 70 MeV, proton-dominated) 70°-offset (blue, solid) and omnidirectional (black, dotted) notch response functions for pitch angles ranging from $\alpha = 70°$ to 85°. These pitch angles reflect the angle between the telescope's B-end boresight with respect to the magnetic field. The 70°-offset curves were each calculated from observations listed in Table 4.1 (uncertainties not shown). HET 1's boresight pitch angle during the 70°-offset intervals within the 2013-120 epoch was $\alpha = 79.3°$ (yellow).

blue) intersect with the omnidirectional curves (dashed black) at some point, revealing a variety of possible solutions, depending on the particular value of $\alpha$. However, the majority of HET 1's curves do not intersect; the few which do represent a narrow range of pitch angles, with curves overlapping so well that the range of possible widths and depths is not effectively constrained by HET 1 alone.

Referring back to the 2013-120 70°-offset example from Chapter 4 (Subsection 4.5.2), differences in HET 1 & 2's boresight orientations enable HET 2 to better set limits to the notch's parameters than HET 1 (e.g. Figures 4.10

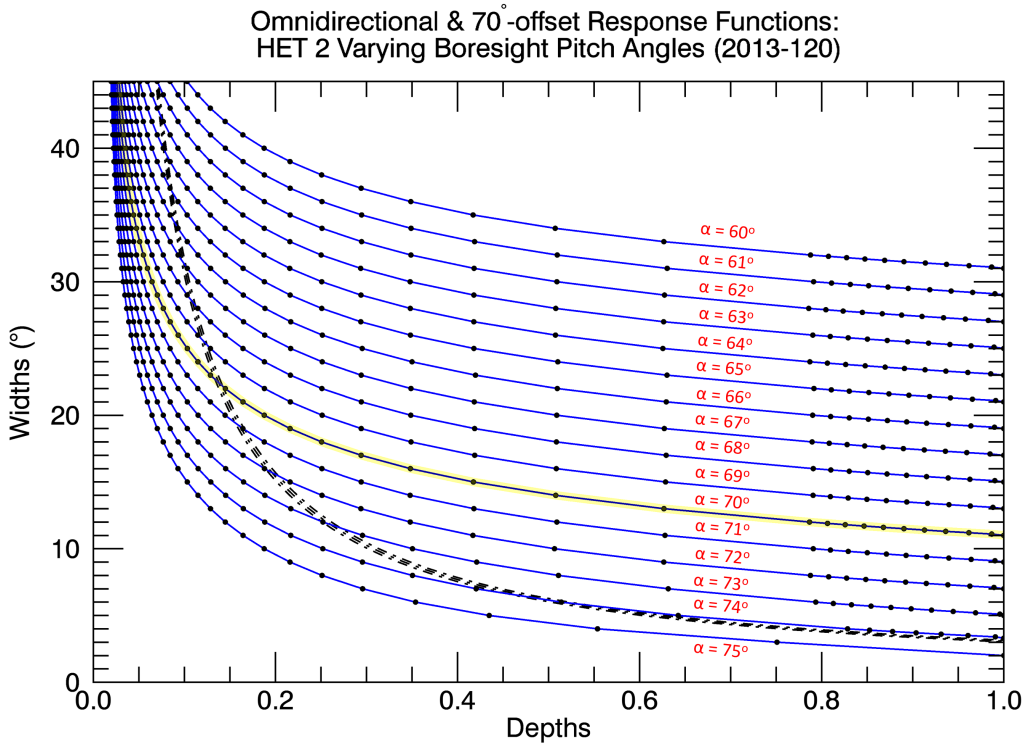


**Figure 5.7**. Width and depth curves for simulated HET 2 (PENH; $\gtrsim$ 70 MeV, proton-dominated) 70°-offset (blue, solid) and omnidirectional (black, dotted) notch response functions, for pitch angles ranging from $\alpha = 60°$ to 75°. The pitch angles shown are with respect to HET 2's A-end boresight; its nominal 70°-offset boresight pitch angle within the 2013-120 epoch was $\alpha = 70.0°$ (yellow).

& 4.11). Indeed, this is true for all epochs. HET 2 is most sensitive to the notch's width and depth since the anisotropy is at the very edge of its field of view. In contrast, the anisotropy is more fully within HET 1's field of view, so it is much more sensitive to the magnetic field direction than HET 2.

A complication arises because the combination of the telescope's boresight direction and the observed magnetic field direction for most epochs does not allow HET 1's omnidirectional and 70°-offset notch response function curves to agree. In fact, the 2013-120 is the only epoch where omnidirectional and 70°-offset simulations intersect without adjustment (albeit, only a small adjustment is needed for 2013-67). For example, Figure 5.8 shows HET 1's curves for

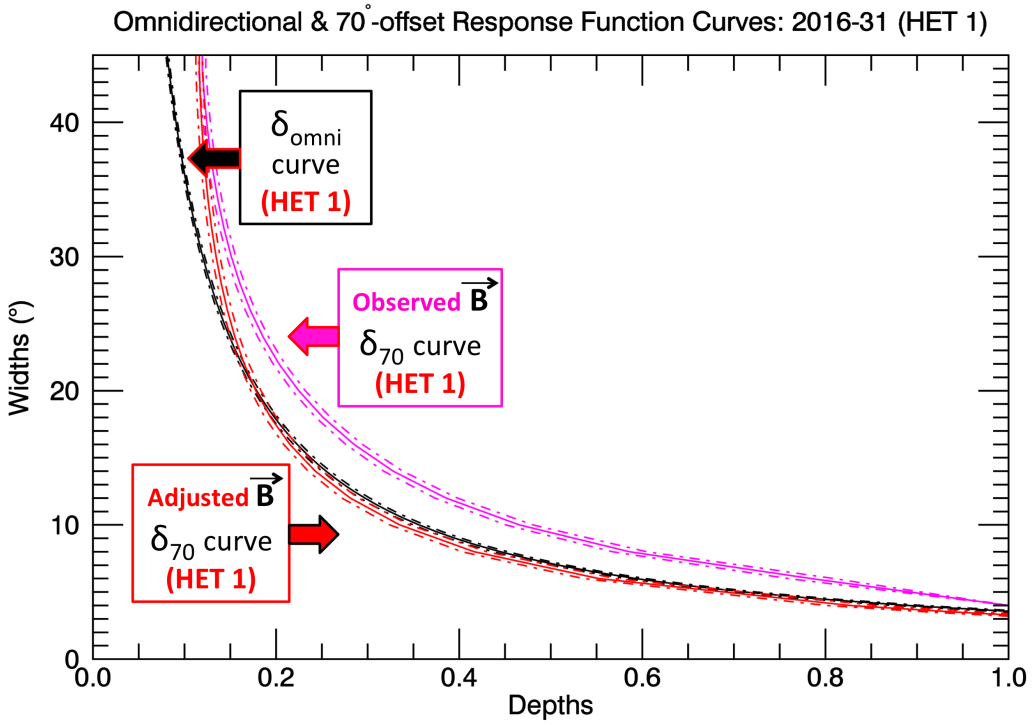


**Figure 5.8**. Simulated HET 1 omnidirectional (black, dotted) and two 70°-offset response function curves indicating the difference between the observed B-field (pink) of (0.132, -0.370, 0.180) nT (in R, T, N) and an adjusted B-field (red) of (0.181, -0.351, 0.170) nT during the 2016-31 offset epoch. HET 1's B-end 70°-offset boresight pitch angle was 79.3° for the observed case and 82.5° for the adjusted case.

2016-31. For this epoch there is no strong agreement between the two curves to within their respective uncertainties that also yields a width and depth that is consistent with HET 2 observations.

Ultimately, the typical shift in boresight pitch angle required to resolve HET 1's disagreement ($\sim$3.5° in $\alpha$), is larger than CRS's expected telescope alignment uncertainties ($\lesssim 1°$). However, uncertainties in the MAG data allow for adjusted directions that are sufficient. Thus, an additional search is done for an alternate B-field direction that is illustrative in achieving agreement amongst HET 1 & 2 omnidirectional and directional observations for each epoch.

### 5.3.3 Magnetic Field Results

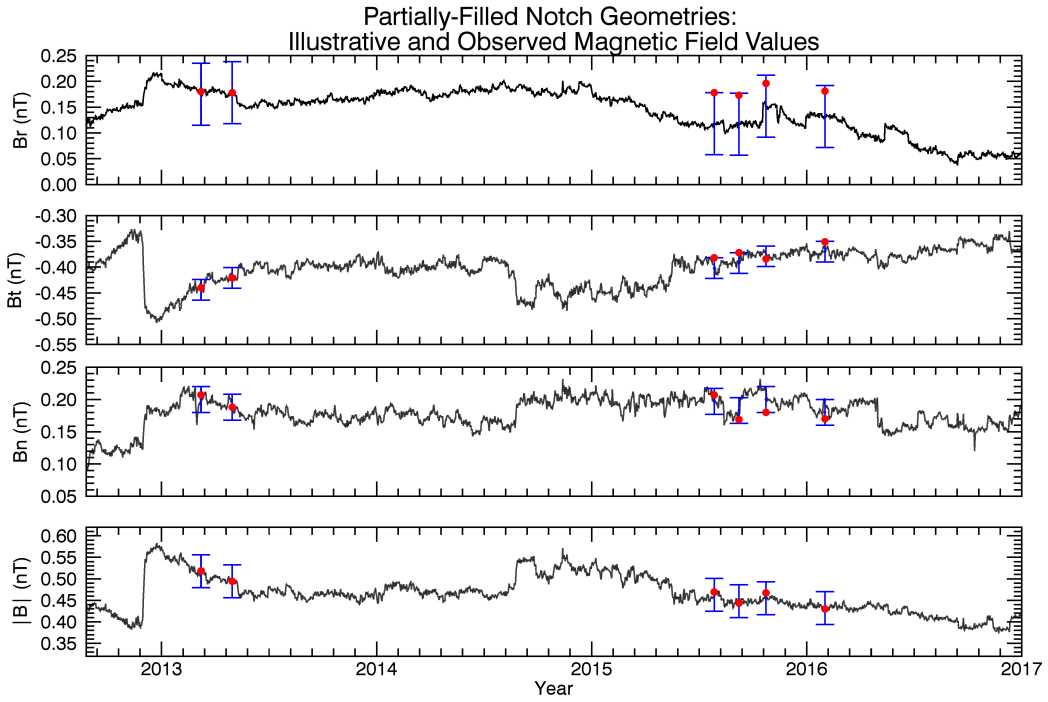


**Figure 5.9**. Comparison of observed (black) and illustrative (red dots) magnetic fields used for the variable width, variable depth notch analysis. The error bars (blue) reflect MAG's 1-$\sigma$ uncertainties: $\delta$B = ($\pm$0.06, $\pm$0.02, $\pm$0.02) nT in R, T, N.

| | | **2013-67** | **2013-120** | **2015-208** | **2015-250** | **2015-296** | **2016-31** |
|---|---|---|---|---|---|---|---|
| **Illustrative** | Br = | 0.180 | 0.178 | 0.178 | 0.173 | 0.196 | 0.181 |
| **Magnetic** | Bt = | -0.440 | -0.421 | -0.382 | -0.372 | -0.384 | -0.351 |
| **Field** (nT) | Bn = | 0.207 | 0.188 | 0.207 | 0.169 | 0.180 | 0.170 |
| | \|B\| = | 0.519 | 0.494 | 0.470 | 0.444 | 0.467 | 0.430 |
| **Observed** | Br = | 0.175 | 0.178 | 0.118 | 0.117 | 0.152 | 0.132 |
| **Magnetic** | Bt = | -0.444 | -0.421 | -0.402 | -0.392 | -0.379 | -0.370 |
| **Field** (nT) | Bn = | 0.200 | 0.188 | 0.197 | 0.183 | 0.200 | 0.180 |
| | \|B\| = | 0.517 | 0.495 | 0.463 | 0.448 | 0.455 | 0.433 |
| **$\Delta$B** | $\Delta$Br | 0.005 | 0.000 | 0.060 | 0.056 | 0.044 | 0.049 |
| (nT) | $\Delta$Bt | 0.004 | 0.000 | 0.020 | 0.020 | -0.005 | 0.019 |
| | $\Delta$Bn | 0.007 | 0.000 | 0.010 | -0.014 | -0.020 | -0.010 |

**Table 5.1**. Summary of observed and predicted magnetic fields used for the variable width, variable depth notch analysis. $\Delta$B represents the difference between the illustrative and observed magnetic fields. MAG's 1-$\sigma$ uncertainties are $\delta$B = ($\pm$0.06, $\pm$0.02, $\pm$0.02) nT in R, T, N.

For each epoch, agreement between HET 1 and HET 2 can be achieved

using a B-field that falls within MAG's 1-$\sigma$ uncertainties, $\delta$B = ($\pm$0.06, $\pm$0.02, $\pm$0.02) nT in R, T, N. Magnetic fields used to obtain the results described below are listed in Table 5.1 and shown in Figure 5.9. The observed values and their uncertainties are included. In principle, differing combinations of $B_r$, $B_t$, and $B_n$ can produce identical pitch angles for HET 1, so alternate solutions do exist. Illustrative magnetic fields were chosen to reflect the least deviation from the reported measurements, preserving the magnitude, |B|.

### 5.3.4 Omni-70° Results: Predictions and Comparison with Observations

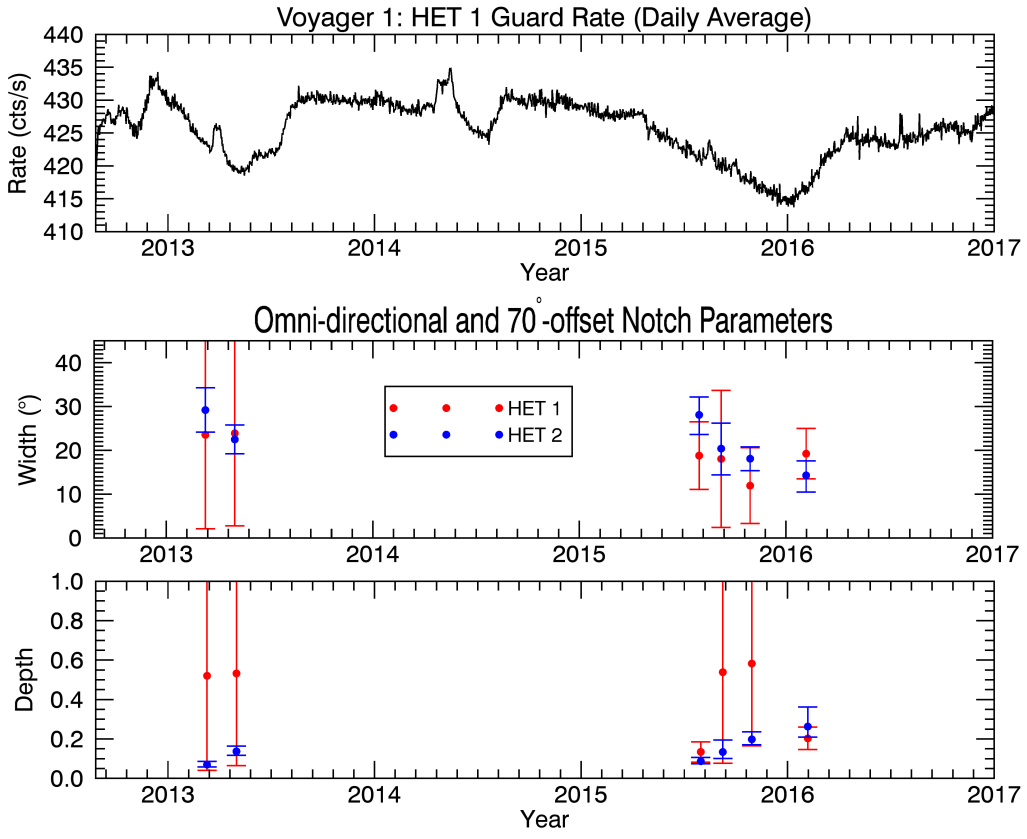


**Figure 5.10**. Widths and depths predicted from the intersection of omnidirectional and 70°-offset simulations for HET 1 (red) and HET 2 (blue) incorporating the illustrative field listed in Table 5.1.

Figure 5.10 shows the notch parameters obtained using the illustrative B-field (Table 5.1) to achieve consistency between HET 1 & 2 omnidirectional and 70°-offset response function curves (also listed in Appendix E, Tables E.3 & E.4). The two sets of results are consistent with one another, favoring a broad, shallow notch that is, on average ∼22°-wide and ∼15% deep. For four epochs, HET 1's 70°-offset curves matched the omnidirectional curves over a broad range of widths and depths, and therefore could not effectively provide constraint to the notch's geometry. However, for two epochs (2015-208 and 2016-31), the curves were sufficiently different to allow HET 1 to confirm the broad, shallow notch seen by HET 2. Regarding uncertainties, one should note that preserving the observed notch areas ($\delta_{\text{omni}}$ and $\delta_{70^\circ}$) causes width and depth to vary as inversely proportional to one another. In other words, the wider the notch, the shallower the depth.

The results from HET 1 and HET 2 roll maneuver fits are shown in Figure 5.11 and also listed in Appendix E (Tables E.5 & E.6). These fits are performed according to the procedure outlined in Chapter 4, Subsection 4.4.2, but for varying depths and widths. HET 1 & 2 results agree for 4 out of the 6 epochs. HET 2's 2015-250 epoch had a poor fit with a P-value of 0.50% (see Table E.6, Appendix E). HET 1 and HET 2 also disagree for the preceding 2015-208 epoch. Perhaps the small shock enhancement on 2015-224 or the plasma oscillations that began on 2015-247 contributed to these outliers in HET 2. Finally, independently acquired HET 1 roll maneuver fits and HET 2 omni-70° results show encouraging agreement (Figure 5.12).

### 5.3.5 Omni-70° Approach: Advantages and Limitations

The omni-70° approach is the most successful so far in determining ranges for the notch's widths and depths that not only show consistency between HET 1 and HET 2, but also amongst the omnidirectional, 70°-offset, and roll

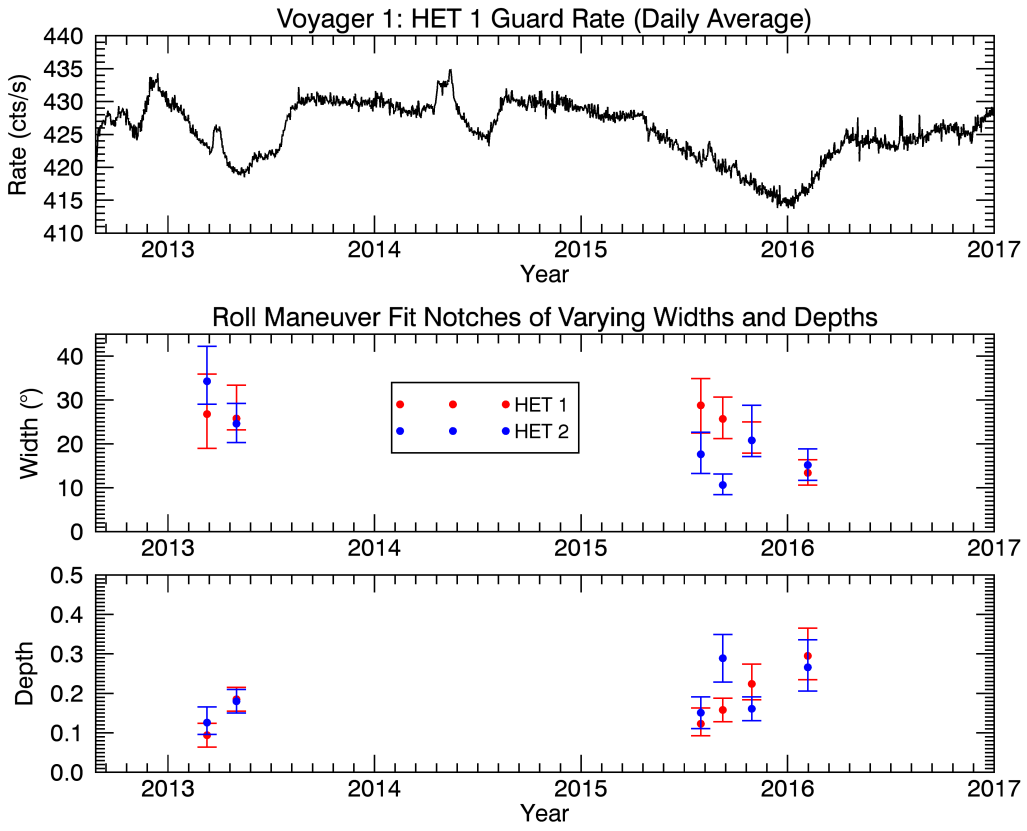


**Figure 5.11**. Widths and depths predicted from HET 1 and HET 2 roll maneuver fits for notches of varying widths and depths.

maneuver data. Although there was a general discrepancy between HET 1's 70°-offset and omnidirectional notch response function curves using nominal pitch angles, solutions exist for modified pitch angles using B-fields that are within MAG's uncertainties for all epochs.

This approach relies heavily on the assumption that the omnidirectional intensity changes primarily arise from the pitch-angle anisotropy, but those assumptions are in agreement with directional measurements not perpendicular to the B-field (recall Section 3.5). For example, HET 1 & 2 observe constant cosmic ray intensity (with the exception of several brief shock transients) when the spacecraft is in its usual configuration, during roll maneuvers when fields of view do not overlap with the notch, and for epochs when the

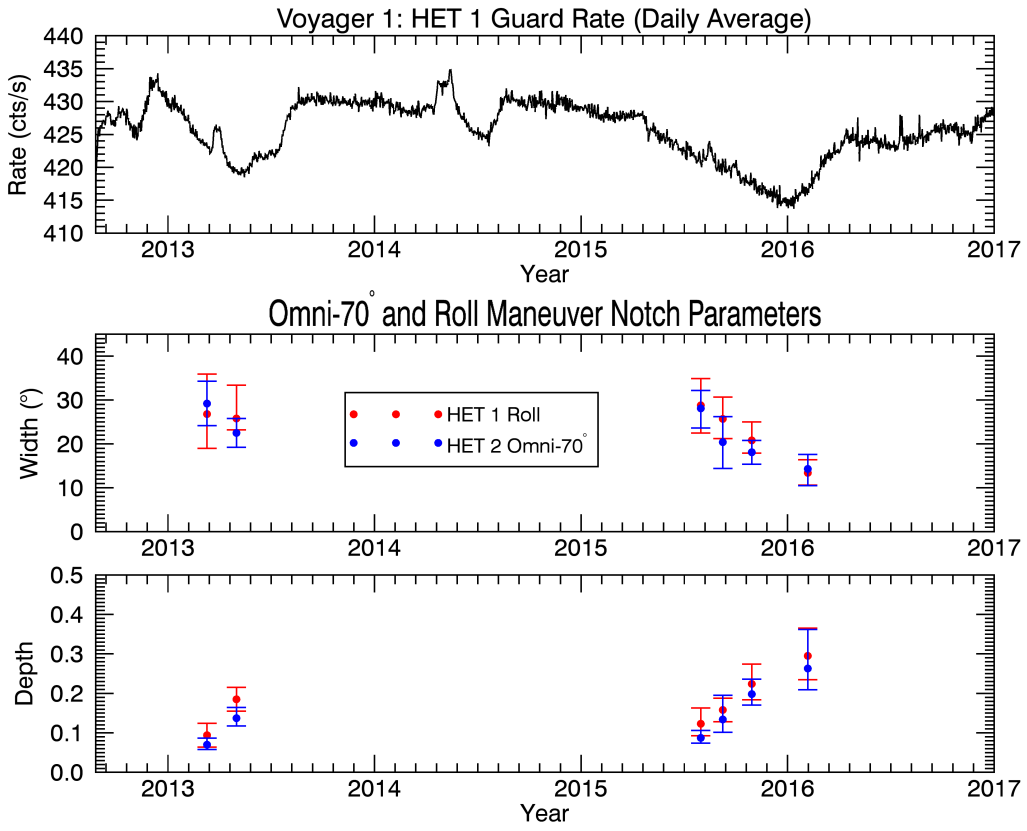


**Figure 5.12**. Comparison of HET 1 roll maneuver widths and depths (red) to HET 2 omni-70° results (blue).

anisotropy is temporally absent. LECP's sectored measurements agree with these conclusions.

### 5.3.6 Comparing Model #1 and Model #2

The modified boresight pitch angles from Model #2's illustrative fields merit a return to Model #1 in order to address the question: Are there illustrative fields that work for Model #1 that are within MAG's uncertainties? Table 5.2 compares the differences between the nominal and illustrative B-fields ($\Delta B_r$, $\Delta B_t$, and $\Delta B_n$ ) that are required to yield consistent results for each set of assumptions.

For all epochs, model #1 requires a larger than 1-$\sigma$ shift in at least two

| | | 2013-67 | 2013-120 | 2015-208 | 2015-250 | 2015-296 | 2016-31 |
|---|---|---|---|---|---|---|---|
| **Observed Magnetic Fields** | Br = | 0.175 | 0.178 | 0.118 | 0.117 | 0.152 | 0.132 |
| | Bt = | -0.444 | -0.421 | -0.402 | -0.392 | -0.379 | -0.370 |
| | Bn = | 0.200 | 0.188 | 0.197 | 0.183 | 0.200 | 0.180 |
| **Magnetometer Uncertainties** | $\delta$Br = | ±0.06 | ±0.06 | ±0.06 | ±0.06 | ±0.06 | ±0.06 |
| | $\delta$Bt = | ±0.02 | ±0.02 | ±0.02 | ±0.02 | ±0.02 | ±0.02 |
| | $\delta$Bn = | ±0.02 | ±0.02 | ±0.02 | ±0.02 | ±0.02 | ±0.02 |
| **Illustrative Field for Model #1 (Empty Notch)** | $\Delta$Br = | 0.090 | 0.069 | 0.091 | 0.058 | 0.088 | 0.049 |
| | $\Delta$Bt = | -0.066 | -0.029 | 0.045 | 0.061 | -0.030 | 0.049 |
| | $\Delta$Bn = | -0.001 | -0.006 | -0.046 | -0.051 | -0.029 | -0.048 |
| | $\sigma_r$ = | 1.5 | 1.2 | 1.5 | 1.0 | 1.5 | 0.8 |
| | $\sigma_t$ = | 3.3 | 1.5 | 2.3 | 3.1 | 1.5 | 2.5 |
| | $\sigma_n$ = | 0.1 | 0.3 | 2.3 | 2.6 | 1.5 | 2.4 |
| **Illustrative Field for Model #2 (Partially -Filled Notch)** | $\Delta$Br = | 0.005 | 0.000 | 0.060 | 0.056 | 0.044 | 0.049 |
| | $\Delta$Bt = | 0.004 | 0.000 | 0.020 | 0.020 | -0.005 | 0.019 |
| | $\Delta$Bn = | 0.007 | 0.000 | 0.010 | -0.014 | -0.020 | -0.010 |
| | $\sigma_r$ = | 0.1 | 0.0 | 1.0 | 0.9 | 0.7 | 0.8 |
| | $\sigma_t$ = | 0.2 | 0.0 | 1.0 | 1.0 | 0.3 | 1.0 |
| | $\sigma_n$ = | 0.3 | 0.0 | 0.5 | 0.7 | 1.0 | 0.5 |

**Table 5.2**. Comparison of estimated fields required for empty (variable width, 100% depth) vs. partially-filled notch models using the illustrative, adjusted B-field approach to yield agreement between omnidirectional and 70°-offset response function curves for HET 1 & 2. The $\Delta$B's reflect differences between the estimated and original B-fields.

B-field components, while model #2 requires shifts no larger than 1-$\sigma$ in each component. Thus, model #2's partially-filled notch approach is in better agreement with MAG observations, in addition to producing consistent CRS observations.

## 5.4 Electron Observations

Figure 5.13 and Appendix F (Table F.1) summarize HET 1 and TET 70°-offset observations from the end of 2012 through the end of 2016. An unexpected finding is that while protons show clear evidence of the pitch angle anisotropy, electrons do not. This is most readily denoted by two aspects of the 70°-offset data. First, TET's average boresight is nominally centered at ∼88° pitch angle during 70°-offsets, while HET 1's B-end boresight is at ∼77° (Table 3.1). Even allowing for an adjusted B-field (Subsection 5.3.3), TET's average boresight is

$\sim$87° while HET 1's is $\sim$81°. Thus, if the physical mechanism producing the anisotropy is species-independent, TET is expected to observe a larger count rate reduction compared to HET 1 (taking into account their differing geometry factors). However, TET's TAN rate reductions are negligible compared to HET 1's PENH rate (Figure 5.13b). Second, B-stopping electrons (BSe) and protons (BSp) enter the same end of the telescope, but the BSe rate (Figure 5.13d) remains largely unaffected compared to BSp (Figure 5.13c).

A quantitative illustration of the electron vs. proton observations is made in a final example using the 2015-296 offset epoch. Despite TET's boresight being better centered on the notch ($\alpha_{\mathrm{TET}} = 86°$ vs. $\alpha_{\mathrm{H1}} = 83°$), TET TAN observed only a $1.4\% \pm 0.7\%$ reduction[5.1] compared to HET 1 PENH's $11.0\% \pm 0.3\%$. In addition, HET 1's proton and electron B-stopping modes are expected to see the same amount of reduction if the anisotropy is not species dependent. Yet, BSp observed a $9.7\% \pm 1.0\%$ intensity decrease while BSe observed a $2.6\% \pm 1.7\%$ increase. Thus, the evidence suggests that the pitch angle anisotropy is only weak, at most, for TAN electrons ($\sim$5 to $\sim$105 MeV) and BSe electrons ($\sim$3 to $\sim$14 MeV).

[5.1] $\sim$0.4% of this is accounted for by TET TAN's estimated $\sim$4% proton background; recall Note (2) of Table 2.1.

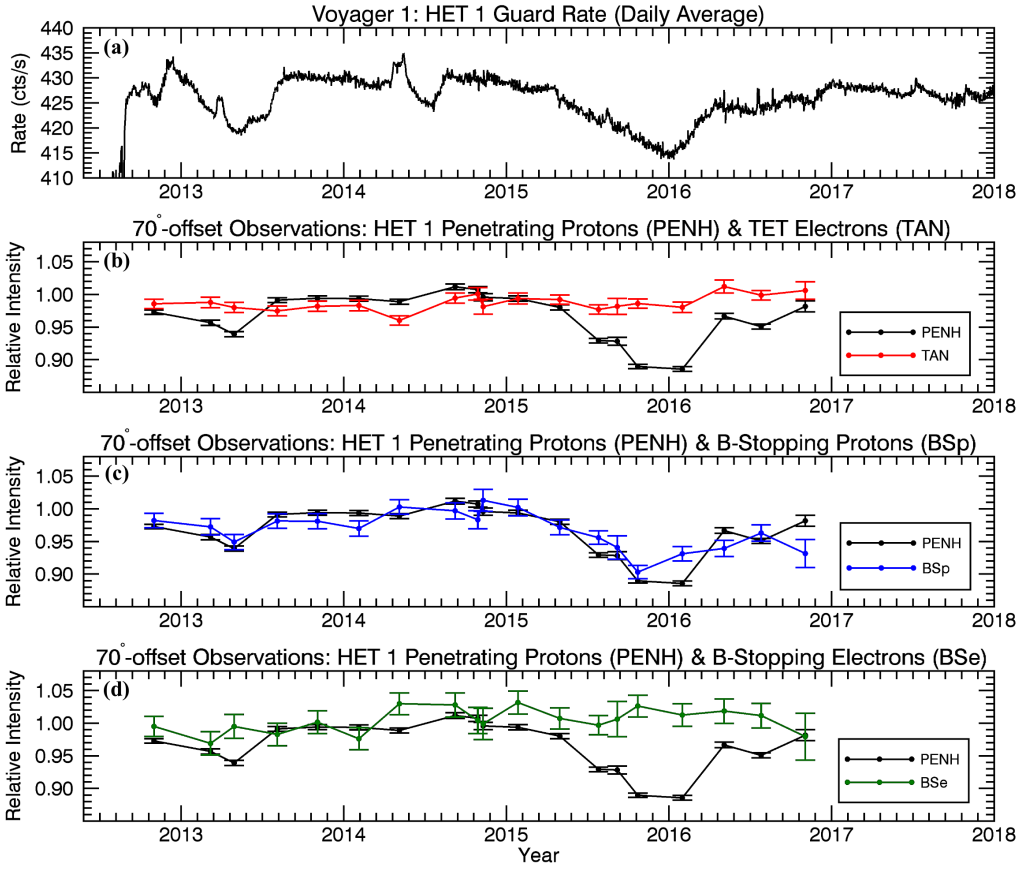


**Figure 5.13**. 70° offset observations for protons and electrons.
(a) HET 1's omnidirectional guard rate ($\gtrsim$ 20 MeV; proton-dominated) shows the time-varying GCR intensity reductions caused by the pitch-angle anisotropy.
(b) TET's unidirectional TAN rate ($\sim$5 to $\sim$105 MeV; electron-dominated) and HET 1's bi-directional PENH rate ($\gtrsim$ 70 MeV; proton-dominated) during 70°-offset maneuvers. Intensities are normalized to the temporally-adjacent non-offset rates for each particular telescope mode.
(c) HET 1's unidirectional B-stopping proton rate (BSp; $\sim$18 to $\sim$70 MeV) and bi-directional PENH rate ($\gtrsim$ 70 MeV; proton-dominated) during 70°-offset maneuvers.
(d) HET 1's unidirectional B-stopping electron rate (BSe; $\sim$3 to $\sim$14 MeV) and bi-directional PENH rate ($\gtrsim$ 70 MeV; proton-dominated) during 70°-offset maneuvers. The electrons in panels (b) and (d) show a substantial lack of pitch angle anisotropy compared to protons.

# Chapter 6
# Discussion: The Anisotropy's Formation and Temporal Evolution

## 6.1 A Story from the Cosmic Ray Perspective

Consider an isotropic distribution of ∼100-MeV cosmic ray protons traveling along a 0.48 nT uniform magnetic field ($|\mathrm{B}|_{\mathrm{ism}}$) through the interstellar medium, with gyroradii $r_g = 0.021$ AU and gyroperiods $\tau_g \simeq 150s$. Due to very large scattering mean free paths in the ISM, such particles gyrate about local field lines (moving parallel along the field) for $\sim 10^4$ astronomical units without scattering, so long as the magnetic fields remain quiescent (see Appendix G, Section G.1).

Now suppose a spherical magnetic disturbance emanates from the sun and propagates radially outward through the heliopause into the interstellar medium, at a constant speed, $\mathrm{V}_s$. The disturbance compresses the magnetic field to a value $|\mathrm{B}|_{\mathrm{shock}}$, where $|\mathrm{B}|_{\mathrm{shock}} > |\mathrm{B}|_{\mathrm{ism}}$ within a region of thickness, L. When the particles encounter the gradient in the field produced by this transient event, they will likely continue along, undisturbed if $r_g >> \mathrm{L}$. But if $r_g < \mathrm{L}$ will interact in one of two ways depending on their $\alpha$, and a critical value, $\alpha_c$, generated by the disturbance: 1) particles with $\alpha \geq \alpha_c$ will be reflected upstream away from the shock, while 2) particles having $\alpha < \alpha_c$ will pass through it.

The reflection occurs because the disturbance acts as a magnetic mirror. The critical value is defined as follows: conservation of the first adiabatic invariant implies that

$$\frac{\sin^2\alpha(x)}{\mathrm{B}(x)} = \frac{\sin^2\alpha_o}{\mathrm{B}_o} = \text{const.} \tag{6.1.1}$$

(for a distance $x$ along the field line and values $\alpha_o$ and $\mathrm{B}_o$ at the point of observation). In terms of particle velocities,

$$\frac{\sin^2\alpha(x)}{\mathrm{B}(x)} = \frac{1-\left(\frac{v_{||}}{v}\right)^2}{\mathrm{B}_o}. \tag{6.1.2}$$

As they proceed toward the increased fields of the disturbance, $v_{||}$'s will decrease and $\alpha$'s will increase until they reach $\alpha = 90°$. At that point, the parallel velocity vanishes causing the particles' motion to all be in the $v_\perp$ mode, and the parallel component of the Lorentz force (known as the "mirror force") takes over,

$$m\frac{dv_{||}}{dt} = \frac{1}{2}\frac{mv_\perp^2}{\mathrm{B}}\frac{\partial \mathrm{B}}{\partial x} \tag{6.1.3}$$

causing the particles to reverse directions and accelerate towards lower B-values. The mirror point at the disturbance can be represented as:

$$|\mathrm{B}|_{\text{shock}} = \frac{|\mathrm{B}|_{\text{local}}}{\sin^2\alpha_c}. \tag{6.1.4}$$

Taking the square root and re-arranging leads to:

$$\mu_c = \cos\alpha_c = \sqrt{\left(1-s\right)}, \tag{6.1.5}$$

where $s$ is the ratio of the local field, $|\mathrm{B}|_{\text{local}}$, to the disturbance's field, $|\mathrm{B}|_{\text{shock}}$ ($|\mathrm{B}|_{\text{local}} < |\mathrm{B}|_{\text{shock}}$).

To summarize, the condition for particle reflection at the shock is:

$$\mu \leq \sqrt{1-\frac{|\mathrm{B}|_{\text{local}}}{|\mathrm{B}|_{\text{shock}}}} \tag{6.1.6}$$

and the condition for transmission is:

$$\mu > \sqrt{1-\frac{|\mathrm{B}|_{\text{local}}}{|\mathrm{B}|_{\text{shock}}}} \tag{6.1.7}$$

How the particles gain energy at the reflection, or what occurs in the

downstream region of the shock depends on the surrounding environment and the particular model. In 2017, Kóta and Jokipii developed a model to explain how GCRs respond to shocks in the VLISM [3]. In the plasma frame, particles moving along the field that encounter a perpendicular shock experience a momentum change given by:

$$\frac{\mathrm{d}P^2}{\mathrm{d}t} = \left(\frac{P_\perp^2}{\mathrm{B}}\right)\frac{\mathrm{DB}}{\mathrm{D}t} \tag{6.1.8}$$

where $\mathrm{D}/\mathrm{D}t$ is the Lagrangian time derivative ($\mathrm{D}/\mathrm{D}t = \partial/\partial t + v_p \partial/\partial x$). In the VLISM, the shock propagates nearly perpendicular to the field and the velocity of the plasma ($v_p$) is negligible [45]. Since the first adiabatic invariant is conserved, $P_\perp^2/\mathrm{B}$ is constant and the amount of energy gained or lost is proportional to the amount of time spent near the compression or expansion regions ($\mathrm{DB}/\mathrm{D}t$).

The illustration in Figure 6.1a summarizes this model. Region I represents the compression region. Here, both the field strength, B, and plasma density, $n$, increase, and the particles gain energy. Region II represents the expansion region, where magnetic fields weaken and the GCRs cool. According to the theory, it is in region II where the pitch angle anisotropy occurs. Because GCRs have a negative spectral component in the VLISM (higher intensities at lower energies; recall Chapter 2, Section 2.3), energy gains translate to an increase in intensity and energy losses translate to a decrease in intensity (see Appendix G, Section G.2 for more details).

Now, consider how the particles interact with the shock from Voyager 1's perspective. When Voyager is on a field line that is connected to the shock (e.g. in the $\mathrm{B}_0$ region in Figure 6.1b), CRS or LECP will detect the newly-energized, mirrored particles via increased count rates. According to [3], the particles do not gain their energies by being instantly accelerated at the shock; rather their energy change is continuous, in proportion to the time they spend in the

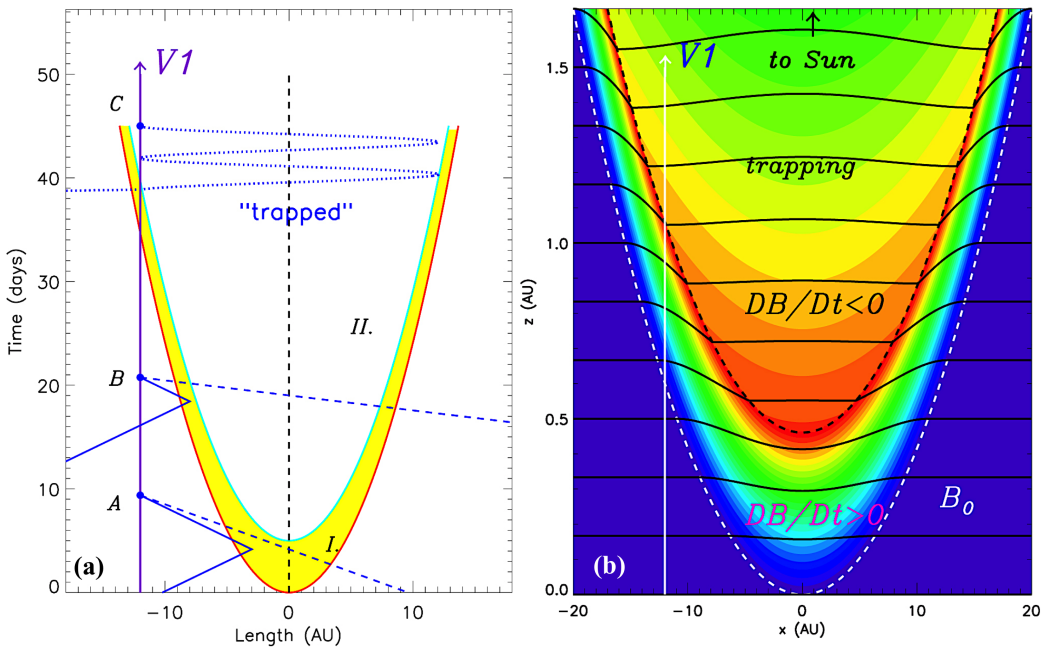


**Figure 6.1**. Illustration (a) and simulation (b) of Kóta and Jokipii's adiabatic heating/cooling model to explain particle interactions with shocks in the VLISM [3]. (a) According to the model, GCRs gain energy as they spend time in the compression region (I) and lose energy as they bounce in the expansion region (II). The zero of the time axis marks the time when a field line first connects to the compression's leading edge. As particles interact with the shock, those with $\mu \leq \mu_c$ are reflected (solid lines) or trapped (dotted), while those with $\mu > \mu_c$ are transmitted (dashed). Observation points A, B, and C mark when Voyager encounters the particles in their various sample scenarios (the trajectories are exaggerated for visualization purposes). From Figure 2 of [3].
(b) A simulation of the perpendicular shock in terms of its magnetic fields, viewed in the shock frame. The horizontal black lines represent the magnetic field lines of the VLISM. The shock consists of a gradual compression (DB/D$t > 0$, between the dashed lines; region I of panel a) followed by slow expansion (DB/D$t < 0$; region II of panel a) of the magnetic fields (red = stronger field, blue = weaker). The field strengths are exaggerated for visualization purposes. In the model, the shock moves radially outward from the sun at $V_s = 40$ km/s and in the shock frame, Voyager (V1) moves upward at 23 km/s. From Figure 1 of [3].

compression region (DB/D$t > 0$ in Figure 6.1b). Hence, the width of these shock spike events should reflect the shock's thickness. Concerning pitch angles, particles with $\alpha$ near 90° get reflected. As such, they spend the least time in the compression region and therefore gain the least energy. In contrast,

particles with $\alpha$ near the $\alpha_c$ (Equation 6.1.5) should gain the most energy because they penetrate further into the compressed region before mirroring. As Voyager itself traverses the compression (Figure 6.1b, between the dotted lines) it should detect a slow rise in the field's strength as it increases to maximum (Figure 6.1b, red).

By the time Voyager arrives in the downstream region ($\mathrm{DB/D}t < 0$ in Figure 6.1b), the pitch angle anisotropy should start to develop as already-trapped particles lose energy in the weakening field. Particles with $\alpha$ near 90° ($\mu \approx 0$) bounce back and forth, trapped between the enhanced fields of the shock's boundary (Region II in Figure 6.1a and between the red enhancements in Figure 6.1b).

The condition for bouncing is the same as for reflection in a static field, and is similar to the equation upstream of the shock (Equation 6.1.6)[6.1]:

$$\mu^2 \leq \frac{(|\mathrm{B}|_{\mathrm{shock}} - |\mathrm{B}|_{\mathrm{local}})}{|\mathrm{B}|_{\mathrm{shock}}}. \tag{6.1.9}$$

As particles bounce, they spend more time in the expansion region and continuously cool. Therefore, Voyager should observe a linearly decreasing trend in their intensities as a function of time. The depletion should also be independent of energy; within the same cooling time, faster GCRs bounce more frequently and thus experience roughly the same energy loss and intensity depletion as slower particles of the same $\mu$. Particles with larger $\mu$ (smaller $\alpha$) spend less time cooling due to larger distances between consecutive bounces, and those with $\mu > \sqrt{1 - \mathrm{B_{local}/B_{shock}}}$ escape entirely. Finally, the anisotropy's decreasing trend should stop when the field is no longer weakening [3].

For the above story to be a valid description of what is happening in the VLISM, several features should be present in Voyager 1's observations. First,

[6.1] Upstream, the local field is that of the unperturbed ISM ($|\mathrm{B}|_{\mathrm{local}} = \mathrm{B_{ism}}$). Downstream, the local field is increased compared to that of the ISM, but weaker than that of the shock ($\mathrm{B_{ism}} < |\mathrm{B}|_{\mathrm{local}} < |\mathrm{B}|_{\mathrm{shock}}$).

in order for the particles to interact with these magnetic transient events, the shock thicknesses should be larger than the gyroradius of the observed energetic particles. Second, the frequency and timing of the shocks should be consistent with measurements of the temporal evolution of galactic cosmic ray intensities. Third, the characteristics of the pitch angle anisotropy should relate to the behavior of the magnetic field. Each of these features are examined in detail in the following sections.

## 6.2 Voyager 1's Observations of VLISM Shock Transient Events

Between Voyager's heliopause crossing on 2012-238 (2012.65) and the beginning of 2017, MAG measured two significant increases in magnetic field strength that occurred around 2012-335 (2012.92) and 2014-236 (2014.65) [45]. These disturbances were each preceded by electron plasma oscillations – well-known shock precursors that arise from electron beam instabilities – detected by the Plasma Wave Subsystem (PWS) [4]. Additionally, abrupt enhancements in cosmic ray intensities – typically lasting a month at a time – have been observed by LECP and CRS, and are reminiscent of the shorter-lived particle spikes produced at the foreshock of interplanetary shocks, modeled by [3, 46] and noted by [4].

Although these events share many similarities with their interplanetary counterparts, they also have features that are startlingly different, as will be addressed in the following subsections. First, observations in the upstream region will be discussed (when Voyager senses particles interacting with the remote shock), followed by the shock crossing itself (when magnetic field changes are detected by Voyager), and then the downstream region (where the pitch angle anisotropies might occur).

### 6.2.1 Upstream Observations

The energetic particle enhancements ("shock spikes") observed by CRS are small (∼1.5% in the omnidirectional intensities), last roughly a month, and affect several-hundred MeV cosmic rays, whereas enhancements near 1 AU can have 100-fold intensity increases (and greater), might last only minutes, and typically involve particles of ∼100 keV to several MeV in energy [4, 57–59].

The plasma oscillations detected by PWS in the VLISM are analogous to known precursors to terrestrial bow shocks and shocks propagating outward from energetic events at the sun [4]. The emissions occur at the electron plasma frequency, $f_p = 8980\sqrt{n_e}$ Hz, where $n_e$ is the electron density of the plasma (in units of $\mathrm{cm}^{-3}$). Shortly after the heliopause crossing, the detection of these fortuitous events enabled PWS to measure a plasma density of 0.08 $\mathrm{cm}^{-3}$, which was closer to the expected value of the VLISM (∼0.1 $\mathrm{cm}^{-3}$ [27]) than the observed value of the outer heliosphere (∼0.002 $\mathrm{cm}^{-3}$ [21]). This finding resolved the initial uncertainty about whether or not Voyager 1 had finally reached interstellar space [32].

The mechanism for plasma oscillations inside the solar system is well understood. The emissions consist of Langmuir waves generated by electron beam instabilities that are driven by shock-accelerated electrons. These energized electrons escape along magnetic field lines in an upstream region known as the "electron foreshock" [60, 61]. The electron beam energies are relatively low (typically several hundred eV to a few keV), so the foreshock's leading edge is located far behind the initial field line that is tangent to the shock. Ions escaping from the shock typically have lower velocities, so ion foreshocks are known to follow electron foreshocks in the inner solar system [4].

Applying these concepts to the VLISM, [4] introduced an interstellar precursor model and related it to observations near the 2014-236 shock, illustrated

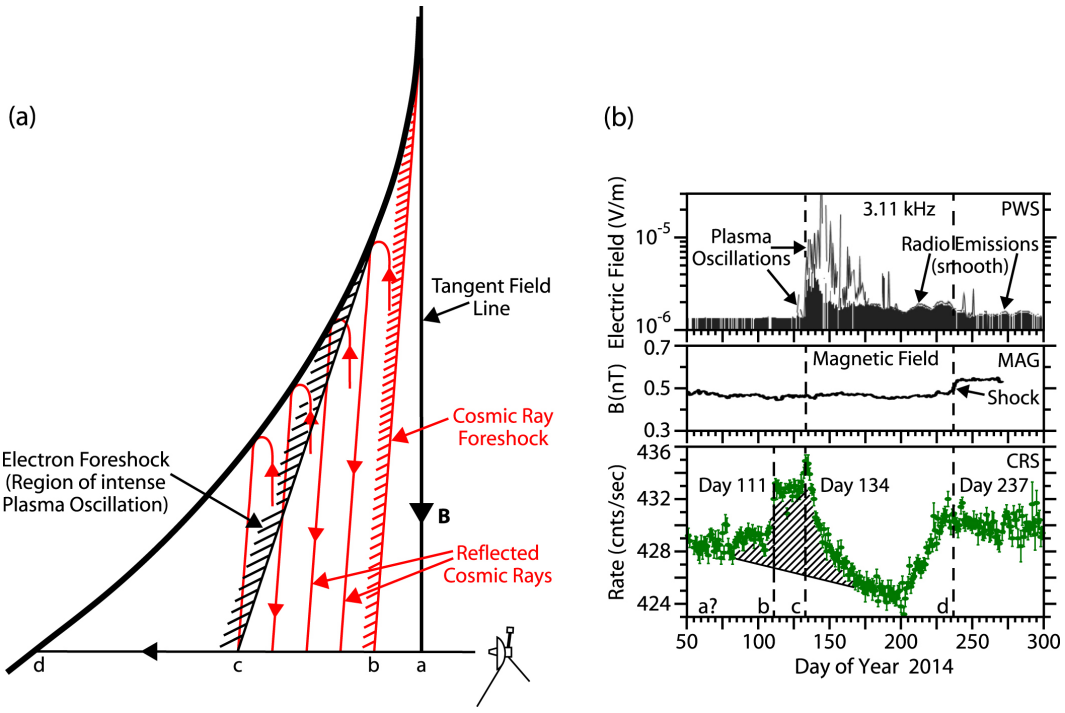


**Figure 6.2**. Illustrated sequence of VLISM shock precursor events as viewed by Voyager – from Figure 8 of [4].
(a) Cartoon of the cosmic ray foreshock and electron foreshock in relation to Voyager's trajectory towards the shock. Although the diagram is with respect to the shock's reference frame, the velocity of the corresponding observed shock (panel b) is ∼60 km/s [45], Voyager 1's velocity is 17 km/s, and both are traveling outward from the sun.
(b) Observations of events leading up to the 2014-237 shock, including the cosmic ray shock spike observed by CRS (bottom; HET 1 guard rate), followed by the plasma oscillations observed by PWS (top), and lastly, the shock itself observed by MAG (middle).

in Figure 6.2. At point (a), Voyager comes into contact with a field line tangent to the leading edge of the shock's compression region. The closest set of observations to this point is that of ultra-relativistic electrons (detected by TET[6.2] on CRS). Point (b) indicates the start of a "cosmic ray foreshock". This is a region that is encountered well ahead of the electron foreshock since cosmic ray protons have higher speeds than the plasma electrons (for ∼200 MeV cosmic rays, $v_p = 0.6c$ compared to $v_e = 0.06c$ for ∼1 keV electrons). In

[6.2]The median energy of TAN electrons is ∼13 MeV (recall Table 2.1), which corresponds to a Lorentz factor of $\gamma \approx 700 >> 1$.

the observations, the arrival of the highest-energy protons corresponds to the leading edge of the GCR intensity shock spike (Figure 6.2b, bottom panel). The plasma oscillations are detected when Voyager reaches point (c) (Figure 6.2b, top panel). The onset of the emissions is indicative of the leading edge of the electron foreshock. At point (d), Voyager finally crosses the shock itself and measures a jump in magnetic field strength (Figure 6.2b, middle panel).

For the most part, this sequence of upstream precursor events is consistent with Voyager 1 observations. Within the 2012.65 to 2017 timeframe, 5 plasma oscillations events were detected (Figure 6.3c), and each was preceded by an intensity enhancement in the cosmic rays, seen in CRS's directional (Figure 6.3a) and omnidirectional (Figure 6.3b) rates and also by LECP (not shown)[6.3].

According to MAG observations, Voyager encountered two forward shocks in late-2012 and mid-2014, and two possible reverse shocks in mid-2013 and mid-2015 (Figure 6.3d) [45]. It is noted that a shock signature in the magnetic field may not necessarily follow Voyager's observation of the upstream events; an absence of a local shock could simply imply that Voyager was magnetically connected to the shock front, but did not cross it [4].

### 6.2.2 At the Shock

The forward shocks observed by Voyager 1 in the VLISM are considered weak, subcritical, laminar, quasi-perpendicular shocks [23, 45]. Their properties are summarized in Table 6.1.

First, the shocks are considered weak since their magnetic field strength

[6.3] An exception to this is the enhancement in omnidirectional intensities near 2012-335 (∼2012.92; Figure 6.3b). Although it is tempting to attribute this to a shock spike, it occurs after the 2012 plasma emissions, at the same time that Voyager crosses the shock. A suggested interpretation of the late-2012 shock precursors is that the particle enhancements were either not seen (they occurred before Voyager's 2012.65 heliopause crossing), or they occur just after the crossing (note ∼2012.75 in Figures 6.3a & 6.3b). Either of these latter interpretations agree with the upstream sequence of GCR enhancements followed by the plasma oscillations, followed by the shock itself (cf. Figures 6.3c & 6.3d).

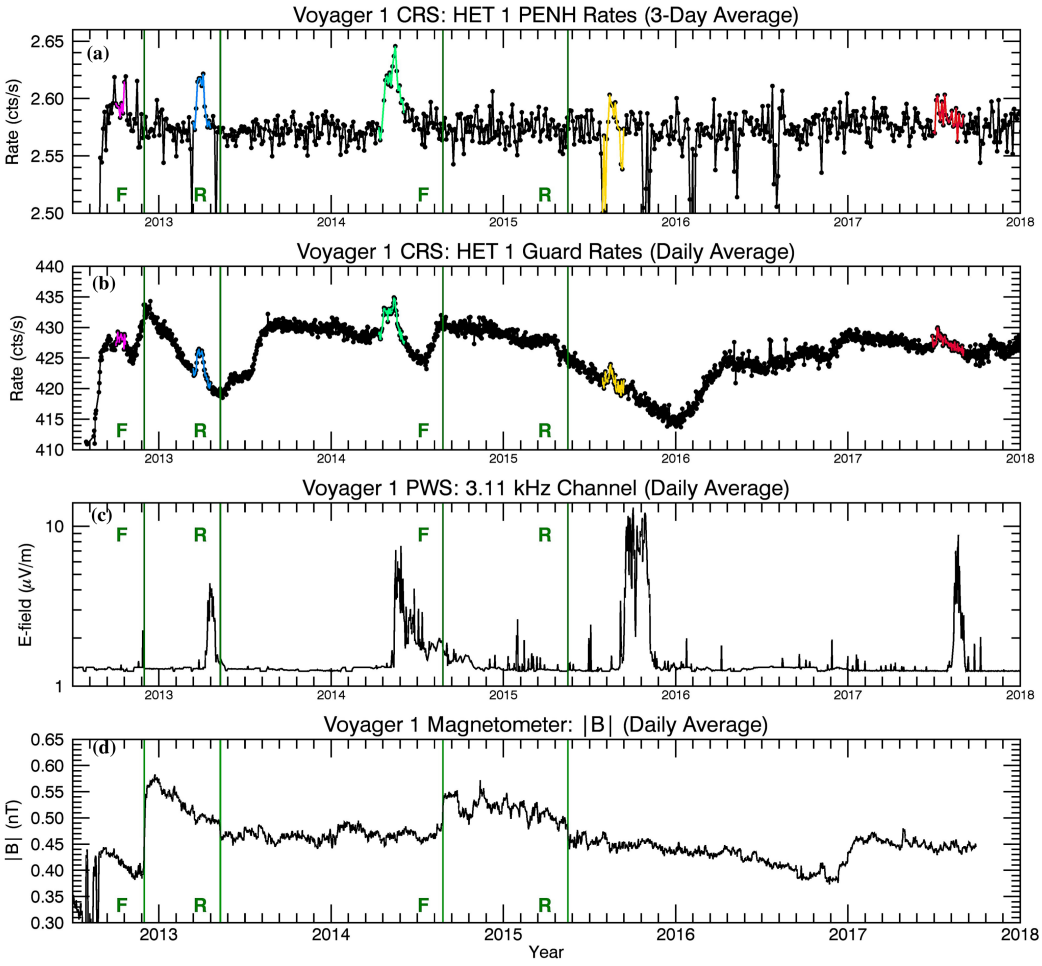


**Figure 6.3**. GCR shock spikes and electron plasma oscillations accompany weak shocks in the VLISM. Vertical lines on all four panels indicate the arrival times of the forward and reverse shocks reported by [45].
(a)(b) Cosmic ray precursor events are observed in CRS bi-directional PENH rates ($\gtrsim$ 70 MeV; proton-dominated)(a) and omnidirectional guard rates ($\gtrsim$ 20 MeV; proton-dominated)(b) prior to the electron emissions and shocks (HET 1 shown; spikes in color).
(c) Electron plasma oscillations arrive later than the cosmic ray events, since they are of much lower energies. The emissions are measured by the Plasma Wave Subsystem's (PWS) 16-channel spectrum analyzer and waveform amplifier. Electric field measurements from the 3.11 kHz channel of the spectrum analyzer are shown (see [4, 32]; from publicly-available data: http://www-pw.physics.uiowa.edu/voyager/data/).
(d) Following the upstream events, weak, subcritical, laminar, quasi-perpendicular shocks arrive at Voyager and are observed by MAG (see [23, 45]; from publicly-available data: https://omniweb.gsfc.nasa.gov/coho/form/voyager1.html).

| Year | DOY | $\|B\|_2/\|B\|_1$ | $V_s$ | $\Theta$ | Mach Number | $\mu_c$ | $\alpha_c$ |
|---|---|---|---|---|---|---|---|
| 2012 | ∼335 | 1.4 | ∼40 km/s | 85° | ∼1.1 | 0.53 | 58° |
| 2014 | ∼237 | 1.12 | ∼60 km/s | 80° | ∼1.1 | 0.35 | 70° |

**Table 6.1**. Summary of magnetic field observations for the 2012-335 and 2014-237 forward shocks. $|B|_2/|B|_1$ is the enhancement ratio ($B_1$ is prior to the shock), $V_s$ is the velocity of the shock, and $\Theta$ is the angle between the shock propagation direction and the field before the shock. See [23, 45] for further details. $\mu_c$ and $\alpha_c$ are calculated from the observed enhancement ratio using Equation 6.1.5 ($s = |B|_1/|B|_2$).

ratios are small (for reference, $|B|_2/|B|_1 \simeq 2.5$ at the termination shock [19]). Second, at 1 AU, shocks with magnetosonic Mach numbers $< 2$ are considered subcritical; these interstellar shocks have Mach numbers of $M \approx 1$ (in contrast, the supercritical termination shock has a Mach number of $M \approx 10$ [19]). Third, they exhibit the "laminar" property of having a very smooth and featureless transition across $|B|$. Fourth, they are quasi-perpendicular because the angles between the shock normals and the pre-shocked fields are almost 90° (Table 6.1).

The latter feature of the shocks is particularly relevant to the anisotropy in that it enables particles encountering the shock (traveling along the fields) to become trapped between the two mirror points formed by the shock's boundaries (recall Equation 6.1.9). Moreover, because Voyager also travels radially outward it has an ideal vantage point for viewing the adiabatically expanding fields and affected particles as the shock passes by.

A surprising additional observation about the VLISM shocks is that they are very thick. In both 2012 and 2014, their thicknesses were $L \approx 10^7$ km, roughly $10^4$ times thicker than their 1 AU counterparts. This detail also has important implications for Voyager's anisotropy observations and will be addressed shortly.

## 6.3 The Downstream Region

The VLISM pitch angle anisotropies are unusual compared to their solar system counterparts. Although cosmic rays are modulated by the solar wind, and shock-related decreases in energetic particle intensity are frequently observed (e.g. Forbush decreases; see [62]) these effects are mostly isotropic and short-lived – lasting days[6.4] – while variations reported here affect only particles with $\alpha$ near 90° and last hundreds of days. Kóta and Jokipii [3] were the first to develop a model relating the GCR pitch angle anisotropy to the combination of magnetic trapping and adiabatic cooling behind the shocks in the VLISM (described in Section 6.1). The present work is the first to explore the GCR anisotropy observations in light of their model. The focus of the remaining section is to quantitatively relate the results of CRS observations to the possible physics governing the anisotropy's formation (magnetic trapping) and evolution (adiabatic cooling).

### 6.3.1 Interactions of CRS Protons and Electrons with the Shock

Table 6.2 lists the median energies of particles observed by CRS in its various modes (recall Chapter 2, Subsection 2.2.1), along with their corresponding rigidities ($R$), gyroperiods ($\tau$), and gyroradii ($r_g$) calculated using the 0.48 nT average VLISM field observed by Voyager 1's magnetometer [45].

In all cases, $r_g < 10^7$ km, so particles interact with the shock in a way that preserves their first adiabatic invariants. Interestingly, $r_{gp} \simeq$ L for the non-stopping protons, while for the electrons, $r_{ge} \simeq 0.01$ L. The proton and electron gyroperiods also considerably differ: $\tau_p \simeq 100\ \tau_e$. A puzzle is that

[6.4] Near 1 AU, the onsets occur rapidly – lasting ∼hours to a day – and are followed by slow recoveries ∼1-10 days; [63].

| Mode | PENH | Guards | BSp | TAN | BSe |
|---|---|---|---|---|---|
| **Dominant Species** | protons | protons | protons | electrons | electrons |
| **Rigidity** $R$ (MV) | 1142 | 1037 | 287 | 13.5 | 6.49 |
| **Gyroperiod** $\tau$ (s) | 215 | 203 | 143 | 2.0 | 0.95 |
| **Gyroradius** $r_g$ (km) | $7.93 \times 10^6$ | $7.20 \times 10^6$ | $2.00 \times 10^6$ | $9.38 \times 10^4$ | $4.51 \times 10^4$ |
| **Gyroradius** $r_g$ (AU) | 0.053 | 0.048 | 0.013 | 0.00063 | 0.00031 |
| **Gyroradius in Terms of Shock Thickness** | 0.77 L | 0.71 L | 0.20 L | 0.0093 L | 0.0045 L |
| **Median Energy** | ∼540 MeV | ∼460 MeV | ∼43 MeV | ∼13 MeV | ∼6 MeV |

**Table 6.2**. Properties of VLISM particles listed according to the various CRS modes. Values are calculated using a magnetic field of $|B| = 0.48$ nT and shock thicknesses of L $\approx 10^7$ km $= 0.067$ AU, reported by [45].

TET on CRS observes shock spikes, so the electrons clearly gain energy and are reflected in the upstream region of the shock, which implies that they should get trapped and lose energy in the downstream region. Yet, electrons experience, at most, a small anisotropy (recall Chapter 5, Section 5.4). Perhaps their short gyroperiods and small gyroradii suggest that their notch gets rapidly filled in by pitch angle scattering caused by small-scale turbulence like that potentially caused by plasma wave electric fields [4].

### 6.3.2 Temporal Variation of the Anisotropy

According to CRS observations, GCR intensities decline for roughly 165, 60, and 260 days during the 2013, 2014, and 2015 episodes, respectively. If the cooling of particles in the weakening magnetic field downstream of a shock is responsible for the anisotropy's temporal evolution, the weakening would have to occur gradually. Such timescales are generally reflected in the MAG observations [45]. In Figure 6.3d, the magnetometer's first prominent forward shock arrived on 2012-335 (2012.915), coinciding with the start of the first GCR decrease (Figure 6.3c). During this time, the field was increased above its average value of 0.48 nT and slowly weakened until a reverse shock returned it to average around 2013-130 (2013.356). The magnetic field decrease lasted

∼161 days, about the same length of time as the ∼165-day GCR intensity drop during this time period. Moreover, the GCR intensity minimum also occurred near 2013-130 – following a prominent shocked-particle enhancement feature. The magnetic field quieted for the following months and the GCR intensities returned to isotropy.

The 2014 and 2015 anisotropy episodes present an interesting challenge because they are not as well correlated with local magnetic field behavior. The 2014 anisotropy coincided with the electron plasma oscillations (near 2014.4 in Figures 6.3c & 6.3d), and no obvious shock preceded it. One possibility is that Voyager did not measure the change in |B| because it remained upstream of this shock. Another possibility is that the 2014 and 2015 anisotropy episodes are connected to the same event. The timing of the GCR shock spike and the electron plasma oscillations fits the suggested sequence of precursor events leading to the 2014-236 forward shock. What, then, produced the anisotropy? According to [4], the emission spectrum for this event was unusual in that it revealed a clear parabola-shaped depression in plasma density. As a result, PWS observed trapped radio emission along with the plasma oscillations. They suggest that this cavity might also have trapped energetic particles. An alternate conjecture is that Voyager encountered field lines that were remotely connected to the downstream region of the shock (pre-decreases to Forbush decreases near 1 AU originate for similar reasons; [64–67]).

The largest anisotropy event to date occurred shortly after the 2014-236 (2014.647) forward shock and was marked by a shallowly-sloped reduction in GCR intensities that lasted roughly until the 2015-136 (2015.373) reverse shock. Afterward, the magnetic field and particle intensities decreased at a steeper rate for ∼260 days. However, the local magnetic field continued to decrease below average even as particle intensities reached their minimum (at

the beginning of 2016) and subsequently recovered in 2017.

### 6.3.3 Anisotropy Recoveries and the Nature of the Transient Events

The anisotropy recoveries are a challenge to explain since they are not well correlated with the local magnetic field. However, the timing of the plasma oscillations in relation to the 2013 and 2015 anisotropy episodes may provide some insight. Oscillations precede both episodes (∼2012.78 and ∼2014.37 in Figure 6.3d) and abruptly end at the onset of the forward shocks. This is to be expected since the plasma oscillations are known to occur upstream of the shocks, the change of magnetic field marks when the shock is at Voyager, and the particle trapping/adiabatic cooling occur when Voyager is downstream. Yet, there is a second set of plasma oscillations (∼2013.28 and ∼2015.68 in Figure 6.3a, 6.3b, & 6.3c) that occur in the midst of the anisotropy events. These are preceded by shock spikes in the high-energy particles (∼2013.22 and ∼2015.38 in Figure 6.3d) and occur near possible reverse shocks identified by MAG (∼2013.36 and ∼2015.61 in Figure 6.3d). Moreover, at nearly the same time that these oscillations end (∼2013.4 and ∼2015.9), GCR intensities reach their minima and begin recovery.

These occurrences imply that the transient disturbances are more complicated than simple forward shocks. For example, they could originate from merged interaction regions (MIRs) that arrive at the heliopause – first suggested by [68] – and generate pressure pulses that propagate into the VLISM [35] and steepen to form forward-reverse shock pairs.

Another possibility is that they imply a more complex shock shape. Figure 6.4 depicts a structure used by [3] to generate the intensity distribution in Figure 6.6b. In this scenario, the shock is perpendicular in two places, ≈ 30 AU apart. A second spike is observed ∼100 days after Voyager crosses the shock, when it reaches a field line that is connected to the shock at a small

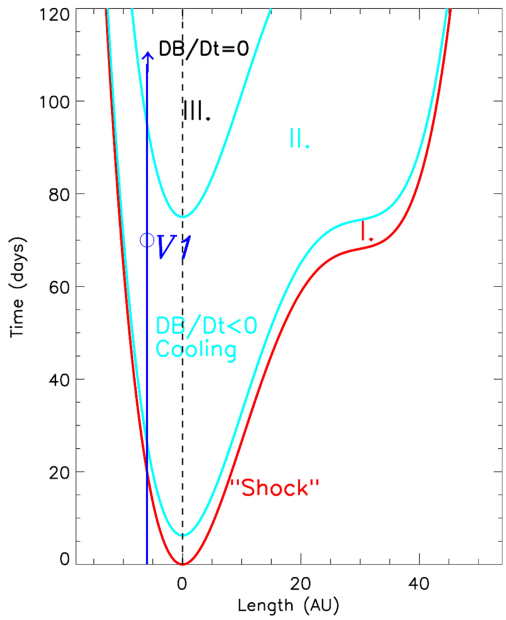


**Figure 6.4**. Schematic of the geometry used by Kóta and Jokipii to produce the complex shock compression shown on the right of Figure 6.6 (from Figure 4 of [3]).

angle. Evidently, some geometries might allow for Voyager to see particle enhancements (and perhaps plasma oscillations) from the same shock more than once.

Whatever the shape of the shock, or the nature of the magnetic structures might be, the recoveries likely occur as Voyager passes entirely through the structure, or it has dissipated enough that the previously-trapped particles escape the downstream region.

## 6.4 Physical Interpretation of the Notch's Characteristics

### 6.4.1 Relation to Magnetic Field Fluctuations

If the notch is produced by magnetic trapping (Equation 6.1.9), the size of fluctuations in both the steady-state and disturbed magnetic fields can be used to set limits to its characteristics. The magnetic field change required

to explain the notch's formation is determined by combining Equations 4.4.3 & 6.1.9:

$$\delta|\mathrm{B}|_n = (|\mathrm{B}|_{\mathrm{shock}} - |\mathrm{B}|_{\mathrm{local}})/|\mathrm{B}|_{\mathrm{shock}} = \cos^2(\alpha) = \cos^2(90^\circ - w/2). \quad (6.4.1)$$

During the quietest periods, average magnetic field fluctuations are on the order of $\sim$2% over several-week timescales [69, 70]. Given that the anisotropic decreases in GCRs endure for many months at a time, this quantity serves as a lower limit to $\delta|\mathrm{B}|_n$. An upper limit is informed by the more sudden changes in magnitude caused by the shocks. As mentioned in Subsection 6.2.2, the 2014 transient event produced a $\sim$12% change in |B| (see Table 6.1). Therefore, in order to be reasonably consistent with observations, it is expected that $2\% \lesssim \delta|\mathrm{B}|_n \lesssim 12\%$.

Returning to Model #1's 2015-310 epoch example, a 4°-wide notch ($\alpha = 88^\circ$) yields $\delta|\mathrm{B}|_n = 0.12\%$, which is much less than 2%. According to this model, even the largest omnidirectional intensity deviation measured to date ($\delta_{\mathrm{omni}} = 3.8\% \pm 0.2\%$ on 2016-11; see Section 5.2) produces only a 4.3° wide notch, for which $\delta|\mathrm{B}|_n = 0.14\%$. Evidently, the smallest fluctuations in field strength are much larger than the strength differences required to explain the anisotropy's formation using the empty notch model.

Averaging Model #2's six epochs yields a notch that is 22° wide and 15% deep, with an average $\delta_{\mathrm{omni}}$ of 2.9% (Subsection 5.3.4). Thus, $\delta|\mathrm{B}|_n = 4\%$. Since $2\% < 4\% < 12\%$, the formation of a broad, shallow notch implies changes in |B| that are consistent with the observed variations in the field.

### 6.4.2 Notch Widths and Depths Related to Expanded and Compressed Magnetic Fields

$\delta|\mathrm{B}|_n$ is calculated for the six epochs from Model #2 where the anisotropy is most prominent (Table E.4 in Appendix E applied to Equation 6.4.1). The results are summarized in Table 6.3. The table also includes the local field strength, $|\mathrm{B}|_{\mathrm{local}}$ (from observations; see Subsection 5.3.3, Table 5.1), and a predicted magnetic field strength at the shock, $|\mathrm{B}|_{\mathrm{shock}}$, calculated from $\delta|\mathrm{B}|_n$ and $|\mathrm{B}|_{\mathrm{local}}$ (Equation 6.4.1).

| **Epoch** | **width** | **depth** | $\delta_{\mathbf{omni}}$ | $\delta\|\mathbf{B}\|_n$ | $\|\mathbf{B}\|_{\mathbf{local}}$ | $\|\mathbf{B}\|_{\mathbf{shock}}$ |
|---|---|---|---|---|---|---|
| **2013-67** | 29°± 5° | 7% ± 1% | 1.8% ± 0.05% | 6% ± 1.3% | 0.52 ± 0.04 nT | 0.55 ± 0.12 nT |
| **2013-120** | 23°± 3° | 14% ± 2% | 2.7% ± 0.05% | 4% ± 0.6% | 0.49 ± 0.04 nT | 0.51 ± 0.10 nT |
| **2015-208** | 28°± 4° | 9% ± 2% | 2.1% ± 0.05% | 6% ± 1.1% | 0.46 ± 0.04 nT | 0.49 ± 0.10 nT |
| **2015-250** | 20°± 6° | 13% ± 5% | 2.4% ± 0.07% | 3% ± 1.1% | 0.45 ± 0.04 nT | 0.46 ± 0.17 nT |
| **2015-296** | 18°± 3° | 20% ± 3% | 3.1% ± 0.05% | 2% ± 0.4% | 0.45 ± 0.04 nT | 0.47 ± 0.09 nT |
| **2016-31** | 14°± 4° | 26% ± 8% | 3.3% ± 0.06% | 2% ± 0.4% | 0.43 ± 0.04 nT | 0.44 ± 0.13 nT |

**Table 6.3**. A listing of Model #2's notch parameters related to the estimated B-field variation required to produce the notch ($\delta|\mathrm{B}|_n$). Also shown is the predicted value for the magnetic field at the shock ($|\mathrm{B}|_{\mathrm{shock}}$) compared to the local field ($|\mathrm{B}|_{\mathrm{local}}$) for particles undergoing magnetic trapping (see Table 4.1 in Section 4.5, Figure 5.10 in Section 5.3, Table 5.1 in Subsection 5.3.3, and Table E.2 in Appendix E).

Returning to the original discussion on the anisotropy's formation through adiabatic cooling downstream of the shock (Section 6.1), $|\mathrm{B}|_{\mathrm{local}}$ represents the local field strength of the cooling region and $|\mathrm{B}|_{\mathrm{shock}}$ represents the increased strength of the disturbance (c.f. Equation 6.1.9 and Equation 6.4.1). By comparing the predicted $|\mathrm{B}|_{\mathrm{shock}}$ to observations, one can determine how well the notch model and magnetic trapping model agree.

Figure 6.5 shows the profile of the magnetic field strength during a late-2012 forward and mid-2015 reverse shock transient event (left and right panels, respectively). The largest predicted $|\mathrm{B}|_{\mathrm{shock}}$ in Table 6.3 occurs during the 2013-67 epoch, and its ∼0.55 nT value is very close to the maximum field strength (∼0.56 nT) of MAG's 2012-335 shock transient event (left panel of

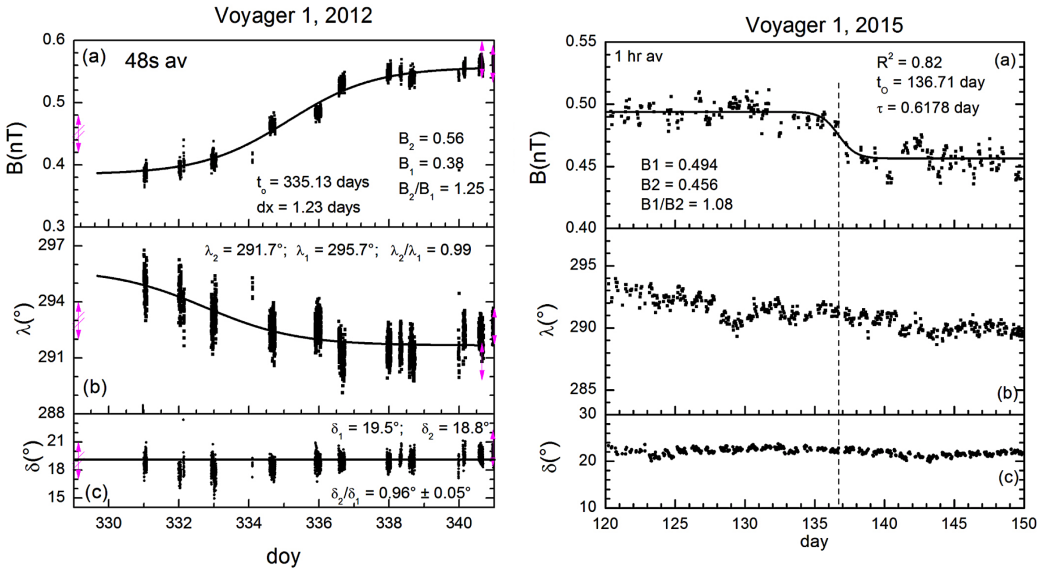


**Figure 6.5**. Sigmoidal (Boltzmann) curve fits to magnetic field strength profiles for forward (2012-335) and reverse (∼2015-137) shock transient events measured by Voyager 1's magnetometer in the VLISM. The magnetic field transitioned from 0.36 to 0.56 nT for the 2012 event and from 0.49 to 0.45 nT for the 2015 event. These particular events are of interest because they are proximate to the epochs considered for Model #2's notch analysis. The panels shown are subsets of Figures 3 & 5 from [45].

Figure 6.5). Shifting focus to the 2015 anisotropy event, during the 2015-208 epoch, the $|B|_{\text{shock}}$ of ∼0.49 nT agrees with the 0.494 nT field observed at the time of the 2015-137 reverse shock (right panel of Figure 6.5). In the remaining epochs, the shocked field decays until it reaches roughly the local value in 2016-31, and the anisotropy subsequently begins its recovery.

Two other trends in Table 6.3 are also worth mentioning: 1) the depths increase over time (per event) and the widths remain about the same. This makes sense in light of Kóta & Jokipii's model [3]; the magnetic field of the shock remains steady (indicated by the widths) while particles spend greater amounts of time cooling (indicated by the depths) as the intensities drop.

Additional evidence supports the physical interpretation that the notch is produced by trapping (widths) and its evolution is governed by adiabatic

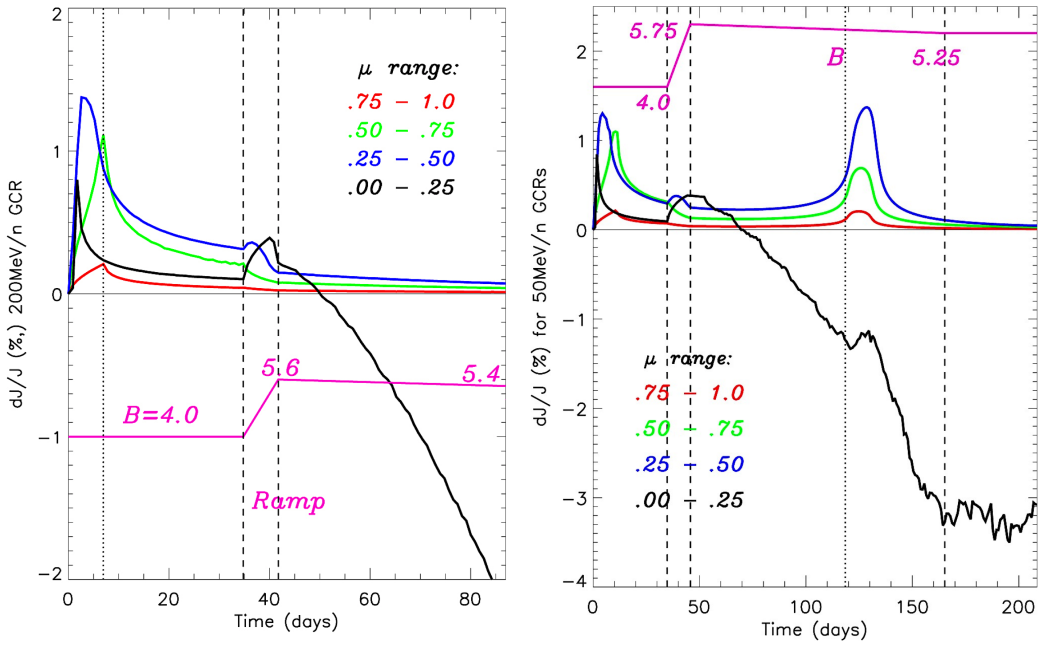


**Figure 6.6**. Predicted intensity vs. time from Kóta and Jokipii's simulation of a spherical (left) and more complex (right; see Figure 6.4) shell of compression generated by a gradual increase of |B| (units listed in $\mu$G) for magnitudes close to that of Voyager 1's 2012-335 shock (Figure 6.5). The intensities of 200 MeV/nuc (left) and 50 MeV/nuc (right) GCRs are calculated in four pitch-angle segments; the anisotropy is most clearly observed in the segment near $\alpha = 90°$ ($\mu = 0.00$ to 0.25). The panels shown are a combination of Figures 3 & 5 from [3].

cooling (depths) downstream of the weak interstellar shocks. Figure 6.6 shows intensity vs. time simulations from [3] of 200 MeV/nuc GCRs interacting with a spherical shock (Figure 6.6, left), and 50 MeV/nuc GCRs interacting with a more complex shock (Figure 6.6, right), both generated using B-fields approximating the 2012-335 shock. They predict a decreasing trend in the GCR flux for the $\mu = 0.00$ to 0.25 pitch angle segment and not in other segments ($\mu > 0.25$) for each geometry. This translates to a maximum notch width of: $w = 2 \times (90° - \cos^{-1}(0.25)) = 29°$. The present work's analysis concurs with their results; Model #2 predicted a ∼29°-wide notch for the epoch nearest to the ∼2012-335 shock (2013-67 in Table 6.3).

# Chapter 7
# Summary and Conclusion

Voyager 1 CRS measurements have been used to explore a GCR anisotropy in the LISM produced by a gap of particles in the intensity distribution that have pitch angles near 90°. Data were analyzed from three telescopes – HET 1, HET 2, and TET – using omnidirectional, bi-directional, and unidirectional count rates. Several types of functions were simulated and fit to data in order to characterize the "notch" of missing particles. These included cuts in pitch angle space – centered about $\mu = 0$ – of varying widths and depths in: 1) omnidirectional response functions, 2) during magnetometer calibration roll maneuvers, and 3) during 70°-offset maneuvers. The data taken during the spacecraft maneuvers proved advantageous for viewing the anisotropy. Nominal telescope field of views are pointed in such a way that they are unable to detect particles having near 90° pitch angles, whereas changes to the spacecraft's orientation enabled CRS fields of view to temporarily overlap with the notch region and measure its effects.

Two types of models were used in the analysis. Model #1 utilized a single effective width parameter (100% depth) to characterize the data, hence an empty notch. Performing fits to HET 1 and HET 2 bi-directional PENH ($\gtrsim$ 70 MeV; proton-dominated) rates for 25 roll maneuver epoch led to results that were then used to predict relative intensity reductions in 70°-offset and omnidirectional guard rates ($\gtrsim$ 20 MeV; proton-dominated). HET 1 predictions and observations agreed well for both types of data. The predictions for HET 2 during 70°-offsets, however, conflicted with observations. According to

simulations, no intensity reduction was expected – even during times when the anisotropy's effects were most prominent – yet small, statistically significant effects were observed. Moreover, it was shown that no width of notch could satisfy the empty notch constraint and produce consistency for both HET 1 and HET 2. Therefore, a second approach was pursued allowing for both variable width and depth.

Model #2's partially-filled notch required at least two types of response functions to separate the two parameters. One method was to use HET 1 & 2 70°-offset simulations for widths ranging from 0° to 45° and depths determined numerically by re-creating the observed intensity reductions. Since HET 2 had a weak signature, only the 6 most prominent epochs were used for the analysis. This method achieved an average notch width of 29.2° and depth of 11.2%. However, recreating omnidirectional intensity reductions from the resulting geometries gave predictions that deviated from observations by several sigma for 4 out of 6 epochs on HET 1 and 5 out of 6 on HET 2.

A second method was to treat HET 1 and HET 2 independently and find the overlap between a given telescope's 70°-offset and omnidirectional response function curves. During the 2013-120 epoch, HET 1's 70° offset curve overlapped with most of its omnidirectional counterpart, showing agreement for widths ranging from 2.8° to greater than 45° and depths from 100% down to less than 6.5%. However, HET 2's curves differed enough to constrain the notch's geometry to having widths ranging from 19.2° to 25.8° and depths from 11.8% to 16.4%, with nominal values of 22.5° and 13.7%.

The 2015 epochs presented a challenge in that HET 1's omnidirectional and 70°-offset curves showed no intersection within their respective uncertainties (informed by observational errors). An accounting for additional possible sources of uncertainty led to an analysis of the effects of MAG's uncertainties –

($\delta B_r$, $\delta B_t$, $\delta B_n$) = ($\pm 0.06$, $\pm 0.02$, $\pm 0.02$) nT – on the calculation of HET 1 and HET 2 boresight pitch angles. Was there a set of values within each of these field-component uncertainties that could allow agreement between HET 1's directional and omnidirectional curves while also retaining consistency between HET 1 and HET 2 interpretations of the notch's geometry? Such a field exists for all epochs. An illustrative field chosen to minimize each epoch's $\Delta B_r$, $\Delta B_t$, and $\Delta B_n$ was successful in demonstrating this. The first epoch, 2013-67, required minimal change, the second, 2013-120 required no change, and the later 4 epochs required larger changes, but all were within magnetometer errors. HET 2 constrained the notch's nominal values to have an average width and depth of 22° and 15%, ranging from nominal values of 14° to 29° and 26% to 7% over the multiple time periods. Independently calculated roll maneuver fits have nominal values of 24° and 18% for HET 1 and 21° and 20% for HET 2.

Unidirectional observations were used to assess the potential anisotropy differences between protons and electrons. It was discovered that, unlike the protons, electrons experience, at most, a small anisotropy. Their gyroradii, which differ by roughly a factor of 100 from the penetrating protons and gyroperiods which are shorter by also a factor of $\sim$100 suggest that their notches may be rapidly filled in by pitch angle scattering.

To summarize, the results from the analysis of CRS observations support that the notch producing the pitch angle anisotropy is broad and mostly filled for several reasons. First a broad, shallow notch produced consistent omnidirectional and bi-directional 70°-offset response function curves for HET 1 and HET 2, with agreement in their respective roll maneuver fits and consistency amongst the two telescopes. No effective width was found that could produce such agreement with the narrow, empty notch model. Second, Model #2 utilized adjusted B-fields for the 2015 and later epochs, but the 2013-120 epoch

revealed a broad notch with no modification to its field. The possibility of resolving Model #1's inconsistencies via a field within the limits of MAG's uncertainties was also explored, but no solutions were found. Third, if the notch is formed via a trapping mechanism (as first suggested by [71]), the mostly-filled notch produced by conservation of the first adiabatic invariant requires variations in the B-field that are large enough to explain its durability (larger than $\sim$2% turbulent fluctuations on a semi-weekly scale; [69, 70]) and small enough ($\lesssim$ 12%) to be credible, compared to jumps in |B| caused by observed shocks [23, 45]. In contrast, the empty notch model's narrow widths required an implausibly small change of |B| – 0.14% at most – which makes it difficult to explain how the anisotropy episodes persist for months at a time.

Kóta and Jokipii's theoretical model [3] was considered in light of the above findings from CRS analysis and observations. According to their model, the anisotropy may be produced by shocks that trap particles if their $\mu$ is less than the shock's critical angle, $\mu_c$ – informed by the magnitudes of local and compressed fields. Particles trapped in the downstream region lose energy over time in the adiabatically-expanding, weakening magnetic fields. Under these circumstances, particles with pitch angles closest to 90° experience the most cooling and contribute the most to the depletions observed in the intensity distribution.

Their results are consistent with a broad, shallow notch. In particular, their late-2012 shock simulation produced a 29° width (centered about 90°) in the affected pitch angle distribution. This is comparable to the 29° nominal width produced by Model #2 for the 2013-67 epoch. Further relating the notch model to their model, it seems reasonable to suggest that that the notch widths are proportional to field changes – produced by the ratio of the shock's expanded to compressed fields – and the depths are related to the amount of

time that the particles spend downstream in the cooling region. Magnitudes of the compressed field were estimated using Model #2's notch parameters (from HET 2's results) and local field measurements reported by MAG. The estimations were found to be reasonably consistent with observations: 1) the 2013-67 prediction yielded a field strength of $0.55 \pm 0.12$ nT, while the preceding 2012-335 forward shock had an observed value of $0.56 \pm 0.04$ nT [23]. 2) An estimated strength of $0.49 \pm 0.10$ nT was predicted for the 2015-208 epoch, compared to the preceding reverse shock's enhanced field of $0.49 \pm 0.04$ nT (on 2015-137) [45]. A trend of mostly constant width is evident and suggests that the magnetic field at the shock was relatively steady until it weakened to the local value toward the anisotropy's minima. A trend of steadily increasing depth may reflect the particles' constant cooling over time.

In conclusion, the current work supports that the GCR pitch angle anisotropy observed by Voyager 1 in the VLISM is the result of a broad, shallow, mostly-filled notch caused by particles that are missing near 90° in an otherwise uniform pitch angle distribution, and there are indications that shocks or compressions play a role in the anisotropy's formation (magnetic trapping) and temporal variation (cooling).

# Appendix A
# CRS Telescope Boresights

The purpose of this appendix is to document the process of acquiring telescope boresight pointing directions over time using a series of coordinate transformations in conjunction with the spacecraft's daily position vector reported by the Navigations team in Voyager's Science Experiment Data Record (SEDR).

## A.1 Clock and Cone Angles

Clock and cone angles on the Voyager spacecraft are described in Chapter 2, Subsection 2.4.1. Table A.1 lists cone and clock angles for the sun sensor, star tracker, and the spacecraft's $\hat{S}_x$, $\hat{S}_y$ and -$\hat{S}_z$ axes, and Table A.2 lists cone and clock angles for the 7 CRS telescopes, applicable for both Voyager 1 and Voyager 2.

| | **Sun Sensor** | **Star Tracker** | $\hat{S}_x$ | $\hat{S}_y$ | $-\hat{S}_z$ |
|---|---|---|---|---|---|
| **cone angle** | 0° | — | 90° | 90° | 0° |
| **clock angle** | — | 0° | 305° | 215° | 0° to 360° |

**Table A.1**. The $\hat{S}_x$, $\hat{S}_y$ and -$\hat{S}_z$ components of the spacecraft coordinate system defined in terms of cone and clock angles for Voyagers 1 & 2. -$\hat{S}_z$ is the axis from the center of the radio dish to Earth and is the same axis as the sun sensor's boresight vector.

| | **LET A & TET** (V1 & V2) | **LET B** (V1 & V2) | **LET C** (V1 & V2) | **LET D** (V1 & V2) | **HET 1A** (V1 Only) | **HET 2A** (V1 Only) | **HET 1A** (V2 Only) | **HET 2A** (V2 Only) |
|---|---|---|---|---|---|---|---|---|
| **cone angle** | 115° | 53° | 65° | 47.49° | 60° | 78° | 120° | 140° |
| **clock angle** | 305° | 236° | 125° | 9.69° | 338° | 104° | 158° | 104° |

**Table A.2**. Summary of clock and cone angles for CRS telescopes on Voyager 1 (V1) and Voyager 2 (V2).

## A.2 Telescope-to-Spacecraft Coordinate System Transformation

The LET A, LET B, and LET D telescope triad on CRS forms an orthogonal (left-handed) coordinate system, which can be used as a reference for the other telescopes. The rotation matrix used to convert a telescope's boresight vector in the A, B, D system ($S_A$, $S_B$, $S_D$) to the corresponding vector in spacecraft coordinates ($S_x$, $S_y$, $S_z$) is:

$$\begin{pmatrix} S_x \\ S_y \\ S_z \end{pmatrix} = \begin{pmatrix} 0.9031 & 0.2862 & 0.3202 \\ 0 & 0.7456 & -0.6664 \\ 0.4295 & -0.6018 & -0.6733 \end{pmatrix} \begin{pmatrix} S_A \\ S_B \\ S_C \end{pmatrix} \tag{A.1}$$

## A.3 Spacecraft-to-Solar-Ecliptic Coordinate System Transformation

Words 12 through 20 in the SEDR's Navigation pointing block contain a matrix for transforming any vector in spacecraft coordinates ($S_x$, $S_y$, $S_z$) to solar ecliptic coordinates ($E_x$, $E_y$, $E_z$). Thus, a telescope boresight vector from Equation A.1 is shifted to solar ecliptic via:

$$\begin{pmatrix} E_x \\ E_y \\ E_z \end{pmatrix} = \begin{pmatrix} P_{12} & P_{15} & P_{18} \\ P_{13} & P_{16} & P_{19} \\ P_{14} & P_{17} & P_{20} \end{pmatrix} \begin{pmatrix} S_x \\ S_y \\ S_z \end{pmatrix} \tag{A.2}$$

where the Navigation terms, ($P_{12}$ through $P_{20}$), reflect the values on a given day.

## A.4 Solar Ecliptic, Heliographic, and R, T, N Coordinate System Transformations

A procedure for converting telescope boresight vectors from solar ecliptic (Earth mean orbit, 1950; inertial) to heliographic (inertial) to R, T, N (spacecraft-

centered) coordinate systems is summarized below, based off of Voyager Memo No. 33 by A. J. Lazarus in 1978.

## A.1 Solar Ecliptic to Heliographic Coordinates

A vector in solar ecliptic coordinates, $\vec{E} = (E_x,\, E_y,\, E_z)$ (recall Equation A.2) can be rotated to heliographic intertial coordinates $(H_x,\, H_y,\, H_z)$ via:

$$\begin{pmatrix} H_x \\ H_y \\ H_z \end{pmatrix} = \begin{pmatrix} \cos\phi_s & \sin\phi_s & 0 \\ -\sin\phi_s\cos\theta_s & \cos\phi_s\cos\theta_s & \sin\theta_s \\ \sin\phi_s\sin\theta_s & -\cos\phi_s\sin\theta_s & \cos\theta_s \end{pmatrix} \begin{pmatrix} E_x \\ E_y \\ E_z \end{pmatrix} \tag{A.3}$$

where $\phi_s$ is the longitude of the ascending node of the solar equatorial plane in 1950: $\phi_s = 75.07°$ (Voyager's solar ecliptic coordinates are reported using Earth mean orbit, 1950), and $\theta_s$ is the tilt of the sun: $\theta_s = 7.25°$.

The above matrix is obtained by a two-step process. First, $\vec{E}$ is rotated about $\hat{z}_{SE}$ by $\phi_s$:

$$\begin{pmatrix} E_x^* \\ E_y^* \\ E_z^* \end{pmatrix} = \begin{pmatrix} \cos\phi_s & \sin\phi_s & 0 \\ -\sin\phi_s & \cos\phi_s & 0 \\ 0 & 0 & 1 \end{pmatrix} \begin{pmatrix} E_x \\ E_y \\ E_z \end{pmatrix}. \tag{A.4}$$

Second, the new vector $\vec{E}^*$ is rotated about the $\hat{x}^*_{SE}$-axis by $\theta_s$ (to align $\hat{z}_{SE}$ with the sun's z-axis):

$$\begin{pmatrix} H_x \\ H_y \\ H_z \end{pmatrix} = \begin{pmatrix} 1 & 0 & 0 \\ 0 & \cos\theta_s & \sin\theta_s \\ 0 & -\sin\theta_s & \cos\theta_s \end{pmatrix} \begin{pmatrix} E_x^* \\ E_y^* \\ E_z^* \end{pmatrix}. \tag{A.5}$$

## A.2 Heliographic to R, T, N Coordinates

Given a vector $\vec{H} = (H_x,\, H_y,\, H_z)$ in heliographic coordinates (e.g. Equation A.3), the transformation to (R, T, N) is performed in a two-step set of rotations about angles $\beta$ and $\theta$, which are defined as follows:

$$\beta = \tan^{-1}\left(\frac{H_y}{H_x}\right) \tag{A.6}$$

$$\theta = \tan^{-1}\left(\frac{H_z}{\sqrt{H_x^2 + H_y^2}}\right). \tag{A.7}$$

The first step is to rotate $\vec{H}$ about $\hat{z}_{HG}$ by the angle $\beta$:

$$\begin{pmatrix} H_x^* \\ H_y^* \\ H_z^* \end{pmatrix} = \begin{pmatrix} \cos\beta & \sin\beta & 0 \\ -\sin\beta & \cos\beta & 0 \\ 0 & 0 & 1 \end{pmatrix} \begin{pmatrix} H_x \\ H_y \\ H_z \end{pmatrix}. \tag{A.8}$$

The second step is to rotate $\vec{H}^*$ about $\hat{y}_{HG}^*$ by the angle $\theta$:

$$\begin{pmatrix} V_R \\ V_T \\ V_N \end{pmatrix} = \begin{pmatrix} \cos\theta & 0 & \sin\theta \\ 0 & 1 & 0 \\ -\sin\theta & 0 & \cos\theta \end{pmatrix} \begin{pmatrix} H_x^* \\ H_y^* \\ H_z^* \end{pmatrix}. \tag{A.9}$$

The result for transforming a vector from heliographic ($H_X$, $H_Y$, $H_Z$) to ($V_R$, $V_T$, $V_N$) is then:

$$\begin{pmatrix} V_R \\ V_T \\ V_N \end{pmatrix} = \begin{pmatrix} \cos\theta\cos\beta & \sin\beta\cos\theta & \sin\theta \\ -\sin\beta & \cos\beta & 0 \\ -\cos\beta\sin\theta & -\sin\theta\sin\beta & \cos\theta \end{pmatrix} \begin{pmatrix} H_x \\ H_y \\ H_z \end{pmatrix}. \tag{A.10}$$

## A.3 Sanity Check: Boresight Components in R, T, N and Solar Ecliptic Coordinates

Tables A.3 & A.4 include boresight components of HET 1 (A-end), HET 2 (A-end), and TET (same as LET A) telescopes to 7 decimal places in R, T, N and solar ecliptic on 2014, DOY 125 to serve as a sanity check when calculating the directions of CRS telescopes.

| | **R** | **T** | **N** |
|---|---|---|---|
| **HET 1A** | -0.4972945 | 0.2815072 | -0.8206413 |
| **HET 2A** | -0.2059683 | -0.9365612 | 0.2836022 |
| **TET** | 0.4295103 | 0.7139733 | -0.5529585 |
| | **$S_x$** | **$S_y$** | **$S_z$** |
| **HET 1A** | 0.1247837 | -0.1201258 | -0.9848853 |
| **HET 2A** | -0.7396914 | 0.6327442 | 0.2291100 |
| **TET** | -0.4033671 | -0.8675235 | -0.2910292 |

**Table A.3**. R, T, N and Sun-centered solar ecliptic ($S_x$, $S_y$, $S_z$) components of boresights to 7 decimal places for Voyager 1 HET 1A, HET 2A, and TET (= LET A) for 2014, DOY 125.

Occasionally, Voyager 1 rotates counterclockwise about the -$\hat{S}_z$ spacecraft axis[A.1] to a position that is offset by 70° in clock angle. These maneuvers are

[A.1]While -$\hat{S}_z$ is pointed towards Earth and not the Sun, it is nearly the same as -$\hat{R}$ in R, T,

detailed in Chapter 3 (Section 3.3), but it is useful to include the transformation equation here. Given the telescope's boresight vector in R, T, N, the 70°-offset rotation matrix is given by:

$$\begin{pmatrix} R_{70^\circ} \\ T_{70^\circ} \\ N_{70^\circ} \end{pmatrix} = \begin{pmatrix} 1 & 0 & 0 \\ 0 & \cos\theta & \sin\theta \\ 0 & -\sin\theta & \cos\theta \end{pmatrix} \begin{pmatrix} R \\ T \\ N \end{pmatrix} \tag{A.11}$$

where $\theta = 70^\circ$. The results from applying this rotation to Table A.3's boresight components are listed in Table A.4.

| | $\mathbf{R}_{70^\circ}$ | $\mathbf{T}_{70^\circ}$ | $\mathbf{N}_{70^\circ}$ |
|---|---|---|---|
| **HET 1A** | -0.4952326 | -0.6738916 | -0.5482837 |
| **HET 2A** | -0.2121083 | -0.0534302 | 0.9757846 |
| **TET** | 0.474377 | -0.2772655 | 0.8604773 |
| | $\mathbf{S}_x$ | $\mathbf{S}_y$ | $\mathbf{S}_z$ |
| **HET 1A** | -0.6813640 | 0.3493002 | -0.6432205 |
| **HET 2A** | 0.2889457 | 0.6788440 | 0.6750419 |
| **TET** | -0.6087252 | -0.6751517 | -0.4166824 |

**Table A.4**. Similar to Table A.3, but for when the spacecraft is in the 70°-offset orientation.

N at Voyager's large radial distance. Therefore, to first order, rotations about -$\hat{S}_z$ are performed counterclockwise in the N-T plane.

# Appendix B
# Data Analysis

## B.1 A Comparison of Sun-to-Spacecraft and Earth-to-Spacecraft Radial Vectors

The $\hat{R}$ sun-to-spacecraft vector in (R, T, N) differs from Voyager 1's earth-to-spacecraft vector, about which roll calibrations and 70°-offsets are performed. However, given that Voyager is beyond the heliopause (> 122 AU from the sun), the angular difference between the two vectors is small. At most:

$$\sin^{-1}\left(\frac{1 \text{ AU}}{122 \text{ AU}}\right) = 0.5^\circ, \tag{B.1}$$

so the simulated maneuvers are performed about $\hat{R}$.

## B.2 Monte Carlo Simulation Procedure

Detectors B1 and C1 have radii of 1.596 and 1.739 cm respectively, and a spacing of $l = 9.094$ cm (measured from the top of one detector to the bottom of the other)[B.1]. Knowing these geometries, one can use a Monte Carlo to numerically simulate particles passing through HET 1 and HET 2 as follows (all in the telescope coordinate system unless otherwise noted):

1. Generate a particle on the first detector at location uniformly randomly distributed in $x_1$, $y_1$.

[B.1] The B detectors are curved, thin detectors. In the Monte Carlo simulation, B1 is modeled as flat and its spacing is defined relative to the bottom of its curvature. Although the curvature alters the path length of the particles and can affect their total energy loss, this has negligible affects on the integrated rates. Moreover, treating B1 as flat does not significantly alter the telescope's field of view.

2. Generate a random direction for the particle using a $\cos^2(\theta)$ distribution.

3. Use these values to calculate the projected points in $x$ and $y$ when a particle travels a distance $L$ in $\hat{z}$.

4. Keep only the projected points which pass through both detectors. Label these particle coordinates – defined with respect to the top detector – as $(p_x, p_y, p_z)$.

5. Convert particle coordinates to R, T, N coordinates: $(p_x, p_y, p_z) \rightarrow (p_r, p_t, p_n)$.

6. Calculate pitch angle by taking the dot product between the particle's coordinates and the B-field direction (in R, T, N).

7. For a given magnetic field direction and telescope viewing direction (different orientations for HET 1 and HET 2, for example), output information about the telescope orientation (clock angle, $\theta$) and particle pitch angles ($\alpha$)

8. Simulate a magrol by rotating the spacecraft about $\hat{R}$ in small clock angle increments over 360° (in R, T, N) and repeat steps 1-7 to accumulate the desired number of particles.

9. Simulate 70°-offset data by fixing clock angle at 70° – roughly a 70°-offset rotation about $\hat{R}$ (in R, T, N) – and repeat steps 1-7 to accumulate the desired number of particles.

# Appendix C
# Additional Forms of Anisotropy

The 7 prominent roll maneuver epochs described in Chapter 3, Section 3.2 and used in Figure 3.5 are: 1) 2013-71, 2) 2013-122, 3) 2015-219, 4) 2015-252, 5) 2015-257, 6) 2015-310, and 7) 2016-65.

Results of searches for possible additional forms of anisotropy are summarized in this appendix (described in Chapter 3, Section 3.5). Tables C.1 & C.2 lists parameters obtained from Compton-Getting fits to PENH rates ($\gtrsim$ 70 MeV; proton-dominated) during HET 1 and HET 2 roll maneuvers – with pitch-angle anisotropy effects excluded – from late 2012 through the end of 2016 (25 epochs).

| **Epoch** | $I_0$ **(cts/sec)** | $\delta$ | $\theta_0$ | **# Points** | $\chi^2$ |
|---|---|---|---|---|---|
| **2012-263** | 2.60 ± 0.02 | 0.022 ± 0.017 | 233.3° ± 41.0° | 145 | 133.1 |
| **2012-307** | 2.57 ± 0.02 | -0.006 ± 0.017 | 188.0° ± 182.5° | 157 | 176.1 |
| **2013-31** | 2.55 ± 0.02 | -0.019 ± 0.018 | 190.6° ± 43.5° | 155 | 148.9 |
| **2013-71** | 2.55 ± 0.02 | -0.009 ± 0.018 | 33.7° ± 108.0° | 151 | 147.0 |
| **2013-122** | 2.58 ± 0.02 | 0.021 ± 0.016 | 64.4° ± 45.6° | 150 | 144.9 |
| **2013-214** | 2.56 ± 0.02 | 0.017 ± 0.014 | 90.6° ± 58.9° | 155 | 146.2 |
| **2013-261** | 2.55 ± 0.02 | 0.005 ± 0.014 | 271.3° ± 182.5° | 152 | 189.5 |
| **2013-305** | 2.61 ± 0.03 | -0.005 ± 0.023 | 172.1° ± 182.5° | 81 | 88.1 |
| **2014-30** | 2.54 ± 0.02 | 0.016 ± 0.017 | 41.1° ± 51.5° | 157 | 137.5 |
| **2014-69** | 2.55 ± 0.02 | 0.009 ± 0.018 | 39.7° ± 102.8° | 148 | 137.7 |
| **2014-121** | 2.61 ± 0.02 | -0.005 ± 0.015 | 160.5° ± 182.5° | 155 | 152.1 |
| **2014-213** | 2.59 ± 0.02 | 0.016 ± 0.018 | 190.7° ± 58.2° | 139 | 140.7 |
| **2014-260** | 2.59 ± 0.02 | 0.025 ± 0.019 | 314.2° ± 55.3° | 83 | 56.5 |
| **2014-304** | 2.55 ± 0.02 | -0.013 ± 0.017 | 159.8° ± 87.4° | 126 | 154.3 |
| **2015-36** | 2.57 ± 0.02 | 0.017 ± 0.016 | 53.1° ± 53.0° | 156 | 157.2 |
| **2015-127** | 2.56 ± 0.02 | -0.003 ± 0.018 | 199.0° ± 182.5° | 158 | 127.4 |
| **2015-219** | 2.55 ± 0.02 | -0.012 ± 0.017 | 2.2° ± 39.0° | 157 | 173.9 |
| **2015-252** | 2.59 ± 0.02 | -0.015 ± 0.019 | 26.1° ± 43.8° | 153 | 173.5 |
| **2015-257** | 2.56 ± 0.02 | -0.024 ± 0.018 | 200.8° ± 34.3° | 156 | 171.9 |
| **2015-310** | 2.56 ± 0.02 | -0.009 ± 0.017 | 240.2° ± 113.0° | 139 | 139.1 |
| **2016-35** | 2.56 ± 0.02 | 0.023 ± 0.018 | 139.2° ± 57.0° | 93 | 88.8 |
| **2016-84** | 2.59 ± 0.02 | 0.010 ± 0.015 | 66.6° ± 100.2° | 158 | 154.8 |
| **2016-126** | 2.55 ± 0.02 | 0.014 ± 0.015 | 84.0° ± 77.9° | 139 | 135.3 |
| **2016-218** | 2.58 ± 0.02 | 0.008 ± 0.016 | 156.6° ± 133.8° | 150 | 153.7 |
| **2016-309** | 2.57 ± 0.02 | 0.011 ± 0.014 | 147.0° ± 86.7° | 159 | 175.3 |

**Table C.1**. Compton-Getting parameters for 25 HET 1 roll maneuver epochs. Results were obtained by fitting the function $I = I_0(1+\delta\cos(\theta-\theta_0))$ to bi-directional PENH rates (48-s data; >70 MeV; mostly protons) vs. telescope boresight clock angle during roll maneuvers, per [5]. $I$ is the count rate, $I_0$ is the mean rate excluding the pitch-angle anisotropy, $\delta$ is the anisotropy amplitude, $\theta$ is the telescope boresight clock angle, and $\theta_0$ is the boresight clock angle at which maximum intensity occurs. The weighted average of the amplitudes for all 25 epochs is $\delta = 0.005 \pm 0.003$. Anisotropy amplitudes are plotted vs. time in Figure 3.10a.

| **Epoch** | $I_0$ **(cts/sec)** | $\delta$ | $\theta_0$ | **# Points** | $\chi^2$ |
|---|---|---|---|---|---|
| **2012-263** | 2.80 ± 0.02 | -0.008 ± 0.016 | 157.3° ± 146.8° | 145 | 129.4 |
| **2012-307** | 2.82 ± 0.02 | 0.018 ± 0.015 | 158.5° ± 51.1° | 157 | 143.8 |
| **2013-31** | 2.81 ± 0.02 | 0.016 ± 0.017 | 179.1° ± 54.6° | 155 | 141.5 |
| **2013-71** | 2.84 ± 0.02 | 0.006 ± 0.015 | 72.1° ± 182.5° | 151 | 150.3 |
| **2013-122** | 2.82 ± 0.02 | 0.009 ± 0.014 | 144.0° ± 103.7° | 150 | 149.6 |
| **2013-214** | 2.83 ± 0.02 | 0.000 ± 0.016 | 175.8° ± 182.5° | 155 | 134.9 |
| **2013-261** | 2.81 ± 0.02 | -0.013 ± 0.018 | 20.4° ± 43.5° | 152 | 145.9 |
| **2013-305** | 2.83 ± 0.03 | 0.012 ± 0.018 | 301.1° ± 85.7° | 81 | 74.2 |
| **2014-30** | 2.80 ± 0.02 | 0.013 ± 0.013 | 293.5° ± 68.5° | 157 | 179.9 |
| **2014-69** | 2.82 ± 0.02 | 0.003 ± 0.014 | 156.1° ± 182.5° | 148 | 132.5 |
| **2014-121** | 2.89 ± 0.02 | -0.012 ± 0.017 | 200.0° ± 71.8° | 155 | 146.5 |
| **2014-213** | 2.85 ± 0.02 | 0.013 ± 0.014 | 272.0° ± 76.2° | 139 | 116.7 |
| **2014-260** | 2.84 ± 0.02 | -0.033 ± 0.027 | 195.0° ± 31.3° | 83 | 77.2 |
| **2014-304** | 2.81 ± 0.02 | 0.011 ± 0.015 | 95.3° ± 92.5° | 126 | 120.2 |
| **2015-36** | 2.83 ± 0.02 | -0.012 ± 0.017 | 191.1° ± 75.6° | 156 | 119.4 |
| **2015-127** | 2.85 ± 0.02 | 0.011 ± 0.013 | 298.4° ± 77.0° | 158 | 181.5 |
| **2015-219** | 2.79 ± 0.02 | 0.020 ± 0.017 | 45.3° ± 39.1° | 157 | 126.3 |
| **2015-252** | 2.84 ± 0.02 | 0.021 ± 0.017 | 183.7° ± 37.5° | 153 | 167.0 |
| **2015-257** | 2.81 ± 0.02 | 0.015 ± 0.014 | 75.0° ± 62.3° | 156 | 161.8 |
| **2015-310** | 2.83 ± 0.02 | -0.003 ± 0.019 | 227.5° ± 182.5° | 139 | 155.5 |
| **2016-35** | 2.78 ± 0.02 | -0.008 ± 0.017 | 128.8° ± 205.0° | 93 | 89.9 |
| **2016-84** | 2.82 ± 0.02 | -0.010 ± 0.016 | 226.8° ± 101.7° | 158 | 195.7 |
| **2016-126** | 2.77 ± 0.02 | 0.009 ± 0.014 | 285.2° ± 92.3° | 139 | 144.0 |
| **2016-218** | 2.81 ± 0.02 | 0.019 ± 0.016 | 58.8° ± 44.1° | 150 | 163.5 |
| **2016-309** | 2.79 ± 0.02 | 0.010 ± 0.015 | 162.3° ± 104.1° | 159 | 158.7 |

**Table C.2**. Similar to Table C.1, but for HET 2. The weighted average of the amplitudes for all 25 epochs is $\delta = 0.006 \pm 0.003$. Anisotropy amplitudes are plotted vs. time in Figure 3.10b.

# Appendix D
# Model #1 Results: Empty Notch

This section summarizes HET 1 and HET 2 roll-maneuver fits with a figure, and in tabular form. Figure D.1 shows an example of the $\chi^2$ values produced by fits of the simulated roll maneuver response function to observations in order to determine an effective notch width and its uncertainties. Tables D.1 & D.2 contain the information used in Figures 5.1, 5.2, & 5.3.

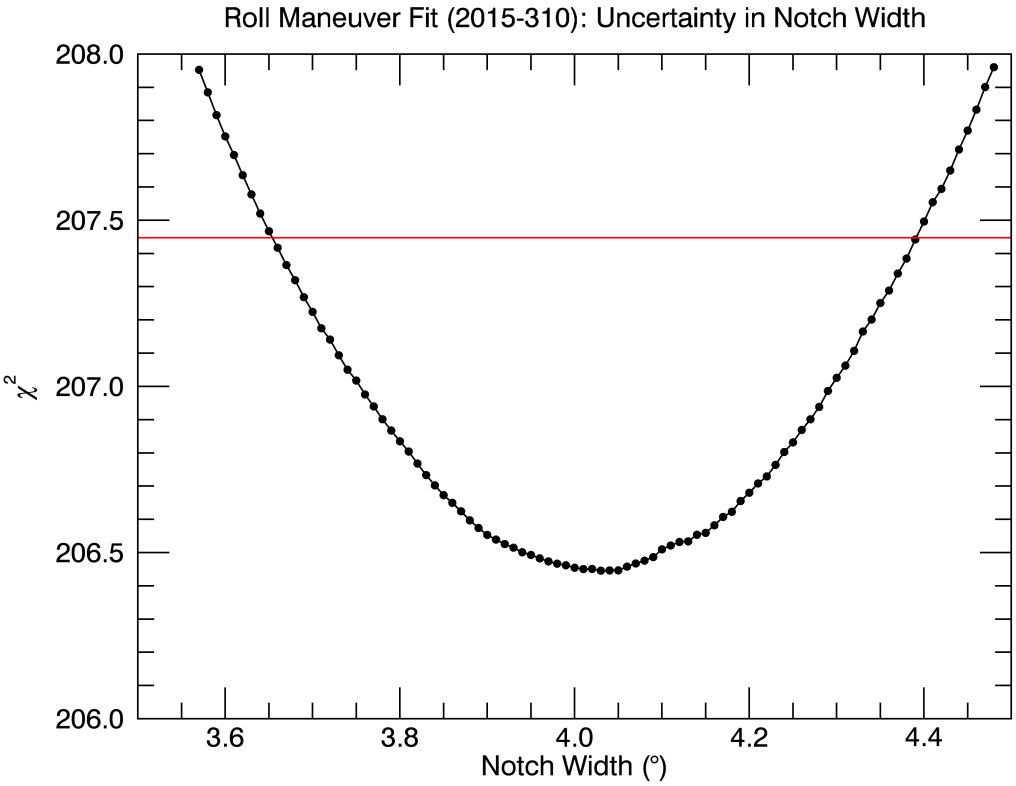


**Figure D.1**. $\chi^2$ vs. effective notch width parabola for roll maneuver response function fits to HET 1 PENH bi-directional ($\gtrsim$ 70 MeV; mostly protons) observations during the 2015-310 epoch. The effective notch width at the $\chi^2$ minimum was 4.0°. The horizontal line (red) indicates the $\chi^2$ + 1 value, which, for this epoch, signifies uncertainties of ±0.4° in the width. There were 185 observation points used in this fit.

| Roll Maneuver Epoch | Effective Notch Width | 70°-offset Predictions (HET 1 PENH) | 70°-offset Observations (HET 1 PENH) | Omnidirectional Predictions (HET 1 Guards) | Omnidirectional Observations (HET 1 Guards) |
|---|---|---|---|---|---|
| **2012-263** | 2.5°± 0.4° | 0.991 ± 0.002 | NA | 0.978 ± 0.003 | 0.995 ± 0.002 |
| **2012-307** | 2.6°± 0.5° | 0.959 ± 0.007 | 0.973 ± 0.004 | 0.977 ± 0.004 | 0.989 ± 0.005 |
| **2013-31** | 1.1°± 0.4° | 0.986 ± 0.005 | NA | 0.990 ± 0.003 | 0.995 ± 0.001 |
| **2013-71** | 2.0°± 0.4° | 0.963 ± 0.007 | 0.957 ± 0.004 | 0.982 ± 0.003 | 0.984 ± 0.001 |
| **2013-122** | 3.7°± 0.4° | 0.925 ± 0.008 | 0.939 ± 0.004 | 0.967 ± 0.003 | 0.976 ± 0.001 |
| **2013-214** | 0.9°± 0.4° | 0.983 ± 0.008 | 0.991 ± 0.004 | 0.992 ± 0.003 | 0.996 ± 0.001 |
| **2013-261** | 0.1°± 0.3° | 0.997 ± 0.006 | NA | 0.999 ± 0.002 | 1.001 ± 0.001 |
| **2013-305** | 0.4°± 0.5° | 0.992 ± 0.008 | 0.994 ± 0.004 | 0.996 ± 0.004 | 0.999 ± 0.001 |
| **2014-30** | 0.3°± 0.4° | 0.995 ± 0.006 | 0.994 ± 0.004 | 0.998 ± 0.003 | 0.998 ± 0.001 |
| **2014-69** | 0.3°± 0.4° | 0.992 ± 0.009 | NA | 0.997 ± 0.003 | 0.995 ± 0.001 |
| **2014-121** | 1.2°± 0.4° | 0.976 ± 0.008 | 0.989 ± 0.004 | 0.989 ± 0.003 | 1.006 ± 0.001 |
| **2014-213** | 1.6°± 0.4° | 0.959 ± 0.010 | NA | 0.986 ± 0.003 | 0.993 ± 0.001 |
| **2014-260** | 0.2°± 0.3° | 0.997 ± 0.004 | 1.012 ± 0.004 | 0.998 ± 0.002 | 0.998 ± 0.001 |
| **2014-304** | 0.8°± 0.5° | 0.987 ± 0.009 | 1.007 ± 0.005 | 0.993 ± 0.004 | 0.994 ± 0.001 |
| **2015-36** | 0.9°± 0.5° | 0.990 ± 0.006 | 0.994 ± 0.004 | 0.993 ± 0.004 | 0.991 ± 0.001 |
| **2015-127** | 1.1°± 0.5° | 0.991 ± 0.004 | 0.980 ± 0.004 | 0.990 ± 0.004 | 0.980 ± 0.001 |
| **2015-219** | 2.5°± 0.4° | 0.956 ± 0.007 | 0.929 ± 0.004 | 0.978 ± 0.003 | 0.977 ± 0.001 |
| **2015-252** | 3.4°± 0.4° | 0.945 ± 0.007 | 0.928 ± 0.006 | 0.970 ± 0.003 | 0.975 ± 0.001 |
| **2015-257** | 2.6°± 0.4° | 0.950 ± 0.008 | 0.928 ± 0.006 | 0.977 ± 0.003 | 0.969 ± 0.001 |
| **2015-310** | 4.0°± 0.4° | 0.878 ± 0.012 | 0.890 ± 0.003 | 0.965 ± 0.003 | 0.967 ± 0.001 |
| **2016-35** | 3.8°± 0.6° | 0.909 ± 0.013 | 0.886 ± 0.004 | 0.967 ± 0.005 | 0.981 ± 0.001 |
| **2016-84** | 2.3°± 0.5° | 0.960 ± 0.008 | NA | 0.980 ± 0.004 | 0.986 ± 0.001 |
| **2016-126** | 1.8°± 0.5° | 0.996 ± 0.001 | 0.967 ± 0.004 | 0.985 ± 0.004 | 0.985 ± 0.001 |
| **2016-218** | 1.6°± 0.4° | 0.995 ± 0.001 | 0.951 ± 0.004 | 0.986 ± 0.003 | 0.989 ± 0.001 |
| **2016-309** | 0.7°± 0.4° | 0.998 ± 0.001 | 0.982 ± 0.009 | 0.994 ± 0.003 | 0.989 ± 0.001 |

**Table D.1**. A summary of effective notch widths (obtained from bi-directional roll maneuver fits to PENH rates; $\gtrsim$ 70 MeV, proton-dominated) and corresponding relative intensity changes arising from the particle pitch-angle anisotropy for predicted and observed 70°-offset and omnidirectional observations for HET 1. Predicted intensities are normalized to values obtained from notch-free simulated response functions. Observed 70°-offset intensities are normalized to temporally-adjacent non-offset rates and omnidirectional observations are normalized to the average values during the 2013.6 to 2014.1 time period when count rates are relatively uniform and isotropic. Data are plotted in Figure 5.1.

| Roll Maneuver Epoch | Effective Notch Width | 70°-offset Predictions (HET 2 PENH) | 70°-offset Observations (HET 2 PENH) | Omnidirectional Predictions (HET 2 Guards) | Omnidirectional Observations (HET 2 Guards) | HET 1 & 2 Avg. Notch Width |
|---|---|---|---|---|---|---|
| **2012-263** | 1.3°± 0.5° | 0.993 ± 0.003 | NA | 0.989 ± 0.004 | 0.993 ± 0.002 | 2.0°± 0.3° |
| **2012-307** | 2.4°± 0.4° | 0.985 ± 0.003 | 0.989 ± 0.003 | 0.979 ± 0.004 | 0.983 ± 0.005 | 2.5°± 0.3° |
| **2013-31** | 1.6°± 0.5° | 0.999 ± 0.000 | NA | 0.986 ± 0.004 | 0.991 ± 0.002 | 1.3°± 0.3° |
| **2013-71** | 3.0°± 0.4° | 1.000 ± 0.000 | 0.987 ± 0.004 | 0.974 ± 0.004 | 0.982 ± 0.001 | 2.5°± 0.3° |
| **2013-122** | 3.6°± 0.4° | 1.000 ± 0.000 | 0.984 ± 0.004 | 0.968 ± 0.004 | 0.973 ± 0.001 | 3.7°± 0.3° |
| **2013-214** | 1.4°± 0.4° | 1.000 ± 0.000 | 0.999 ± 0.004 | 0.988 ± 0.004 | 0.996 ± 0.001 | 1.1°± 0.3° |
| **2013-261** | 0.0°± 0.3° | 1.000 ± 0.000 | NA | 1.000 ± 0.002 | 1.001 ± 0.001 | 0.1°± 0.2° |
| **2013-305** | 1.0°± 0.7° | 1.000 ± 0.000 | 0.996 ± 0.004 | 0.991 ± 0.006 | 1.000 ± 0.001 | 0.6°± 0.4° |
| **2014-30** | 0.5°± 0.4° | 1.000 ± 0.000 | 0.995 ± 0.004 | 0.996 ± 0.004 | 0.998 ± 0.001 | 0.4°± 0.3° |
| **2014-69** | 1.4°± 0.5° | 1.000 ± 0.000 | NA | 0.988 ± 0.004 | 0.995 ± 0.001 | 0.7°± 0.3° |
| **2014-121** | 1.6°± 0.4° | 1.000 ± 0.000 | 1.014 ± 0.004 | 0.986 ± 0.004 | 1.007 ± 0.001 | 1.4°± 0.3° |
| **2014-213** | 0.8°± 0.6° | 0.998 ± 0.001 | NA | 0.993 ± 0.005 | 0.992 ± 0.001 | 1.4°± 0.3° |
| **2014-260** | 0.1°± 0.3° | 1.000 ± 0.000 | 0.998 ± 0.004 | 0.999 ± 0.002 | 1.001 ± 0.001 | 0.2°± 0.2° |
| **2014-304** | 0.3°± 0.5° | 1.000 ± 0.000 | 1.000 ± 0.005 | 0.997 ± 0.004 | 0.997 ± 0.001 | 0.5°± 0.4° |
| **2015-36** | 0.7°± 0.4° | 1.000 ± 0.000 | 1.001 ± 0.004 | 0.994 ± 0.004 | 0.995 ± 0.001 | 0.8°± 0.3° |
| **2015-127** | 1.4°± 0.4° | 1.000 ± 0.000 | 0.999 ± 0.004 | 0.987 ± 0.004 | 0.990 ± 0.001 | 1.3°± 0.3° |
| **2015-219** | 2.5°± 0.4° | 1.000 ± 0.000 | 0.990 ± 0.003 | 0.978 ± 0.004 | 0.980 ± 0.001 | 2.5°± 0.3° |
| **2015-252** | 3.1°± 0.5° | 1.000 ± 0.000 | 0.985 ± 0.006 | 0.973 ± 0.004 | 0.976 ± 0.001 | 3.3°± 0.3° |
| **2015-257** | 2.8°± 0.4° | 1.000 ± 0.000 | 0.985 ± 0.006 | 0.976 ± 0.004 | 0.976 ± 0.001 | 2.7°± 0.3° |
| **2015-310** | 3.0°± 0.4° | 1.000 ± 0.000 | 0.983 ± 0.004 | 0.974 ± 0.004 | 0.970 ± 0.002 | 3.5°± 0.3° |
| **2016-35** | 3.9°± 0.7° | 1.000 ± 0.000 | 0.990 ± 0.004 | 0.966 ± 0.006 | 0.970 ± 0.001 | 3.8°± 0.4° |
| **2016-84** | 2.0°± 0.5° | 1.000 ± 0.000 | NA | 0.983 ± 0.004 | 0.982 ± 0.001 | 2.1°± 0.3° |
| **2016-126** | 0.9°± 0.6° | 1.000 ± 0.000 | 0.998 ± 0.004 | 0.992 ± 0.005 | 0.987 ± 0.001 | 1.4°± 0.4° |
| **2016-218** | 1.7°± 0.5° | 1.000 ± 0.000 | 0.999 ± 0.004 | 0.986 ± 0.004 | 0.981 ± 0.001 | 1.6°± 0.3° |
| **2016-309** | 0.0°± 0.3° | 1.000 ± 0.000 | 1.011 ± 0.008 | 1.000 ± 0.002 | 0.987 ± 0.001 | 0.2°± 0.2° |

**Table D.2**. Similar to Table D.1, but for HET 2 (plotted in Figure 5.2). The last column lists the average of the HET 1 & HET 2 notch widths obtained by independent roll maneuver fits, weighted by uncertainties (plotted in Figure 5.3).

# Appendix E
# Model #2 Results: Partially-Filled Notch

Table E.1 compares empty and partially-filled notches applied to 70°-offset intensity reductions. Table E.2 lists the notch results from the intersection of HET 1 & 2 70°-offset response functions. Tables E.3 & E.4 list the notch parameters obtained using 70°-offset and omnidirectional response function curves for HET 1 and HET 2, respectively. Tables E.5 & E.6 list the fit results for independently calculated roll maneuvers for HET 1 and HET 2, allowing for notches of variable width and depth.

| **Width** | **Depth** | **HET 1 70°-offset Prediction** | **HET 1 70°-offset Observation** | **HET 2 70°-offset Prediction** | **HET 2 70°-offset Observation** |
|---|---|---|---|---|---|
| $4.0° \pm 0.4°$ | 100% | 12.2% ± 0.12% | 11.0% ± 0.3% | 0.0% ± 0.0% | 1.7% ± 0.4% |
| $19.1° \pm 0.8°$ | 100% | 56.2% ± 2.2% | 11.0% ± 0.3% | 1.7% ± 0.4 | 1.7% ± 0.4% |
| 30.2° | 13.5% | 11.0% | 11.0% ± 0.3% | 1.7% | 1.7% ± 0.4% |

**Table E.1**. Comparison of 70°-offset predictions and observations for empty and partially-filled notch scenarios using the 2015-296 offset epoch (2015-310 roll epoch). The width and depth chosen for the partially-filled notch is one possible combination that achieves consistency between predictions and observations for HET 1 and HET 2 simultaneously.

| | Epoch | 2013-67 | 2013-120 | 2015-208 | 2015-250 | 2015-296 | 2016-31 |
|---|---|---|---|---|---|---|---|
| **Width** | Nominal = | 29.1° | 25.8° | 31.0° | 33.5° | 30.2° | 25.4° |
| | Upper = | 32.1° | 28.1° | 33.8° | 37.0° | 32.0° | 28.0° |
| | Lower = | 25.2° | 22.8° | 27.6° | 28.8° | 28.4° | 22.1° |
| **Depth** | Nominal = | 6.5% | 10.0% | 10.0% | 9.7% | 13.5% | 17.6% |
| | Lower = | 6.4% | 9.7% | 9.6% | 9.5% | 13.4% | 16.5% |
| | Upper = | 6.9% | 10.8% | 10.8% | 10.4% | 13.6% | 19.6% |
| **Omnidirectional Intensity Reduction** | Predicted = | 1.6% ± 0.1% | 2.2% ± 0.1% | 2.7% ± 0.1% | 2.8% ± 0.2% | 3.5% ± 0.2% | 3.9% ± 0.1% |
| | Observed (H1) = | 1.6% ± 0.05% | 2.4% ± 0.05% | 1.9% ± 0.05% | 2.2% ± 0.07% | 2.9% ± 0.04% | 3.1% ± 0.06% |
| | Observed (H2) = | 1.8% ± 0.05% | 2.7% ± 0.05% | 2.1% ± 0.05% | 2.4% ± 0.07% | 3.1% ± 0.05% | 3.3% ± 0.06% |

**Table E.2**. Range of widths and depths from the intersection of HET 1 & 2 70°-offset response function curves, detailed in Chapter 4 (Subsection 4.5.2) and Chapter 5 (Subsection 5.3.1). Omnidirectional intensity reductions are predicted using Equation 4.5.1 and compared to observations. Quantities listed here are shown in Figures 5.4 & 5.5.

| **HET 1: Epoch** | **Range of Widths** | **Range of Depths** |
|---|---|---|
| **2013-67** | 2.1° to > 45° | 100% to < 4.1% |
| **2013-120** | 2.8° to > 45° | 100% to < 6.5% |
| **2015-208** | 11.1° to 26.5° | 18.6% to 8.3% |
| **2015-250** | 2.4° to 33.7° | 100% to 7.7% |
| **2015-296** | 3.3° to 20.6° | 100% to 16.5% |
| **2016-31** | 13.5° to 25.0° | 26.0% to 14.6% |

**Table E.3**. HET 1 range of widths and depths from intersection of omnidirectional and 70°-offset response function curves for the 6 epochs where the anisotropy is most prominent. The simulations incorporated values listed in Table 4.1 (Subsection 4.4.2) and pitch angles determined by the illustrative B-fields in Table 5.1 (Subsection 5.3.3). These results are plotted in Figures 5.10 & 5.12.

| **HET 2: Epoch** | **Nominal Width** | **Lower Limit** | **Upper Limit** | **Nominal Depth** | **Upper Limit** | **Lower Limit** |
|---|---|---|---|---|---|---|
| **2013-67** | 29.2° | 24.2° | 34.3° | 7.0% | 8.6% | 5.8% |
| **2013-120** | 22.5° | 19.2° | 25.8° | 13.7% | 16.4% | 11.8% |
| **2015-208** | 28.1° | 23.6° | 32.2° | 8.7% | 10.6% | 7.4% |
| **2015-250** | 20.4° | 14.4° | 26.2° | 13.4% | 19.5% | 10.2% |
| **2015-296** | 18.1° | 15.4° | 20.8° | 19.8% | 23.6% | 17.0% |
| **2016-31** | 14.3° | 10.5° | 17.6° | 26.3% | 36.2% | 20.9% |

**Table E.4**. HET 2 nominal widths and depths (with ranges) from intersection of omnidirectional and 70°-offset response function curves assuming a rectangular notch with variable width and depth as in Table E.4. These results are used in Figures 5.10 & 5.12.

| **HET 1: Epoch** | **Nominal Width** | **Lower Limit** | **Upper Limit** | **Nominal Depth** | **Upper Limit** | **Lower Limit** | **P-Value of $\chi^2$ Fit** |
|---|---|---|---|---|---|---|---|
| **2013-67** | 26.8° | 19.0° | 35.9° | 9.4% | 12.4% | 6.4% | 62.5% |
| **2013-120** | 25.8° | 23.2° | 33.4° | 18.5% | 21.5% | 15.5% | 48.7% |
| **2015-208** | 28.8° | 22.5° | 34.9° | 12.3% | 16.3% | 9.3% | 94.9% |
| **2015-250** | 25.7° | 21.2° | 30.7° | 15.8% | 18.8% | 12.8% | 58.5% |
| **2015-296** | 20.8° | 17.9° | 25.0° | 22.4% | 27.4% | 18.4% | 18.5% |
| **2016-31** | 13.4° | 10.6° | 16.4° | 29.5% | 36.5% | 23.5% | 21.8% |

**Table E.5**. HET 1 roll maneuver fits for notches of variable width and depth for the 6 epochs of Model #2. Results are plotted in Figures 5.11 & 5.12.

| **HET 2: Epoch** | **Nominal Width** | **Lower Limit** | **Upper Limit** | **Nominal Depth** | **Upper Limit** | **Lower Limit** | **P-Value of $\chi^2$ Fit** |
|---|---|---|---|---|---|---|---|
| **2013-67** | 34.3° | 29.1° | 42.3° | 12.6% | 16.6% | 9.6% | 56.6% |
| **2013-120** | 24.6° | 20.3° | 29.2° | 18.0% | 21.0% | 15.0% | 70.0% |
| **2015-208** | 17.6° | 13.2° | 22.6° | 15.1% | 19.1% | 11.1% | 14.0% |
| **2015-250** | 10.6° | 8.4° | 13.1° | 28.9% | 34.9% | 22.9% | 0.50% |
| **2015-296** | 20.8° | 17.1° | 28.8° | 16.1% | 19.1% | 13.1% | 30.9% |
| **2016-31** | 15.2° | 11.7° | 18.9° | 26.6% | 33.6% | 20.6% | 70.7% |

**Table E.6**. Similar to Table E.5, but for HET 2. Results are plotted in Figure 5.11.

# Appendix F
# 70°-offset Observations

This section summarizes HET 1 70°-offset observations in tabular form. Table F.1 lists values used in Figure 5.13.

| Start of 70°-Offset Epoch | 70° -Offset Maneuver Days | HET 1 PENH Bi-directional Protons | TET TAN Unidirectional Electrons | HET 1 BSp Unidirectional Protons | HET 1 BSe Unidirectional Electrons |
|---|---|---|---|---|---|
| **2012-305** | 305, 306, 309, 311, 315, 317, 321, 322, 323, 324 | 0.973 ± 0.004 | 0.986 ± 0.007 | 0.982 ± 0.011 | 0.995 ± 0.015 |
| **2013-67** | 67, 68, 69, 70, 71 | 0.957 ± 0.004 | 0.988 ± 0.008 | 0.972 ± 0.013 | 0.969 ± 0.018 |
| **2013-120** | 120, 121, 122 | 0.939 ± 0.004 | 0.980 ± 0.008 | 0.949 ± 0.012 | 0.995 ± 0.018 |
| **2013-217** | 217, 218, 219, 224 | 0.991 ± 0.004 | 0.975 ± 0.008 | 0.981 ± 0.011 | 0.983 ± 0.017 |
| **2013-307** | 307, 309, 311, 312, 314, 315 | 0.994 ± 0.004 | 0.982 ± 0.008 | 0.981 ± 0.012 | 1.002 ± 0.018 |
| **2014-35** | 35, 36, 40, 41, 42 | 0.994 ± 0.004 | 0.983 ± 0.008 | 0.970 ± 0.012 | 0.976 ± 0.017 |
| **2014-126** | 126, 127, 132, 133 | 0.989 ± 0.004 | 0.960 ± 0.007 | 1.003 ± 0.011 | 1.030 ± 0.017 |
| **2014-251** | 251, 252, 253, 254, 255, 258, 259 | 1.012 ± 0.004 | 0.994 ± 0.008 | 0.997 ± 0.012 | 1.028 ± 0.018 |
| **2014-302** | 302, 307, 308, 309, 310 | 1.007 ± 0.005 | 1.001 ± 0.009 | 0.983 ± 0.014 | 1.004 ± 0.020 |
| **2014-314** | 314, 322, 324 | 0.996 ± 0.006 | 0.981 ± 0.011 | 1.013 ± 0.017 | 0.999 ± 0.024 |
| **2015-27** | 27, 28, 29, 33, 35 | 0.994 ± 0.004 | 0.994 ± 0.009 | 1.002 ± 0.013 | 1.032 ± 0.018 |
| **2015-121** | 121, 123, 124, 125, 126 | 0.980 ± 0.004 | 0.992 ± 0.007 | 0.971 ± 0.011 | 1.007 ± 0.016 |
| **2015-208** | 208, 209, 210, 215, 216 | 0.929 ± 0.004 | 0.977 ± 0.007 | 0.956 ± 0.010 | 0.997 ± 0.015 |
| **2015-250** | 250, 251 | 0.928 ± 0.006 | 0.982 ± 0.012 | 0.941 ± 0.018 | 1.006 ± 0.027 |
| **2015-296** | 296, 297, 298, 300, 302, 307, 312 | 0.890 ± 0.003 | 0.986 ± 0.007 | 0.903 ± 0.010 | 1.026 ± 0.017 |
| **2016-31** | 31, 32, 34, 38, 39, 40 | 0.886 ± 0.004 | 0.980 ± 0.008 | 0.931 ± 0.011 | 1.013 ± 0.017 |
| **2016-124** | 124, 125, 129, 130, 131 | 0.967 ± 0.004 | 1.012 ± 0.010 | 0.939 ± 0.012 | 1.019 ± 0.019 |
| **2016-207** | 207, 209, 210, 213, 214, 217 | 0.951 ± 0.004 | 0.999 ± 0.007 | 0.963 ± 0.012 | 1.012 ± 0.019 |
| **2016-306** | 306, 308 | 0.982 ± 0.009 | 1.006 ± 0.013 | 0.932 ± 0.021 | 0.980 ± 0.036 |

**Table F.1**. A summary of bi-directional and unidirectional 70°-offset observations for HET 1 protons (PENH, BSp) and electrons (BSe) and TET electrons (TAN). Intensities for each epoch are reported relative to temporally-adjacent non-offset measurements.

# Appendix G
# Discussion Notes

## G.1 GCR Scattering Calculation

The diffusion coefficient has been constrained by observations to be:

$$\kappa_{||} \approx 10^{28} \text{ cm}^2\text{s}^{-1} \tag{G.1}$$

[30]. The scattering mean free path is related to $\kappa_{||}$ by:

$$\lambda_{\text{mfp}} = 3\kappa_{||}/v \tag{G.2}$$

[46]. The velocity of 100 MeV protons is $v = 1.3 \times 10^{10}$, which translates to a mean free path of

$$\lambda_{\text{mfp}} \approx 10^{18} \text{ cm} = 66,846 \text{ AU}. \tag{G.3}$$

This is the length scale over which particles are made isotropic by scattering off of turbulent fluctuations. For reference, the heliopause is of the order of $\sim$120 AU, and 1 ly = 64, 241 AU.

## G.2 Liouville's Theorem

Liouville's theorem states that the distribution function along a dynamical trajectory remains constant; phase space trajectories are conserved:

$$f(\vec{x}, \vec{v}, t) = f(\vec{x}_i, \vec{v}_i, t_i). \tag{G.4}$$

If the particles are modified by shocks, ($\vec{x}_i$, $\vec{v}_i$) is the phase space coordinate at time $t_i$ before the shock and ($\vec{x}$, $\vec{v}$) are at time $t$ after the encounter with the shock. In terms of energies and pitch angles,

$$f(E, \alpha) = f(E_i, \alpha_i). \tag{G.5}$$

Therefore, knowing the particles' initial distribution function enables calculation of their final distribution function.

Particles reflecting from a shock often gain energy in the process. As their energies increase, their original spectral intensities will be retained, resulting in sudden peaks in the energetic particle intensity distribution known as "shock spikes" (see for example, [57]). Due to the shape of the interstellar spectrum, which has larger intensities at lower energies (recall Chapter 2, Section 2.3), particles with previously low energies contribute to an increased intensity at their new higher energies, leading to enhancements in GCR intensities. The opposite is true when particles lose energy – energy losses translate to a decrease in intensity (a prime example of this is solar modulation in the heliosphere).

# Bibliography


[1] A. C. Cummings, E. C. Stone, B. C. Heikkila, N. Lal, W. R. Webber, G. Jóhannesson, I. V. Moskalenko, E. Orlando, and T. A. Porter, "Galactic Cosmic Rays in the Local Interstellar Medium: Voyager 1 Observations and Model Results," *Astrophysical Journal* **831** (Nov., 2016) 18.

[2] J. D. Sullivan, "Geometrical factor and directional response of single and multi-element particle telescopes," *Nuclear Instruments and Methods* **95** (1971) 5.

[3] J. Kóta and J. R. Jokipii, "Transient Cosmic-ray Events beyond the Heliopause: Interpreting Voyager-1 Observations," *Astrophysical Journal* **839** (Apr., 2017) 126.

[4] D. A. Gurnett, W. S. Kurth, E. C. Stone, A. C. Cummings, S. M. Krimigis, R. B. Decker, N. F. Ness, and L. F. Burlaga, "Precursors To Interstellar Shocks of Solar Origin," *Astrophysical Journal* **809** (Aug., 2015) 121.

[5] E. C. Stone, A. C. Cummings, B. C. Heikkila, N. Lal, and W. R. Webber, "The Anisotropy of Anomalous Cosmic Rays Observed by Voyager 2 in the Heliosheath," *PoS* **ICRC2017** (2018) 057.

[6] E. N. Parker, "Dynamics of the Interplanetary Gas and Magnetic Fields.," *Astrophysical Journal* **128** (Nov., 1958) 664.

[7] E. N. Parker, "A history of early work on the heliospheric magnetic field," *Journal of Geophysical Research* **106** (Aug., 2001) 15797–15802.

[8] K. R. Lang, *The Sun from Space*. 2009.

[9] N. F. Ness and J. M. Wilcox, "Solar Origin of the Interplanetary Magnetic Field," *Physical Review Letters* **13** (Oct., 1964) 461–464.

[10] A. Balogh, L. J. Lanzerotti, and S. T. Suess, *The Heliosphere through the Solar Activity Cycle*. Springer-Praxis Books and Springer Science+Business Media, 2008.

[11] D. H. Hathaway, "The Solar Cycle," *Living Reviews in Solar Physics* **7** (Mar., 2010) 1.

[12] D. V. Reames, "What Are the Sources of Solar Energetic Particles? Element Abundances and Source Plasma Temperatures," *Space Science Reviews* **194** (Nov., 2015) 303–327, arXiv:1510.03449 [astro-ph.SR].

[13] E. C. Stone, A. C. Cummings, F. B. McDonald, B. C. Heikkila, N. Lal, and W. R. Webber, "Voyager 1 Explores the Termination Shock Region and the Heliosheath Beyond," *Science* **309** (Sept., 2005) 2017–2020.

[14] R. B. Decker, S. M. Krimigis, E. C. Roelof, M. E. Hill, T. P. Armstrong, G. Gloeckler, D. C. Hamilton, and L. J. Lanzerotti, "Voyager 1 in the

Foreshock, Termination Shock, and Heliosheath," *Science* **309** (Sept., 2005) 2020–2024.

[15] L. F. Burlaga, N. F. Ness, M. H. Acuña, R. P. Lepping, J. E. P. Connerney, E. C. Stone, and F. B. McDonald, "Crossing the Termination Shock into the Heliosheath: Magnetic Fields," *Science* **309** (Sept., 2005) 2027–2029.

[16] D. A. Gurnett and W. S. Kurth, "Electron Plasma Oscillations Upstream of the Solar Wind Termination Shock," *Science* **309** (Sept., 2005) 2025–2027.

[17] E. C. Stone, A. C. Cummings, F. B. McDonald, B. C. Heikkila, N. Lal, and W. R. Webber, "An asymmetric solar wind termination shock," *Nature* **454** (July, 2008) 71–74.

[18] R. B. Decker, S. M. Krimigis, E. C. Roelof, M. E. Hill, T. P. Armstrong, G. Gloeckler, D. C. Hamilton, and L. J. Lanzerotti, "Mediation of the solar wind termination shock by non-thermal ions," *Nature* **454** (July, 2008) 67–70.

[19] L. F. Burlaga, N. F. Ness, M. H. Acuña, R. P. Lepping, J. E. P. Connerney, and J. D. Richardson, "Magnetic fields at the solar wind termination shock," *Nature* **454** (July, 2008) 75–77.

[20] D. A. Gurnett and W. S. Kurth, "Intense plasma waves at and near the solar wind termination shock," *Nature* **454** (July, 2008) 78–80.

[21] J. D. Richardson, J. C. Kasper, C. Wang, J. W. Belcher, and A. J. Lazarus, "Cool heliosheath plasma and deceleration of the upstream solar wind at the termination shock," *Nature* **454** (July, 2008) 63–66.

[22] J. D. Richardson and R. B. Decker, "Plasma and flows in the heliosheath," *Journal of Physics: Conference Series* **577** no. 1, (2015) 012021.

[23] L. F. Burlaga, N. F. Ness, D. A. Gurnett, and W. S. Kurth, "Evidence for a Shock in Interstellar Plasma: Voyager 1," *Astrophysical Journal Letters* **778** (Nov., 2013) L3.

[24] L. F. Burlaga, N. F. Ness, M. H. Acuña, Y.-M. Wang, and N. R. Sheeley, "Radial and solar cycle variations of the magnetic fields in the heliosheath: Voyager 1 observations from 2005 to 2008," *Journal of Geophysical Research (Space Physics)* **114** (June, 2009) A06106.

[25] L. Davis, "Interplanetary Magnetic Fields and Cosmic Rays," *Physical Review* **100** (Dec., 1955) 1440–1444.

[26] E. N. Parker, *Interplanetary dynamical processes.* 1963.

[27] P. C. Frisch, S. Redfield, and J. D. Slavin, "The Interstellar Medium Surrounding the Sun," *Annual Review of Astronomy and Astrophysics* **49** (Sept., 2011) 237–279.

[28] E. J. Zirnstein, J. Heerikhuisen, H. O. Funsten, G. Livadiotis, D. J. McComas, and N. V. Pogorelov, "Local Interstellar Magnetic Field Determined from the Interstellar Boundary Explorer Ribbon," *Astrophysical Journal Letters* **818** (Feb., 2016) L18.

[29] M. Ackermann, M. Ajello, and A. Allafort et al., "Detection of the

Characteristic Pion-Decay Signature in Supernova Remnants," *Science* **339** (Feb., 2013) 807–811, arXiv:1302.3307 [astro-ph.HE].

[30] V. S. Ptuskin, "Propagation, Confinement Models, and Large-Scale Dynamical Effects of Galactic Cosmic Rays," *Space Science Reviews* **99** (Oct., 2001) 281–293.

[31] L.-L. Zhao, L. Adhikari, G. P. Zank, Q. Hu, and X. S. Feng, "Influence of the Solar Cycle on Turbulence Properties and Cosmic-Ray Diffusion," *Astrophysical Journal* **856** (Apr., 2018) 94.

[32] D. A. Gurnett, W. S. Kurth, L. F. Burlaga, and N. F. Ness, "In situ observations of interstellar plasma with voyager 1," *Science* **341** no. 6153, (2013) 1489–1492.

[33] S. A. Fuselier and I. H. Cairns, "The 2-3 khz Heliospheric Radiation, the IBEX Ribbon, and the Three-dimensional Shape of the Heliopause," *Astrophysical Journal* **771** (July, 2013) 83.

[34] L. F. Burlaga, "Interplanetary magnetohydrodynamics.," *Interplanetary magnetohydrodynamics, by L. F. Burlag. International Series in Astronomy and Astrophysics, Vol. 3, Oxford University Press. 1995. 272 pages; ISBN13: 978-0-19-508472-6* **3** (1995) .

[35] J. D. Richardson, C. Wang, Y. D. Liu, J. Šafránková, Z. Němeček, and W. S. Kurth, "Pressure Pulses at Voyager 2: Drivers of Interstellar Transients?," *Astrophysical Journal* **834** (Jan., 2017) 190.

[36] G. P. Zank and H.-R. Müller, "The dynamical heliosphere," *Journal of Geophysical Research (Space Physics)* **108** (June, 2003) 1240.

[37] H. Washimi, G. P. Zank, Q. Hu, T. Tanaka, K. Munakata, and H. Shinagawa, "Realistic and time-varying outer heliospheric modelling," *Monthly Notices of the Royal Astronomical Society* **416** (Sept., 2011) 1475–1485.

[38] H. Washimi, T. Tanaka, and G. P. Zank, "Time-varying Heliospheric Distance to the Heliopause," *Astrophysical Journal Letters* **846** (Sept., 2017) L9.

[39] Y. D. Liu, J. D. Richardson, C. Wang, and J. G. Luhmann, "Propagation of the 2012 March Coronal Mass Ejections from the Sun to Heliopause," *Astrophysical Journal Letters* **788** (June, 2014) L28, arXiv:1405.6086 [physics.space-ph].

[40] R. L. Fermo, N. V. Pogorelov, and L. F. Burlaga, "Transient shocks beyond the heliopause," *Journal of Physics: Conference Series* **642** no. 1, (2015) 012008.

[41] T. K. Kim, N. V. Pogorelov, and L. F. Burlaga, "Modeling Shocks Detected by Voyager 1 in the Local Interstellar Medium," *Astrophysical Journal Letters* **843** (July, 2017) L32, arXiv:1706.04221 [physics.space-ph].

[42] E. C. Stone, A. C. Cummings, F. B. McDonald, B. C. Heikkila, N. Lal, and W. R. Webber, "Voyager 1 Observes Low-Energy Galactic Cosmic Rays in a Region Depleted of Heliospheric Ions," *Science* **341** (July, 2013) 150–153.

[43] W. R. Webber and F. B. McDonald, "Recent Voyager 1 data indicate that on 25 August 2012 at a distance of 121.7 AU from the Sun, sudden and unprecedented intensity changes were observed in anomalous and galactic cosmic rays," *Geophysical Research Letters* **40** (May, 2013) 1665–1668.

[44] S. M. Krimigis, R. B. Decker, E. C. Roelof, M. E. Hill, T. P. Armstrong, G. Gloeckler, D. C. Hamilton, and L. J. Lanzerotti, "Search for the Exit: Voyager 1 at Heliosphere's Border with the Galaxy," *Science* **341** (July, 2013) 144–147.

[45] L. F. Burlaga and N. F. Ness, "Observations of the Interstellar Magnetic Field in the Outer Heliosheath: Voyager 1," *Astrophysical Journal* **829** (Oct., 2016) 134.

[46] J. R. Jokipii and J. Kóta, "Interpretation of the Disturbance in Galactic Cosmic Rays Observed on Voyager 1 beyond the Heliopause," *Astrophysical Journal Letters* **794** (Oct., 2014) L4.

[47] W. R. Webber and T. L. Villa, "A Comparison of the Galactic Cosmic Ray Electron and Proton Intensities From 1 MeV/nuc to 1 TeV/nuc Using Voyager and Higher Energy Magnetic Spectrometer Measurements Are There Differences in the Source Spectra of These Particles?," *ArXiv e-prints* (June, 2018) , arXiv:1806.02808 [physics.space-ph].

[48] E. C. Stone, R. E. Vogt, F. B. McDonald, B. J. Teegarden, J. H. Trainor, J. R. Jokipii, and W. R. Webber, "Cosmic ray investigation for the Voyager missions: Energetic particle studies in the outer heliosphere - and beyond," *Space Science Reviews* **21** (Dec., 1977) 355–376.

[49] T. T. von Rosenvinge, D. V. Reames, R. Baker, J. Hawk, J. T. Nolan, L. Ryan, S. Shuman, K. A. Wortman, R. A. Mewaldt, A. C. Cummings, W. R. Cook, A. W. Labrador, R. A. Leske, and M. E. Wiedenbeck, "The High Energy Telescope for STEREO," *Space Science Reviews* **136** (Apr., 2008) 391–435.

[50] M. E. Wiedenbeck et al., "Capabilities and Performance of the High-Energy Energetic-Particles Instrument for the Parker Solar Probe Mission," *PoS* **ICRC2017** (2018) 016. %%CITATION = POSCI,ICRC2017,016;%%.

[51] W. R. Cook, III, *Elemental composition of solar energetic particles.* PhD thesis, California Institute of Technology, Pasadena., 1981.

[52] W. R. Cook, E. C. Stone, and R. E. Vogt, "Elemental composition of solar energetic particles," *Astrophysical Journal* **279** (Apr., 1984) 827–838.

[53] D. E. Stilwell, W. D. Davis, R. M. Joyce, F. B. McDonald, J. H. Trainor, W. E. Althouse, A. C. Cummings, T. L. Garrard, E. C. Stone, and R. E. Vogt, "The Voyager Cosmic Ray Experiment," *IEEE Transactions on Nuclear Science* **26** (Feb., 1979) 513–520.

[54] Y. Guo and R. W. Farquhar, "New Horizons Mission Design," *Space Science Review* **140** (Oct., 2008) 49–74.

[55] D. J. McComas, F. Allegrini, P. Bochsler, M. Bzowski, M. Collier, H. Fahr, H. Fichtner, P. Frisch, H. O. Funsten, S. A. Fuselier, G. Gloeckler, M. Gruntman, V. Izmodenov, P. Knappenberger, M. Lee, S. Livi, D. Mitchell, E. Möbius, T. Moore, S. Pope, D. Reisenfeld, E. Roelof, J. Scherrer, N. Schwadron, R. Tyler, M. Wieser, M. Witte, P. Wurz, and G. Zank, "IBEX – Interstellar Boundary Explorer," *Space Science Reviews* **146** (Aug., 2009) 11–33.

[56] R. B. Decker, S. M. Krimigis, E. C. Roelof, and M. E. Hill, "No meridional plasma flow in the heliosheath transition region," *Nature* **489** (Sept., 2012) 124–127.

[57] R. B. Decker, "Formation of shock-spike events at quasi-perpendicular shocks," *Journal of Geophysical Research* **88** (Dec., 1983) 9959–9973.

[58] P. Van Nes, E. C. Roelof, R. Reinhard, T. R. Sanderson, and K.-P. Wenzel, "A major shock-associated energetic storm particle event wherein the shock plays a minor role," *Journal of Geophysical Research* **90** (May, 1985) 3981–3994.

[59] D. Lario, Q. Hu, G. C. Ho, R. B. Decker, E. C. Roelof, and C. W. Smith, "Statistical Properties of Fast Forward Transient Interplanetary Shocks and Associated Energetic Particle Events: ACE Observations," in *Solar Wind 11/SOHO 16, Connecting Sun and Heliosphere*, B. Fleck, T. H. Zurbuchen, and H. Lacoste, eds., vol. 592 of *ESA Special Publication*, p. 81. Sept., 2005.

[60] P. C. Filbert and P. J. Kellogg, "Electrostatic noise at the plasma frequency beyond the earth's bow shock," *Journal of Geophysical Research* **84** (Apr., 1979) 1369–1381.

[61] S. D. Bale, M. J. Reiner, J.-L. Bougeret, M. L. Kaiser, S. Krucker, D. E. Larson, and R. P. Lin, "The source region of an interplanetary type II radio burst," *Geophysical Research Letters* **26** (1999) 1573–1576.

[62] H. V. Cane, "Coronal Mass Ejections and Forbush Decreases," *Space Science Review* **93** (July, 2000) 55–77.

[63] J. A. Lockwood, W. R. Webber, and J. R. Jokipii, "Characteristic recovery times of Forbush-type decreases in the cosmic radiation. I - Observations at earth at different energies," *Journal of Geophysical Research* **91** (Mar., 1986) 2851–2857.

[64] R. E. Gold and D. S. Peacock, "The Forbush Predecrease," *Journal of Geophysical Research* **78** (1973) 577.

[65] M. Papailiou, H. Mavromichalaki, A. Belov, E. Eroshenko, and V. Yanke, "Precursor Effects in Different Cases of Forbush Decreases," *Solar Physics* **276** (Feb., 2012) 337–350.

[66] A. V. Belov, L. I. Dorman, E. A. Eroshenko, N. Iucci, G. Villoresi, and V. G. Yanke, "Search for Predictors of Forbush Decreases," *International Cosmic Ray Conference* **4** (1995) 888.

[67] K. Leerungnavarat, D. Ruffolo, and J. W. Bieber, "Loss Cone Precursors to Forbush Decreases and Advance Warning of Space Weather Effects," *Astrophysical Journal* **593** (Aug., 2003) 587–596.

[68] D. A. Gurnett, W. S. Kurth, S. C. Allendorf, and R. L. Poynter, "Radio Emission from the Heliopause Triggered by an Interplanetary Shock," *Science* **262** (Oct., 1993) 199–203.

[69] L. F. Burlaga, V. Florinski, and N. F. Ness, "In Situ Observations of Magnetic Turbulence in the Local Interstellar Medium," *Astrophysical Journal Letters* **804** (May, 2015) L31.

[70] L. F. Burlaga, V. Florinski, and N. F. Ness, "Turbulence in the Outer Heliosheath," *Astrophysical Journal* **854** (Feb., 2018) 20.

[71] E. C. Roelof, R. B. Decker, M. E. Hill, and S. M. Krimigis, "Galactic Cosmic Ray Pitch-Angle Anisotropies Beyond the Edge of the Hot Heliosheath: Voyager-1 Observations and Interpretations," *AGU Fall Meeting Abstracts* (Dec., 2013) SH11B–1978.